Multimodal Harmonic Generation Imaging of Highly Scattering Biological Tissues

David MacFarquhar, Department of Physics

McGill University, Montreal

August, 2021

A thesis submitted to McGill University in partial fulfillment of the requirements of the degree of

Master of Physics

©David MacFarquhar, 2021

Abstract

The development of harmonic generation microscopy has presented biological scientists with a novel label-free, high-contrast method of imaging based on structural properties of a biological sample. However, imaging unexplored systems without engineered fluorescence as the source of contrast can be unpredictable, making quantitative methods an important part of these investigations. This thesis aims to broaden the current scope of the field by demonstrating nonlinear multimodal microscopy as a viable method of quantitative imaging in two highly scattering biological tissues. Chapter 1 briefly reviews the development of biological microscopy leading up to nonlinear harmonic generation imaging, and introduces the biological context of two distinct tissue structures: the byssal thread of the sea mussel *Mytilus edulis* and the developing brain of the tadpole *Xenopus laevis*. Chapter 2 gives an in-depth explanation of the physics behind multiphoton scanning microscopy, and introduces image correlation spectroscopy (ICS) as an analytical technique. In Chapter 3 the microscopy instrumentation, sample preparation methods, and algorithms employed for data processing are outlined in detail. Chapter 4 contains the results of multimodal imaging, and the results of the analysis of those images, for two main components of the byssal thread and for the myelination process as it occurs during tadpole development. Full discussion of the interpretation of these findings is left to Chapter 5, which concludes the work with directions for how these techniques can be incorporated into future research on their respective systems.

Abrégé

Le développement de la microscopie à génération harmonique a présenté les scientifiques en biologie avec une nouvelle méthode d'imagerie sans étiquette, basé sur les propriétés structurelles d'un système biologique. Cependant, l'imagerie de systèmes inconnues sans fluorescence artificielle comme source de contraste peut être imprévisible, ce qui fait des méthodes quantitatives une partie importante de ces investigations. Cette thèse sert à élargir l'état actuel du domaine en démontrant la microscopie multimodale non linéaire comme une méthode viable d'imagerie quantitative dans deux tissus biologiques hautement diffusants. Le chapitre 1 passe brièvement en revue le développement de la microscopie biologique jusqu'a à l'introduction de la microscopie à génération harmonique non linéaire, et présente le contexte biologique de deux tissus distincts : le fil byssal de la moule de mer *Mytilus edulis* et le cerveau en développement du têtard *Xenopus laevis*. Le chapitre 2 donne une explication approfondie de la physique de la microscopie à balayage non linéaire et présente la spectroscopie de corrélation d'images (ICS) comme une technique analytique. Dans le chapitre 3, l'instrumentation de microscopie, les méthodes de préparation des échantillons et les algorithmes employés pour le traitement des données sont décrits en détail. Le chapitre 4 contient les résultats de l'imagerie multimodale, et les résultats de l'analyse de ces images, pour deux composants principaux du fil byssal et pour le processus de myélinisation tel qu'il se produit au cours du développement du têtard. La discussion complète de l'interprétation de ces résultats est laissée au chapitre 5, qui conclut le travail avec des indications sur la façon dont ces techniques peuvent être incorporées dans les recherches futures sur leurs systèmes respectifs.

Acknowledgements

Many thanks go out to the huge cast of people who have helped throughout this process in so many ways. First to present and recent members of the Wiseman Lab, particularly (in roughly chronological order): Alexei Kazarine for training and entrusting me with the nonlinear dinosaur; Sarah Aufmkolk for invaluable guidance and insight into physics, biology and academia; Ksenia Kolosova for help with technical troubleshooting and many other little bits; Kamila Mustafina for teaching me wetlab things and commiseration during long days at the lab in a pandemic; Thomas Mosher, Sebastian Morales-Velez, Simon Sehayek, and Sneha Paul for fielding constant questions about ICS, Ahmad Mahmood for fielding constant questions about PCA and occasional questions about ICS. And of course Paul W. Wiseman for coordinating my work with the Harrington and Ruthazer labs while steering our lab ship through rough waters. I also owe much to collaborators from other labs: Tobias Priemel for the original mussel tissue samples; Lucia Youssef for the preparation of the crucial sectioned byssal threads, as well as TEM images; Matthew Harrington for direction on the secrets to be unlocked in the byssal threads; Zahraa Chorghay for involving me in her excellent work with myelination in tadpoles and providing all of the samples imaged here; Manon Oliero for discussions about the peculiar nature of biological research and proofreading.

Of course I would not have made it through this without friends in the physics department (you know who you are), friends afar during the online year (and counting), my incredible parents Carole and Ian (who have put up with an awful lot to get me here), and Manon in her other capacity as a wonderful partner (you get mentioned twice).

Table of Contents

List of Figures

List of Tables

List of Abbreviations

1D: one dimensional

1PF: single photon/linear fluorescence

2D: Two dimensional

2PF: two-photon fluorescence

3D: three dimensional

3DiSCO: three dimensonal imaging of solvent cleared organs

3PF: three photon fluorescence

4PF: four photon fluorescence

ACF: autocorrelation function

ASW: artificial seawater

BF: bright field

CANDLE: collaborative approach for enhanced de-noising under low-light excitation

CARS: coherent anti-Stokes Raman spectroscopy

CCF: cross-correlation function

CD: cluster density

CLSM: confocal laser scanning microscopy

CNS: central nervous system

CRS: confocal Raman (micro)spectroscopy

CT-FiRE: curvelet transform fiber extraction

DBE: dibenzyl ether

ECM: extracellular matrix

EM: electromagnetic

FCS: fluorescence correlation spectroscopy

FWHM: full width (at) half maximum

HGM: harmonic generation microscopy

ICCS: image cross-correlation spectroscopy

ICS: image correlation spectroscopy

MBP: myelin basic protein

MPF: multiphoton fluorescence

MPFM: multiphoton fluorescence microscopy

NLSM: nonlinear scanning microscopy

NA: numerical aperture

NIR: near infrared

OPO: optical parametric oscillator

PSF: point spread function

PC: principal component

PCA: principal component analysis

PMT: photomultiplier tube

PsR: picrosirius red (stain)

ROI: region of interest

SHG: second harmonic generation

SCoRe: spectral confocal reflectance

SNR: signal-to-noise ratio

SRS: stimulated Raman spectroscopy

THG: third harmonic generation

VST: variance-stabilized transform

Chapter 1

Introduction

1.1 The biological microscopist's toolbox

Since the invention of the light microscope nearly 400 years ago, it has been an integral part of research in the biological sciences. Far from its humble beginnings, modern microscopy uses photons from deep infrared [1] through to x-ray wavelengths [2,3], atomic forces [4], electrons [5], and even acoustic waves [6] to illuminate contrast in samples and produce images. These have been supported by advances in stable laser light sources [7,8] and the ability of computers to both control hardware and handle vast amounts of digital data [9]. Breaking the limits of conventional optical physics, both live and fixed samples are imaged with a resolution on the scale of tens of nanometers [7,10,11]. Theoretical models can now be verified experimentally and questions unimaginable one hundred years ago can be answered with quantifiable evidence.

Often research begins with a hypothesis regarding mechanisms that control a biological system. Subsequently, there is consideration which experimental method of data collection best suits the hypothesis. Different techniques have drawbacks and advantages: speed, resolution, flexibility, and costs vary widely between a simple benchtop polarized light microscope (<$1000, 10 µm resolution) and a cryogenic electron microscopy system ($7M + operating costs, 0.2 nm resolution [12]). Many of the most widely used methods in

biology and biophysics are classified under the scope of light microscopy, where photons with wavelengths in or near the visible spectrum are focused through a system of lenses onto a sample and the emitted signal is analyzed for changes in phase, frequency, or intensity. In the simplest form, the entire field of view is illuminated with white light and the transmitted light is observed directly. Bright field (BF) microscopy remains widely used for clinical histology and low-resolution research applications [13]. Using special dyes with affinity for certain tissues, features of interest can be made to stand out against a larger sample [14,15]. Optical filters and polarizers can also be used to provide additional contrast [16] by separating photons based on wavelength and polarization. BF microscopy is ultimately limited by low/imperfect contrast, since unstained features are still visible, and loosely focused light interacts with sample planes both above and below the focal point, blurring the image. Estimating the contributions of the out-of-focus planes requires additional processing [17,18] and is not straightforward.

Fluorescence microscopy provides a great improvement in contrast over white light by illuminating samples with narrow-band wavelengths; molecules with the right electronic properties absorb the photons to enter an excited state, disperse some of the energy thermally within picoseconds [19], then emit the remaining energy as a photon in an effectively random, isotropic direction [20]. The likelihood of absorption varies between fluorophores and is known as the cross section. The fluorescence lifetime, which describes the duration of the excited state before photon emission, is generally on the nanosecond timescale, and can be a source of information itself [21–24].

Fluorescence microscopy was first developed on longer-lived (phosphorescent) transitions observed in endogenous molecules [25]. It has since been improved by the incorporation of immunohistochemistry [15,26] and genetic fluorescent labelling, pioneered with green fluorescent protein [27], where exogenous fluorophores (as molecules that display fluorescent behaviour are known) are introduced artificially to label non-fluorescent features in a sample. Systems employing laser wavelengths from the near-infrared (NIR) through the visible spectrum to the near-ultraviolet, and corresponding fluorophores, give

researchers many options to tailor their approach to each application. Even complicating factors have been put to productive use. Fluorophores can become trapped temporarily in an excited state where they do not decay (i.e. a dark non-emissive state); this on/off blinking is the foundation of certain cutting edge super-resolution techniques [28, 29]). They will also eventually cease to fluoresce altogether due to oxidation in a process known as photobleaching, which can be used to measure diffusion in cells and artificial lipid bilayers [30].

These imaging techniques have been further developed to make it possible to image single µm-thick planes, and to construct three dimensional images of intact samples. There are three distinct ways that this has been accomplished. Total internal reflection microscopes take wide field images by exploiting the physics of total internal reflection to generate a boundary evanescent field, exciting fluorophores only within the first hundred nanometres of the surface [30]. The trade-off for excellent axial resolution is the limitation of imaging to only surface features. If 3D reconstruction is required, either plane- or point-focused scanning microscopy is required. Planar approaches like light sheet microscopy and selective plane illumination microscopy employ carefully designed lens systems to produce a two-dimensional sheet of excitation light. This excites a 1-2 µm plane in the sample that can be scanned in the third dimension, with the detection path located along this axis [31]. This allows fast 3D imaging but is very technically demanding and systems often have limited flexibility [32]. Confocal laser scanning microscopy (CLSM) on the other hand uses one or more lenses to focus light as tightly as possible to a single point on or within a sample with up to $\sim$300 nm resolution [33]. The fluorescence is then focused (either by the objective lens or one located immediately opposite it) through a pinhole the size of the focal point and onto a detector or eyepiece; photons originating above or below the beam focus are focused on a spot away from the pinhole and the vast majority do not reach the detector [34]. The simple design is most significantly limited by the fact that out-of-focus planes are still subject to photobleaching, and mitigation requires careful manipulation of the local oxidation/reduction pathways [35, 36]. Visible

wavelengths are also prone to scattering and absorption in biological samples [37, 38] which restricts the ability to image at high resolution beyond a depth of a few hundred microns. Optical clearing methods can extend this depth if chosen correctly, at the risk of causing unintended changes in sample structure [39].

1.2 Nonlinear methods in microscopy

An alternative to CLSM exists in nonlinear scanning microscopy (NLSM), beginning with multiphoton fluorescence microscopy (MPF/MPFM) [40]. It is possible for a fluorophore to absorb two or more photons before emitting one single photon of fluorescence, although the cross section is much smaller. At low powers the rate of multiphoton fluorescence is extremely low; the photon flux is only dense enough for a significant rate of MPF in the area immediately around the focal point of a pulsed laser with high peak power. As absorption is limited to this small focal volume, optically sectioned imaging and 3D reconstruction of the imaged slices is possible without the pinhole of CLSM. Only a fraction of the incident photons are converted via MPF, but this is compensated for by the fact that there is no out-of-focus fluorescence and all emitted photons can be collected. Detection can then be done at any angle, making 3D live sample imaging feasible [41]. If using readily available fluorophores and detectors designed for the visible spectrum, MPF requires excitation wavelengths are in the NIR, which scatter less than visible light within tissue. This further reduces photobleaching and photodamage outside of the focal volume and increases the depth to which imaging can be performed in thick samples, cementing MPFM as an improvement on CLSM for the imaging of biological tissues.

Two-photon fluorescence (2PF) has been used with existing dyes for calcium ions [42–44], DNA [44, 45], and generally with immunohistochemical stains, as well as with autofluorescent endogenous molecules [23, 46]. Three-photon fluorescence (3PF) increases the penetration depth even further and improves resolution slightly over 2PF [47]. Endogenous tryptophan and seratonin have large autofluorescent 3PF cross sections [48], and

conventional fluorescent stains were recently used with 3PF to image mouse brain structure through intact bone [49]. New labels have been developed for 2PF and 3PF ranging from modified existing fluorophores [50], to entirely new ones [51–53], to nanoparticles for cancer screening [54]. MPF can also be used in other nontraditional ways, such as in pH sensing [55] and measuring fluorescence anisotropy [56]. The inverse relationship between wavelength and spatial resolution and the high energies necessary to drive four-plus photon absorption pose challenges, but four-photon fluorescence (4PF) has been achieved both with genetically expressed fluorescence [57] and exogenous staining [58]. Challenges invite further innovations: visible-to-visible 4PF [59], two-step four photon absorption [60], and five photon absorption [61]) have all been demonstrated. These have limited applications so far in biology because of their esoteric nature and the risks of damage to specimens at such high laser powers.

One key innovation was the importation of optical harmonic generation microscopy (HGM) from materials science, originally to investigate the polar nature of collagen in rat tail tendons [62]. Unlike fluorescence, harmonic generation is a non-absorptive scattering effect where the dielectric polarization of molecules caused by a passing electromagnetic (EM) wave drives the lossless up-conversion of multiple low energy photons into a single high energy one. This process is largely independent of the frequency of the EM wave as long as it is reasonably far from the atomic resonance of the material [63]. The rate of conversion depends on the structure and molecular properties of the medium. Second harmonic generation (SHG), where two incident photons produce one scattered photon, occurs in bulk crystals or structures displaying non-centrosymmetric asymmetry. THG occurs in all bulk media, regardless of symmetry, although the conversion efficiency spans a range of 15 orders of magnitude between different materials. It also originates at boundaries where there are large step changes in the nonlinear refractive index [64]. Both processes generally have high conversion rates in birefringent materials, and can be used to extract information about chirality that is unobtainable with linear optical methods [65]. Some dyes and nanoparticles also show the electronic characteristics necessary for

efficient harmonic generation [16,66–68]; analogously to fluorophores, these are known as harmonophores.

The birefringent biomaterial most commonly investigated with HGM is collagen, which produces both SHG and THG [69]. SHG can be used to differentiate the various types of collagen structures that occur naturally in the extracellular matrix (ECM) [70] and to assess structural changes resulting from disease [71,72] and wound healing [73,74]. It can also probe the size of individual collagen fibers [75] and the organization of the amino acids in collagen itself [76]. THG has been applied to imaging lipid bodies [77–79] and hemoglobin cells [80], as well as detecting malaria [81,82] and the perimeters of brain tumors [83]. Unlike fluorescence, harmonic generation is not inherently isotropic [67,84], which makes it sensitive to the orientation of the harmonophores [85]. This allows for information on lipid membrane dynamics to be extracted [86] but has also been used to map muscular tissue [87], the polarity of brain microtubules [88], and the organization of collagen in rat tails as mentioned previously [89]. A major advantage of these techniques is that they often do not require any exogenous stain. However, the use of stains can improve contrast and signal-to-noise ratio (SNR), and labelling dyes can be used for specific detection of structures.

Nonlinear techniques can also be easily demultiplexed with the wide spectral gaps between the frequencies involved. SHG from collagen and endogenous autofluorescence from elastin, another ECM protein, have been used to image a variety of connective tissues [73, 90]. SHG and THG have been employed simultaneously in imaging the structure of the eye [66], blood vessels [91], and viral particles [92,93]. 2PF and THG have been used effectively to image the nervous system [94], combining tagged fluorescence with the natural refractive index change of myelin sheaths. The multimodal approach can be used to distinguish competing features of interest, as with elastin and collagen, or simply to collect data on multiple aspects of a sample simultaneously. It can also easily cross-validate the results of imaging systems with novel modalities. Since biological systems are

often complex, heterogeneous and highly scattering, harmonic and multiphoton imaging approaches are ideal for studying their structural and molecular makeup.

1.3 Imaging byssal threads in sea mussel *Mytulis Edulis*

Among biological systems, the field of bio-inspired materials is replete with novel organisms and open questions. Materials scientists are very interested in natural materials that have been shaped by evolution to display remarkable properties [95]. Organisms have both diversified and converged towards a variety of molecular and structural motifs, but their subtleties make them difficult to replicate on useful scales [96]. Simple localization via fluorescent tagging or proteome characterization explains little about how a natural system mechanically outperforms synthetic equivalents [97]. Comprehensive genetic and cellular knowledge about the organisms that create these biomaterials is sparse compared to human physiology, and hierarchies of less-to-more-complex animal models are nonexistent. These new areas of biomaterials research can benefit greatly from the ultrastructural contrast of HGM and the complimentary nature of multimodal imaging.

One such organism of interest is the aquatic mussel *Mytilus edulis* (Figure 1.1a). It is a typical representative of the multitude of species of bivalves across more than 20 genera that attach to marine surfaces using filaments known as byssal threads, or simply byssi (singular: byssus). These threads withstand remarkable stresses, up to 100 MPa under successive tests while stretching up to twice their length [98], making them a target of bio-inspired materials research [99]. These threads have three components: a core made up of long chains of collagen-like proteins (preCols), a protective cuticle of coagulated, spherical, proteinaceous granules, and a foamy bioadhesive plaque at the distal end that can adhere to nearly any surface (Figure 1.1b). Each byssus is anchored to a common structure (the stem) near the anterior opening, at the base of which is an organ known as the foot. Proteins are stored in vesicles in three distinct glands centred around a groove on the upper surface (Figure 1.1c).

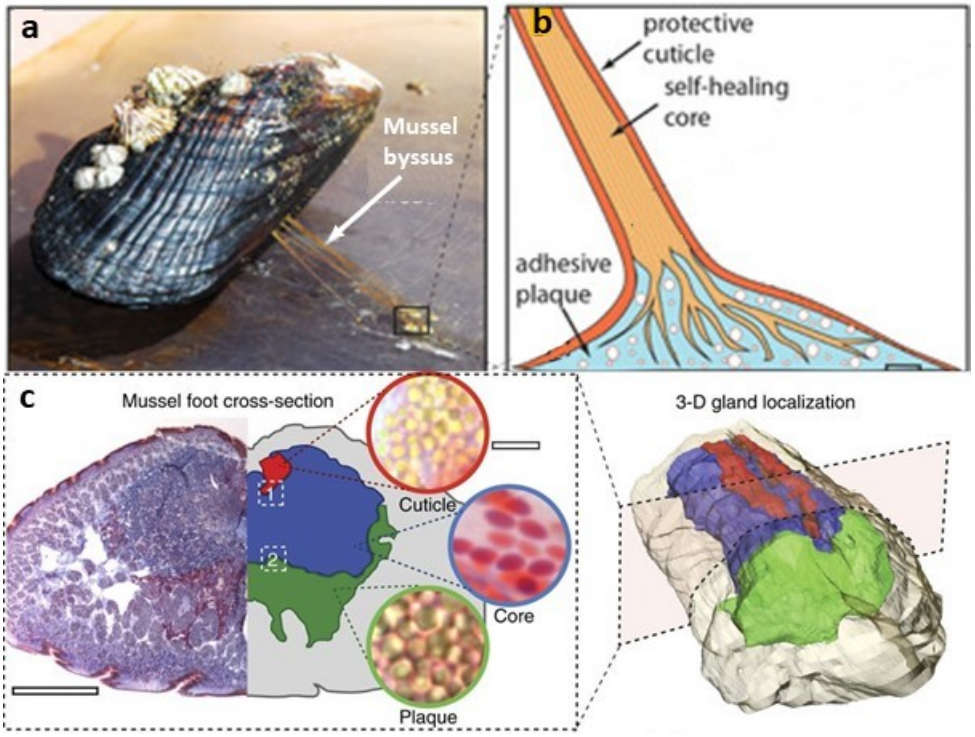

Figure 1.1: Physiology of mussel byssal thread system. a) *Mytilus edulis* adhered to a surface by byssal threads. b) Cross-sectional diagram of the distal end of a thread thread showing the cuticle, collagen core, and adhesive plaque. c) Mussel foot with gland regions colored to indicate the origin of each thread component. Adapted from [100] (a, b, with permission from Wiley) and [101] (c, licensed under Creative Commons).

A new thread is formed by secreting the vesicles, which spontaneously assemble in the salt water environment to form the tripartite structure. Simple inspection with a wide-field microscope shows clearly that the threads are not uniform, having a rippled/wrinkled appearance at the proximal end that transitions to a straighter, narrower distal region comprising roughly 2/3 of the total length. These regions differ both in terms of their their relative amounts of the two main preCol protein variants [102] and mechanical behaviour [98], with the proximal region being much less stiff and having a lower tensile failure point [103]. This composite design allows energy to be dissipated more effectively under the high cyclical loads experienced in marine conditions [104]. At rest, the proximal region is generally protected in the shell while the distal region is exposed; the area at the shell margin where they meet is known as the transition region [103].

The overall properties of the thread are largely due to the structure and organization of the preCol molecules, shown in Figure 1.2. They consist of long helical collagen domains with glycine-rich flanking domains at each end, which differ slightly between the two variants and stretch during extension [105]. These domains contain metal complexes that are likely incorporated from the seawater [106] and form sacrificial, reversible cross-links between the threads [107], previously identified by confocal Raman microspectroscopy (CRS) [101]. The bonds break during extension, then reform during recovery; the degree of cross-linking is one possible way of controlling stiffness between the macroscopic regions [97]. Some form of autonomous regulation of protein distribution, metal incorporation and cross-linking occurs such that the mechanical properties of a thread are compromised if it is formed by chemically triggering the release of the proteins [101]. However, this is poorly understood at the level of the structure of the collagen matrix. The behaviour of the heterogeneous transition zone in particular is a critical piece of this puzzle, since interfaces are common points of failure in mechanical systems. A quantitative mesoscale understanding of the structure would be helpful in bridging the gap between the molecular picture described by CRS and the macroscopic mechanical behaviour determined empirically.

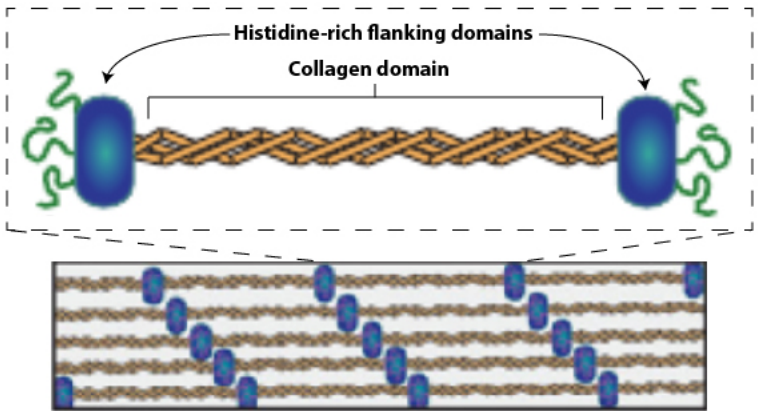

Figure 1.2: Precol molecule showing collagenous central region and flanking crosslinking domains in larger matrix of collagens. Adapted from [100] (with permission from Wiley).

The cuticle appears to serve primarily to protect the thread from abrasion, but also retains water [108] and exhibits hardness and stiffness up to a magnitude greater than that of the core [109]. The main protein component, unique to the cuticle, is present in a gradient along the length of the thread, but is also concentrated in scattered dense, highly cross-linked granules that may serve to make the cuticle behave like a particle-reinforced composite [100,110]. This step-change in density suggests that their size and distribution may be mapped in intact threads using THG, which should have some correlation with the bulk mechanical properties of the different thread regions [111]. Changes in the distribution from the distal to proximal ends may reveal more information about the roles of their respective interior structures.

HGM has been previously applied to numerous biomaterials based on collagen and/or highly similar proteins [112–114]. The natural birefringence of these materials it possible to map their orientation [115,116] and assess variations across a single sample [117] using linear methods, although it has been conclusively demonstrated that this is limited to samples/regions with a common orientation [16]. Collagen-like proteins are also generally able to bind to the collagen-specific stain picrosirius red (PsR) with high affinity. PsR is a birefringent histological dye that has been additionally demonstrated to be a strong harmonophore [93].

Although mussel preCols are not identical to collagen, their molecular structure suggests that they may be imaged using the same approaches [118]. Both SHG from birefringence and THG from PsR staining should identify collagen fibers along the entire length of the thread, and SHG may give further information about the microstructure in the different regions through its dependence on ordered orientation. SHG images have previously been correlated with the mechanical properties of collagen, suggesting that this approach may be applicable to the collagen-like structure of the byssal threads [119,120]. It should be possible to image the core through both modalities simultaneously and in whole threads, which has been a limitation of spectroscopic methods [101]. HGM also avoids the dominant signal of C-H bonds present in Raman spectroscopy that obscures fine detail

when investigating crosslinking [1]. Further, if the density of the granules is achieved through ordered cross-linking, they should be birefringent, which could be imaged with both SHG and THG. With 3D multimodal imaging this information can be gathered in parallel with structural information about the core.

If the qualitative differences in the structure at the proximal and distal ends can be established, and further distinguished quantitatively, it should be possible to determine whether the transition between the two occurs gradually or sharply, which would aid in understanding the physiochemical regulation of thread formation. Quantitative methods applicable to micron-scale images could also be applied to images of byssal threads acquired using different modalities, for comparison and validation. Possible candidates include high-resolution electron microscopy images and Raman spectroscopy [121,122].

1.4 Observing myelination in the central nervous system

The parallel acquisition of information applies equally well when seeking straightforward answers to clearly defined questions where fluorescence alone fails. HGM neatly fills an experimental gap in observing the state of development of an organism's central nervous system (CNS). The ability to observe myelination in the CNS in many ways is an important step towards a mechanistic understanding of the nervous system [123].

The ability of the nervous system to control and regulate an organism's activities depends on the transmission of electrical impulses between neurons via their axons, narrow (sometimes branching) protrusions that connect at their extremities to other neurons or muscle cells. The impulse signals are known as action potentials and entail ion channels in the cell membrane being triggered to open by a local threshold voltage. This voltage propagates as a rapid wave down the axon as adjacent channels are subsequently triggered. To speed up transmission, axons are often wrapped in a fatty insulating layer provided by other cells. Insulating the axon allows the signal to travel faster because only channels in periodic short exposed sections need to open to propagate the signal. In the CNS of nearly

all vertebrates (and some invertebrates), insulation is accomplished via oligodendrocytes [124]. These cells populate the ECM around neurons and extend protrusions that are rich in specialized proteins, such as various forms of myelin basic protein (MBP) [124]. The protrusions wrap around axons tightly many times, pressing out the cytosol and leaving on a lipid bilayer sheath. Figure 1.3 shows a diagram depicting this arrangement.

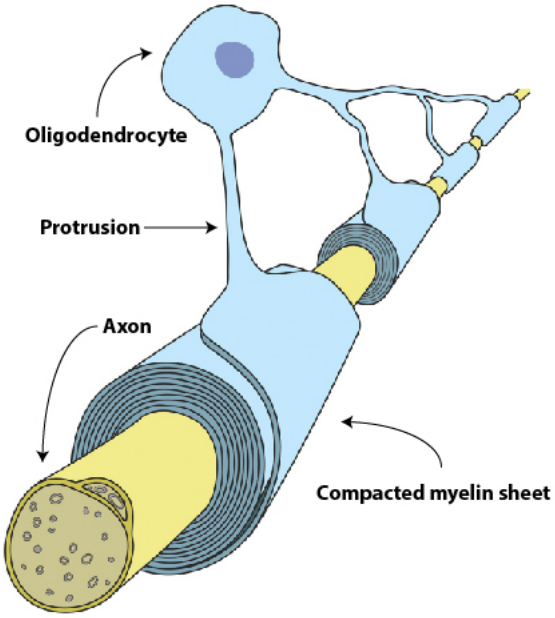

Figure 1.3: Myelination of an axon by protrusions from a nearby oligodendrocyte. Adapted from [123] (with permission from Elsevier)

.

Myelination is uniform neither across all axons nor along the length of individual axons [125]. The thickness and total coverage of the sheath determines the speed at which signals are conducted [126]; improper myelination is a feature of many pathologies affecting the central nervous system, such as multiple sclerosis [127]. Wrapping is triggered by chemical signals released by the neuron, after which MBP binds the lipid bilayers together [128]. This forces out the cytoplasm, creating a continuous volume of phosphonolipids and proteins between 500 nm and 2.5 um thick in human nervous systems [129]. Oligodendrocytes migrate and sequentially wrap axons during the development of the nervous system and throughout its life. There is strong evidence that the fine timing of the circuitry is

accomplished using feedback from the activity of the nervous system, both during its formation and at maturity [130], to direct compaction of already-present myelin. In model systems it should be possible to trace myelination to certain environmental catalysts by imaging its progression [131, 132].

There are many options available for fluorescent imaging of myelin both with exogenous probes and autofluorescence [53, 128, 133]. However, these fail to differentiate between myelin that is simply present around the axon, and myelin that has been compacted. This has instead been accomplished with coherent anti-Stokes Raman spectroscopy (CARS) [134] and stimulated Raman spectroscopy (SRS) [135], which rely on CH_2 bonds in the lipid bilayer for contrast, as well as recently developed spectral confocal reflectance (SCoRe) microscopy [136]. The gold standard for myelination detection (and best spatial resolution) is the use of transmission electron microscopy (TEM) [135]. However, TEM suffers from a limited field of view for imaging and harsh sample preparation that limits it to nonliving fixed samples, and Raman techniques and SCoRe both rely on complex multi-laser instrumentation. The single-laser setup offers a simpler alternative to CARS, SRS and SCoRe [135].

One feature of note is that the compacted myelin sheath in the human nervous system is thick enough to produce a THG signal at the interfaces with the cell membrane and the ECM, while the membrane of a bare axon alone is insufficient. CNS axons produce a THG signal as shown by Farrar et al. [94], and with the same approach as Lim et al. [137] myelination in the visual cortex can be correlated with exposure to stimuli during development. Other aspects of the tissue can add unwanted features to these images: microtubules display a similar birefringence to myelinated neurons [138], potentially visible as both SHG and THG; cell nuclei may be visible due to THG reactivity of chromatin structures [139]; endogenous neurotransmitters tryptophan and seratonin are sources of 3PF [140], which could be generated both in intact synapses and potentially dispersed around damaged ones. Imaging can be facilitated through selection of transparent models,

such as *Xenopus laevis*, an amphibian with sufficiently thick myelin sheaths [141] commonly used to study biological processes due to its simplicity [142].

Explicit links between exposure to stimuli, neuronal activity, and myelination have not been conclusively demonstrated because of the difficulty in determining precise cause and effect [143]. It is significant in itself to be able to track in a quantifiable manner the emergence of a THG signal from compacted myelin at different developmental stages, controlled by exposure of the organism to certain stimuli, regardless of the mediating mechanism between the two. This makes the *Xenopus laevis* particularly appealing. The potential to extend it to live imaging with intermediate time points makes this an especially potent technique.

1.5 Thesis summary

This thesis contains two studies employing multimodal nonlinear microscopy. The first investigation applies the principles of second and third harmonic generation to the sea mussel *Mytulis edulis* with the aim to improve the understanding of the mechanical properties of the byssal threads explored previously by Harrington et al. [100]. The structure of their collagen-like cores is examined by correlating statistical analysis with feature detection algorithms developed by Bredfeldt et al. [72]. The potential for mapping the dense reinforcing granules on the cuticle is also established. The second study uses multimodal THG/2PF imaging similar to Farrar et al. [94] to map the development of axons during brain development in *Xenopus laevis*. The THG and 2PF signals are also examined with correlative and algorithmic methods to attempt to quantify the change in the degree of compact myelination across the time points.

The biological contexts of these two systems have been outlined above in sections 1.3 and 1.4, giving the overall motivation behind the questions at hand as well as explaining the role that harmonic generation can play in answering them. In Chapter 2, Section 2.1 explains the background theory behind florescence and multiphoton fluorescence, with

subsection 2.1.1 expanding the physics that give rise to nonlinear harmonic generation. Section 2.2 contains a brief overview of the techniques used for quantitative image analysis, and how they are applied to the two studies presented in Chapter 4.

Chapter 3 contains detailed descriptions of the experimental methods used in the investigations of these two systems: the custom nonlinear microscope system used to acquire data in 3.1; the sample preparation protocols for mussels and tadpoles in Sections 3.2 and 3.3 respectively; and the packages and pipelines used for data analysis in 3.4. Chapter 4 covers the analysis of the data gathered showing the application of quantitative techniques to multimodal images of both systems. Section 5 discusses the significance of these results with respect to the broader projects of which they are part, summarizing the conclusions that can be drawn from this work and what future studies can be done to make use of them.

Chapter 2

Theory

2.1 Principles of nonlinear scanning microscopy

The energetic processes that give rise to single-photon excited fluorescence (1PF), described in Section 1.1, as well as the nonlinear effects described in Section 1.2 are shown graphically using a Jablonski energy level diagram (Figure 2.1).

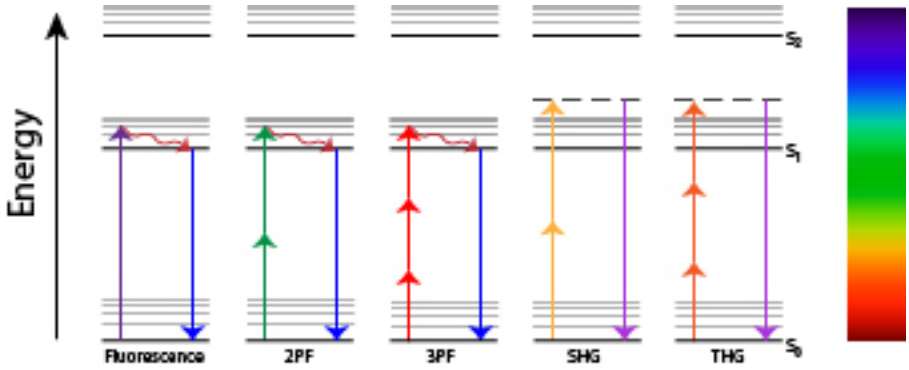

Figure 2.1: Jablonski diagram showing energy transitions involved in single-photon fluorescence, 2PF, 3PF, SHG and THG. Solid black lines indicate excited molecular states of the fluorophore. Grey lines indicate the manifold of molecular vibrational levels. Dashed black lines represent virtual energy states involved in harmonic generation. Straight arrows represent photons; wavy arrows represent internal and vibrational relaxation through phonons. Arrows are color-coded for the relative energies involved.

Straight arrows indicate photons being absorbed, emitted, or scattered. Black lines represent the molecular electronic excitation states starting with the ground state S_0, with grey lines indicating the manifold of molecular vibrational levels that exist immediately above each electronic state. Molecules excited to these energy levels drop to the pure electronic excitation state via internal conversion and vibrational relaxation on a picosecond timescale, much faster than the nanosecond scale of fluorescence, so that the fluorescence photon has a longer wavelength. This energy loss is called the fluorescent Stokes shift. The excitation wavelength in fluorescence microscopy is chosen to target the vibrational excited states so that fluorescent signal can be easily separated from the excitation light. The dashed lines indicate that the states implicated in HG are virtual, rather than real molecular states. There is no Stokes shift involved and the scattered photons have exactly one half or one third the wavelength of the incident photons. The physics of HG are important for understanding its research applications, and are discussed in more detail starting in Section 2.1.1.

The absorption cross sections of MPF (and scattering cross sections of HG) are many magnitudes smaller than those of linear processes. Scanning microscopy with 1PF is often conducted at powers below 1 mW [35,144], with artificial fluorophores designed to have high quantum yield at readily available wavelengths [144–146], or with endogenous molecules that are well-researched due their accessibility [23,128,147,148]. In contrast, even media with high nonlinear susceptibilities/large multiphoton cross sections produce relatively low quantum yields [48,149]. However, the involvement of multiple photons means that the rate of conversion scales with a power dependence equal to the number of incident photons involved [150], and at high intensities the rate of nonlinear conversion grows rapidly compared to the linear increase of single-photon absorption. NLSM is performed using femtosecond-pulsed lasers with average powers on the scale of 100 mW, meaning that the peak power experienced at the focal point is on the scale of kW but total pulse energy remains on the nJ scale.

Raster scanning this point across a 2D plane in a sample produces a 1D sequence of signal-integrated pixel values that are reconstructed into a 2D image. Rastering is accomplished by placing scanning mirrors or optical modulators in the path of the unfocused laser; these control the angle at which the beam is passed through a telecentric scanning lens into a tube lens, before being focused by a high numerical aperture (NA) objective lens. The sample is placed in the focal plane of this lens and scanned by making tiny adjustments to the mirrors. Harmonic generation and/or nonlinear fluorescence occurs in molecules experiencing the concentrated photon flux at focal point, and scattered/emitted light is collected with another objective lens and sequentially binned into pixels.

The size of each pixel (or voxel, when scanning in three dimensions) can be as small as the scanning hardware allows, but the effective spatial resolution is set by the minimum size of the focal volume. This results from the diffraction of the laser by the objective lens. It is specifically known as the point spread function (PSF) of an imaging system and defines a minimum distance between point sources of light below which they will appear as one continuous object in the reconstructed image. Equation 2.1 gives one way of defining the PSF in the X-Y plane for two-photon effects driven by a coherent light source, taken from Latychevskaia [151], with λ representing the wavelength of the laser. MPF has an inherently lower lateral resolution than 1PF of the same emission wavelength because of the longer excitation wavelengths involved. However, since both the excitation and emission profiles can be approximated as Gaussian, and emission intensity has a nonlinear dependence on excitation power, MPF resolution increases with the degree of nonlinearity. A PSF measurement based on the full width at half maximum (FWHM) value of the Gaussian profile for 2PF microscopy, taken from Cox & Sheppard [152], is given in Equation 2.2.

$$R_{xy}^{1PF} = \frac{0.82\lambda}{\mathrm{NA}} \tag{2.1}$$

$$R_{xy}^{2PF} = \frac{0.5\lambda}{2^{1/2} * \mathrm{NA}} \tag{2.2}$$

For 3PF, the optical calculations become quite complex, but work out to an improvement of roughly 20% over the resolution of 2PF when using the same excitation wavelength [153]. Since coherent nonlinear scattering is a fundamentally different process, determining the diffraction limit when imaging with these techniques is slightly more complicated, but has been determined by Zhilie et al. to be slightly smaller [154]. The effective PSF in harmonic generation can also be affected by the orientation of the features relative to the laser beam axis and polarization [155] so the diffraction-limited resolution in HGM can vary slightly between samples.

Moving the sample relative to the objective lens along the axis of propagation of the laser between scans allows for z-sectioning. In this case there is also a different limit in the axial direction based on the z-profile of a focused light source that is slightly larger and is provided in Equation 2.3, taken from Latychevskaia [151]. Since the mathematical origin of this criterion is a sinc rather than a Gaussian function, multiphoton microscopy has no advantage in this dimension.

$$R_z = \frac{\lambda}{\mathrm{NA}^2} \tag{2.3}$$

These limits for the objective lens and excitation wavelength of the microscope system used in this work (NA 1.05 and 1140 nm) are shown in Table 2.1. Since NLSM constructs an image by collecting all fluorescence produced at each scan step, if the any dimension of the voxel is set smaller than the diffraction limit along that axis, photons will be assigned to that voxel that were generated in the voxels immediately adjacent. The image will therefore be a blurred convolution of the sample and the diffraction-limited cross-section of the excitation beam itself. In practice the PSF of a particular microscope setup is slightly larger due to aberrations present in the optical path, and can be measured by imaging fluorescent beads with a sub-diffraction limit diameter (see Section 2.3.1).

Modality (1140 nm excitation)	Lateral resolution (nm)	Axial resolution (µm)
1PF	890	2.07
2PF	384	2.07
3PF	303	2.07
SHG	270	1.3
THG	200	0.5

Table 2.1: Theoretical lateral and axial resolution for 1- ,2- & 3-photon fluorescence and HG microscopy at 1140 nm excitation, using the Rayleigh limit and the limits as calculated by G. Cox and C. J. R. Sheppard [152], Latychevskaia [151], and Tang [154] respectively.

2.1.1 Harmonic susceptibility of materials

The physical origin of nonlinear scattering lies in the fact that when the oscillating electric field of an EM wave passes through a medium, charged components in the medium are pushed in opposite directions. This causes them to experience a time-dependent dielectric polarization $P(t)$. Equation 2.4 describes this below, using the usual complex notation to express an EM wave of amplitude E propagating in time t and assuming a monochromatic driving frequency ω (which is the case in this work). The χ_m terms are properties of the molecules/medium that represent the degree to which they are polarized relative to the amplitude of the wave, given in terms of the vacuum permittivity ε_0. Higher-order terms indicate the response to polarization by multiple photons simultaneously. The ellipsis indicates that terms beyond the third order exist but are negligibly small at the laser powers used in this work.

$$P(t) = \varepsilon_0 \chi_1 E e^{i\omega t} + \varepsilon_0 \chi_2 (E e^{i\omega t})^2 + \varepsilon_0 \chi_3 (E e^{i\omega t})^3 + c.c.... \tag{2.4}$$

More precisely, χ_m are tensors which describe the strength of the coupling between E-field components in each dimension, and between dimensions. The length of the tensor in each dimension reflects the number of physical dimensions (in general, 3) while the rank is determined by the number of photons involved. For example, χ_2 is therefore a

third rank tensor, used in SHG to determine the likelihood of conversion of two incident photons to a single scattered photon.

This oscillating polarization $P(t)$ then becomes an additional source of EM radiation. Expanded fully, $P(t)$ has components at the fundamental frequency, as well as at each integer multiple $n\omega$. Expanding the right hand side of Equation 2.4 shows that the contribution of $P(t)$ can be expressed as a sum of terms at specific frequencies. The following equations show the components of $P(t)$ arising from two- and three-photon coherent scattering (P_2 and P_3, respectively).

$$P_2(t) = P(0) + P(2\omega) \tag{2.5}$$

$$P_3(t) = \frac{3}{4}P(\omega) + \frac{1}{4}P(3\omega) \tag{2.6}$$

If the driving frequency is far from the resonant frequencies of the material, and the medium is therefore lossless (usually valid for optical microscopy of biological specimens [156]), these tensors can be reduced drastically from the six 3x3 matrices of generalized $\chi_2(\omega_1 + \omega_2, \omega_1, \omega_2)$ to one 2D matrix that is sufficient to describe the SHG response of an ordered material. This rigorous approach proves a general principle, that SHG only occurs in non-centrosymmetric materials and χ_2 is otherwise zero [63]. This result can also be found intuitively by inverting the sign of E in Equation 2.4. Assuming inversion symmetry, the sign of $P(t)$ must also change, giving:

$$-P_2(t) = \chi_2 E^2 = P_2(t) \tag{2.7}$$

Which can only be true if χ_2 is zero. However, this is not the case for χ_3 effects due to the odd exponent on E. χ_3 is nonzero for all materials (spanning a range of 15 orders of magnitude), but a full understanding of the conditions under which HG occurs requires consideration of the fact that in both processes the driving EM wave is propagating not only

in time, but also in space. This necessitates the inclusion of phase matching (subsection 2.1.2) and polarization dependence (subsection 2.1.3).

2.1.2 Phase matching considerations

A complete description of a travelling EM wave includes both its temporal and spatial component. Considering only second order effects for simplicity, this changes Equation 2.4 by replacing the constant amplitude E with A_n. This is modulated by an exponential term containing z representing the spatial position in the direction of propagation of the wave, k_n being the spatial frequency or wave vector:

$$P(z,t) = \varepsilon_0 \chi_2 (A_1 e^{-ik_1 z} e^{i\omega_1 t}))(A_2 e^{-ik_2 z} e^{i\omega_2 t}) \tag{2.8}$$

If both waves are coming from the same monochromatic source the subscripts can again be dropped from A and ω. The wave vector k_n is roughly proportional to the frequency of the wave, but also depends on the refractive index of the medium, so photons traveling in a three dimensional non-isotropic medium are distributed across a variety of wave vectors and the subscript is necessary. Momentum is conserved in nonlinear scattering processes via this quantity according to the sum in Equation 2.9, with subscript 2ω denoting the upconverted photon at double the driving frequency ω.

$$k_{2\omega} = k_1 + k_2 + \delta k \tag{2.9}$$

k_1 + k_2 represent the theoretical wave vectors of two incident photons in the material. The rate at which HG occurs is maximized when δk is equal to zero [63]. However, away from resonance frequencies, refractive index increases slowly and monotonically with respect to frequency, making δk strictly negative and nonzero and preventing bulk SHG in most media. Birefringent and ordered non-centrosymmetric materials display strong SHG (and THG) because the lower refractive index of the fast axis can minimize δk for the right angle of incidence, and the right combination of photon polarizations. The efficiency of

HG then depends on the length over which the orthogonal polarizations are coherent, with the total amount varying in a sinusoidal manner depending on the propagation distance through the nonlinear medium [63]. If the material is disordered over a shorter length scale, HG will not occur at all due to destructive interference from out-of-phase radiation from misaligned dipoles.

In a tightly focused laser setup, the coherence length is large compared to the focal region where the intensity is high enough for nonlinear conversion. HG is instead limited by a different effect, the Gouy phase shift, wherein a focused beam experiences a phase shift of π as it crosses the focal point [20,84]. In this case a nonzero δk is necessary to avoid destructive interference from upconverted photons originating on opposite sides of the focal point [63]. Only off-axis wave vectors can accomplish this, so a negative overall δk is necessary [63,157], consistent with the propagation patterns of HG radiation [67,84].

Alternatively, the presence of materials with different refractive indices within the focal volume can satisfy the phase matching conditions and produce HG. Even two materials that are individually centrosymmetric will produce weak SHG in this scenario as the inversion symmetry is broken within the focal volume of the laser [158], producing the weak backward SHG observed in collagen fibers [76,87] and nanoparticles [67]. THG is especially sensitive to boundary conditions because of the nonlinear contribution to a material's refractive index dependent on χ_3 [63], making phase matching easier to achieve.

2.1.3 Polarization dependence of harmonic generation

In single-photon imaging, polarization is often either the primary focus of the modality or not considered. Simple polarization microscopy derives contrast from changes in polarization that occur when light scatters coherently from features in a sample, filtering out either phase-shifted or unchanged light to form an image. With fluorescence, absorption is more likely to occur when the laser polarization and dipole axis align, but rotational diffusion during the fluorescence lifetime produces emission at (usually) uncorrelated angles [20]. Fluorescence emission is generally treated as being effectively isotropic.

In multiphoton microscopy, this is not always the case. If the fluorophore has an intermediate absorption state, absorption of the second and third photons becomes more sharply confined to fluorophores that align with their polarization [159], leading to reduced fluorescence intensity [160,161]. Harmonophores also have preferred axes of polarization which, when in structures, are less free to undergo rotational diffusion. However, as explained in subsection 2.1.2, efficient HG depends on minimizing phase mismatch. The processes of coherent scattering of linearly and circularly polarized light are therefore somewhat different for both SHG and THG.

Under linear polarization where photons experience only one orthogonal pair of refractive indices, biological materials that are not crystalline over large regions will produce SHG selectively based on the alignment of the polarization axis with individual features [162] and interfaces [158]. This can be used effectively to determine orientation of dipoles [76,85,87,163] or avoided by using circular polarization, which interacts with all dipoles equally [70,73,88,164].

THG is much less sensitive to orientation of the polarization axis when using linearly polarized light [155,165]. Circular polarization is more complex: at an interface between two isotropic materials, the components of the nonlinear susceptibility tensor cancel out [166], suppressing THG from inhomogeneities. At least one of the materials must be weakly birefringent to produce a THG signal under this condition, and THG from an anisotropic bulk material will be unaffected [167,168]. This is the basis previously used to distinguish heterogeneous from homogeneous birefringent corneal tissue [164] and lipid ordering in cells [78].

2.2 Image processing in multiphoton microscopy

The particular physical requirements of HG, nonstandard excitation wavelengths of MPFM, and low conversion rates of both, introduce complications in terms of achieving a high SNR in the final image. Both random and nonrandom sources contribute to reduced

SNR in an image. This section gives a brief overview of sources of random noise and nonrandom aspects of NLSM that appear as artifacts, affecting the quality of the final output image. It also discusses ways in which the are mitigated, most of which are applied in some way in this work.

2.2.1 Random noise

Noise in multiphoton microscopy generally takes two forms: Gaussian white noise and Poisson-distributed shot noise in photon counts. White noise from detection hardware is a problem encountered in all forms of microscopy and can be addressed by time averaging or taking multiple samples, but when photon counts are very low (a particular issue in multiphoton microscopy) they follow a Poisson distribution [169]. Imaging deep into tissue increases scattering, compounding this issue [169]; the coherent nature of nonlinear scattering reduces the photon count even more if only one of forward- or backward-detection is available [162, 170]. The issue of noise is often addressed both in the image capture software and in post processing.

The most straightforward method of reducing noise is to capture and average multiple frames for each image. Whether to limit scan time or sample exposure, fewer repetitions are usually preferred. Given the low Poisson-distributed photon counts involved, probability-based methods such as variance-stabilized transforms (VSTs) and Kalman filtering [171] are preferred over simple averaging. This can be done independently for each voxel or using localized statistics. One drawback of such methods, which are often implemented directly in image capture software, is that they require some knowledge of the expected noise statistics, and need to be optimized specifically for the hardware involved.

On home-built or custom systems this may not address all sources of noise. Since NLSM requires nonstandard wavelengths at relatively high powers, the instrumentation may link a high power laser through one or more stages of nonlinear frequency conversion. Electrical, mechanical and thermal artifacts are amplified by the power law dependence of these processes into variability in the final output and must be taken into consideration

both while collecting and analyzing data. Even environmental noise sources unnoticed in linear fluorescence images with low-voltage detectors can appear in NLSM images. These systematic issues with external origins can be addressed through mathematical approaches that consider the totality of the image at once, although some can be dealt with using practical means like isolating the microscope from nearby sources of light.

2.2.2 Spatial filtering

Averaging serves primarily to reduce noise at the single pixel level, which limits it to noise on the scale of the pixel dwell time (microseconds). Artifacts spread over longer times or independent of time altogether may be distributed periodically throughout an image. Localized blurring from the diffraction-limited Gaussian shape of the excitation beam itself as mentioned in Section 2.1 can be addressed through deconvolution, but periodic artifacts may only be apparent when images are described in terms of spatial frequency components instead of spatial pixel values. This section considers filtering in terms of pixels in 2D, but all of it can be also extended to voxels in a 3D image.

In an extension of the 1D discrete Fourier transform, any 2D image can be Fourier-decomposed into a superposition of two-term complex exponentials where the x- and y-axis spatial frequencies map to a matrix with the same dimensions as the original image. The coefficient of each term in the decomposition defines the value of the pixel; the four quadrants correspond to the four permutations of positive and negative frequencies in the two Cartesian directions. In this way, low-frequency contributions that describe large-scale features in the image populate the centre, and concentric rings correspond to increasingly finer spatial scales. Indiscriminate high- or low-pass filtering can be applied by setting pixels either outside or inside of a given radius to zero and transforming back to real space.

Identifying noise in frequency space from an unknown source in a static image is, at best, unintuitive. A more subtle approach takes a small, carefully selected kernel and convolves it with the image to create a downsampled transformation. Doing this once with a kernel rotated along each axis, and once with a diagonal one, creates a set of three

high-pass filtered approximations. This can be repeated at multiple scales, and at each where obvious noise is present, it can be easily removed by zeroing pixels either locally or across the entire image. The original image can then be reconstructed from the filtered decomposition series. This was originally developed as the wavelet transform [172], but expanded into different kernels with the curvelet transform [173], and has applications in microscopy as well as many other fields [72, 174]. Non-local averaging adds to this approach by comparing small patches of an image and weighing patches based on their similarity to nearby patches, identifying patches that seem more likely to be highly affected by noise. These patches can then be singled out for more filtering with a kernel-based approach [175].

2.3 Quantitative image analysis techniques

While some questions are easily answered qualitatively, or by manual quantitative methods (such as counting or measuring relatively large, clear objects), others require an approach that can make use of the indistinct gradients in pixel values inherent to both diffraction-limited imaging and heterogeneous biological specimens. Specifically, image correlation spectroscopy (ICS) will be discussed here, because of its ease of implementation and the longer-range spatial patterns that it can detect. When images contain a great number of spatial and/or temporal features, which may each measure ten or fewer pixels across, collective analysis is best done either via statistics or automated segmentation and measurement of distinct, individual features. Both of these methods can produce a large variety of outputs and can be applied to answer diverse questions.

2.3.1 Image correlation spectroscopy

An early merger of statistics and imaging took the form of fluorescence correlation spectroscopy (FCS), where fluorescence fluctuations are recorded from the intensity time trace of a single excited focal spot as fluorescent molecules diffuse or flow in and out of fo-

cus [176]. The fluorescence intensity time series is then correlated with itself, and different models are fit to the resulting decay curve to measure transport modes and/or photophysical dynamics, such as diffusion, flow, and fluorophore blinking. [177]. Similar techniques have been applied with cosmology, using stars rather than fluorescent molecules as the source of fluctuating photon counts [178].

The correlation function of a data series is ostensibly produced by superimposing the data series on itself, recording the normalized sum of the product of each pair of points, then offsetting the superimposed series and repeating the calculation. This process is iterated until there is no more periodicity in the sample, generally well before the two series have been offset by their entire length. The output correlation function is expressed graphically by mapping the value of the integral at each incremental offset (lag) to the same axes as the original series. The data in correlation spectroscopy does not have to be a time series, but the interpretation of the output will vary for different contexts. Importantly, fluorescence correlation spectroscopy can only get information from a single point, and only about processes that occur on time scales for which the data series has been oversampled; the sensitivity of the decay curve increases with increased oversampling.

The FCS concept is extended into the imaging domain with ICS and image cross correlation spectroscopy (ICCS) and. In diffraction-limited microscopy with a Gaussian excitation beam profile, the decay of the 2D correlation function will have a Gaussian form if the pixelated image is oversampled relative to the diffraction limit. ICCS describes the spatial correlation of fluorescence fluctuations in two images or regions of interest (ROIs) $i(x, y)$ and $j(x, y)$ by producing an output $g_{ij}(\xi, \eta)$ with dimensions equal to those of the larger input, with the lag variables ξ and η representing pixel shifts in the spatial variables x and y [177, 179]. This output is normalized by the product of the mean values of each input. The discrete mathematical representation of this calculation for a 2D correlation calculated at all discrete pixel shift lags is given in Equation 2.10, with angular brackets indicating the average over all spatial coordinates [177].

$$g_{ij}(\xi,\eta) = \frac{\langle (i(x,y) - \langle i(x,y)\rangle)(j(x+\xi,y+\eta) - \langle j(x,y)\rangle)\rangle}{\langle i(x,y)\rangle\langle j(x,y)\rangle} \tag{2.10}$$

Due to the speed of the fast Fourier transform algorithm it is computationally more efficient to calculate the correlation function in frequency space through the Wiener-Khinchin theorem, which connects the correlation function of an image and its power spectrum as a Fourier transform pair. The power spectrum is the product of the Fourier transform of the image with its complex conjugate. This calculation is shown in Equation 2.11 for a normalized cross-correlation function, where F is the two-dimensional Fourier transform [177]. The ICCS equation can also easily be applied to a single image by making $j(x,y)$ equal to $i(x,y)$, which then describes the spatial autocorrelation of fluctuations in one image.

$$g_{ij}(\xi,\eta) = \frac{F^{-1}([F(i(x,y))] * [F^*(j(x,y))])}{\langle i(x,y)\rangle\langle i(x,y)\rangle} - 1 \tag{2.11}$$

Information about the image(s) is extracted using the parameters of the 2D Gaussian fit of this surface, referred to from here as the autocorrelation function (ACF). The general mathematical form of this fit, used for ICS in two dimensions, is given in Equation 2.12, where ω denotes the radius of the Gaussian along the respective lag axes [177] and g_∞ is the vertical displacement of the curve, or offset. Figure 2.2 shows how the width, amplitude, center and offset map to a perfect 2D elliptical surface. The same parameters identically describe the cross-correlation function (CCF) produced by ICCS.

$$g_i(\xi,\eta) = g_i(0,0)e^{-\left((\frac{\xi}{\omega_\xi})^2+(\frac{\eta}{\omega_\eta})^2\right)} + g_\infty \tag{2.12}$$

Particularly relevant to this work, the spatial correlation function can give aggregate information about discrete features in the image. It is frequently evaluated for images of sub-diffraction sized beads to verify the size of the PSF as part of microscope alignment; in this case the width of the spatial ACF is directly proportional to the width of the PSF. However, if imaging features above the diffraction limit, the width of the spatial ACF will

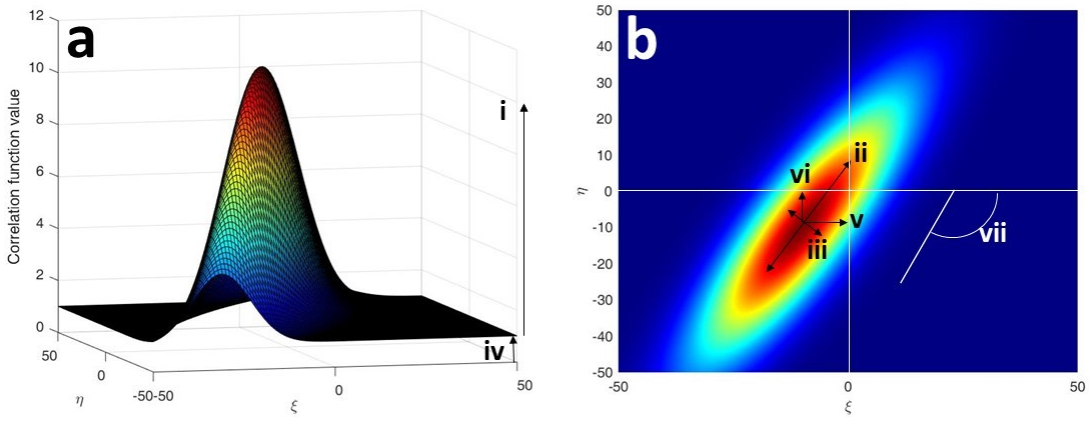

Figure 2.2: Example of a perfectly Gaussian 2D correlation function surface showing the physical meaning of the Gaussian fit parameters: (a) three dimensional view of the amplitude (i) and offset (iv); (b) 2D top-down view showing the major axis width (ii), minor axis width (iii), x-axis center (v), y-axis center (vi), and rotation angle (vii). Arrows indicate scalar spatial measurements. Lag variables are given in terms of discrete pixels.

have a dependence on the scale over which the features decorrelate with themselves in the image [119, 180]. If the features are close to the diffraction limit and therefore exhibit significant Gaussian blur, it should be possible to extract meaningful information using a Gaussian fit; if they are much larger than the PSF, the ACF will exhibit a non-Gaussian plateau, distorting the fit parameters. For highly anisotropic images some difference would be expected between the major axis (corresponding to the lengthwise dimension) and the minor axis (corresponding to the widthwise dimension); conversely no significant difference would be expected if the image was homogeneous and showed no preferred orientation.

Another parameter of interest is the value of the peak of the ACF, $g_{i,j}(0,0)$, which is related to the cluster density (CD) of fluorophores in the image [181]. It can be used to determine information about membrane receptor clustering and oligomerization [182]. In ICS, the relationship is simply inverse to the density, but in ICCS dividing the CD of the cross-correlation by the autocorrelation CD_i of one of the two images indicates the percentage of clusters in the other image j that are colocalized with those in image i;

Equation 2.13 gives this relationship as defined by Petersen [177]. Combining the two gives the average number of colocalized clusters per beam area independent of non-colocalized clusters elsewhere (shown in Equation 2.14 from Constantino et al. [183]).

$$F(i|j) = \frac{CD_{ij}}{CD_i} = \frac{g_{ij}(0,0)}{g_i(0,0)} \tag{2.13}$$

$$\langle N_{12} \rangle = \frac{g_{ij}(0,0)}{g_i(0,0) * g_j(0,0)} \tag{2.14}$$

2.3.2 Feature classification

In contrast to correlation analysis which averages features over noisy signals or images, direct feature analysis such as particle counting and fiber fitting is possible if contrast and resolution are sufficiently high and there is sufficient separation between features. Thresholds can be set for what qualifies a certain shape or pattern as a target feature in order to perform segmentation and analysis algorithmically. Automated approaches such as identification based on probability [161, 184] or machine learning [185] are preferable in many situations where a data set contains many instances of a feature, especially if output metrics are more complex than a single measurement. The approach has been applied repeatedly to study fibrillar structures, analyzing the impact of fibre length, thickness, and packing density on the Gaussian parameters, as well as connecting these to the effective pore size of the structure [72, 186]. One caveat to this approach is that automated feature recognition can be hard to validate manually when looking at images with features that are too faint or vague to be detected above the background before filtering. Unsupervised filtering can lead to anomalous results and conclusions; it is often better to cross-validate the analysis with other approaches first [187].

2.3.3 Principle Component Analysis

The various outputs produced by ICS and feature classification may themselves answer biological questions. However, in heterogeneous biological systems where there is often a large amount of variation both between and within samples, considering any one variable may not give a statistically significant result. One solution is to run many samples so that standard deviations are small. If this is not an option, or if there are many competing metrics that individually do not contain sufficient variance to draw conclusions, a better option is principle component analysis (PCA) [188]. It can be used both to measure the significance of various factors in a system [189] and to simply classify samples in a large, multidimensional dataset [190].

PCA uses linear algebra on a normally distributed dataset of two or more dimensions to rotate the coordinate system so as to maximize the amount of variance contained along a single axis. For a 2D dataset, the perpendicular axis then contains the rest of the variance; if there are additional dimensions, PCA orients and orders them such that each subsequent axis captures as much of the remaining variance as possible. Each can also be decomposed to see the relative contributions of each input dimension.

Correspondingly, each input dimension can be described in terms of its contribution to each principal component; this can be projected into principal component space using a biplot, which displays each input as a vector with magnitude along each principal axis equal to the relative weight of the input on that component. This allows for quick, manual identification of which variables contribute a significant amount of variance to the overall transformation. It also identifies correlated input variables, which will be close to parallel in the biplot projection. Plotting the transformed data points in principal component space can also emphasize or reveal clustering that may not be apparent if only considering the input variables independently, differentiation subgroups of samples within a larger dataset [188].

Chapter 3

Materials and Methods

3.1 Nonlinear microscope instrumentation

Imaging was performed using a home-built multiphoton laser scanning microscope, shown in schematic form in Figure 3.1.

A 532 nm Verdi V-18 InGaS optically pumped semiconductor laser (Coherent) running at 11 W output was used to pump a Mira 900F Ti:Sapphire laser (Coherent) which produced a 200 fs, 86 MHz pulsed 780 nm output. This laser output was fed into a Mira optical parametric oscillator (OPO) (APE) with a fs-regime periodically-poled crystal, which could be tuned to produce an output laser with a wavelength between 1050 nm and 1200 nm at approximately 200 mW. Spectral information was sampled with a 1050-1700 nm beam sampler (Thorlabs) directed at a Wavescan Laser Spectrometer (APE) connected to an OPO PP Analyzer (APE), and was used to align the optics in the OPO and select the excitation wavelength.

A pair of mirrors in the beam path were used to make coarse adjustments to straighten and center the propagating beam on an achromatic 690-1200 nm half waveplate (Thorlabs). This was placed immediately before a thick birefringent crystal and was used to control the excitation power sent to the microscope by rotating the waveplate relative to the fast axis of the crystal. Excitation power was controlled using a custom Labview program

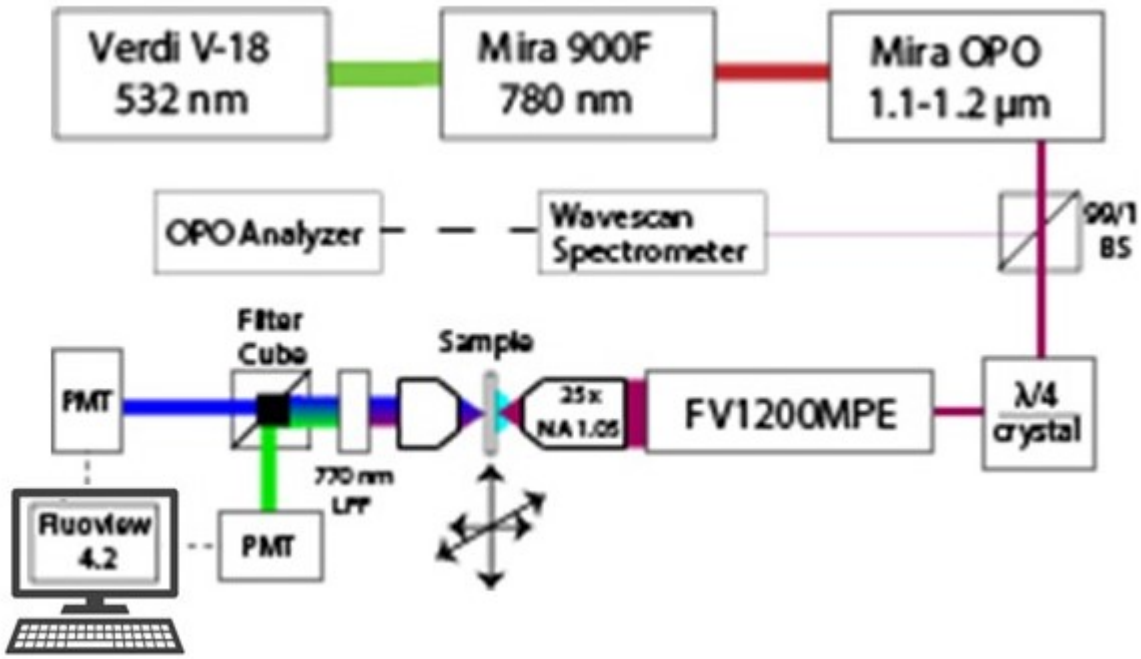

Figure 3.1: Nonlinear microscope instrumentation indicating (in sequence): three laser components; beam sampler (BS) & spectral analysis hardware; half waveplate/birefringent crystal power control module; optional quarter waveplate; Fluoview laser scanning microscope; nonlinear excitation objective; three-axis motorized sample stage; collection objective; 770 nm low-pass IR filter; filter cube containing 425 nm dichroic beam splitter, 600/60 nm band pass filter for 2PF and SHG signal, and 400/40 nm band pass filter for THG signal; PMTs for signal collection; Fluoview 4.2 software for microscope control.

which read the laser power from a power meter (Thorlabs) placed just before the scanning hardware. For all experiments, a power at the meter of 100 mW was used, which translated to 50 mW at the plane of the sample. Following the power control module a 400-1100 nm achromatic doublet was used to correct for aberration.

Polarization was controlled using an achromatic 690-1200 nm quarter waveplate (Thorlabs) to switch from linear to circular polarization as necessary, placed several centimeters after the achromatic doublet. Mussel samples were all imaged with linearly polarized light and images of tadpole samples were acquired once with linearly polarized light, then again with circularly polarized light.

The microscope base was an FV1200MPE (Olympus). Two mirrors at the start of the beam path provided fine control over beam centering and straightness prior to two servo-controlled raster scanning mirrors, which directed the beam into a scanning lens/telecentric tube lens pair. The microscope was equipped with a water-immersion XL-SLPLN25XWMP2 objective lens (Olympus) with a 1.05 NA, 25x magnification, working distance of 2 mm and a chromatic correction collar. The collar was adjusted based on the thickness of the cover slips being used to achieve the highest resolution possible based on calibration with 0.1 µm red-fluorescent (580/605 nm) Fluospheres (Invitrogen) mounted in ProLong™ Diamond Antifade Mountant (Invitrogen). The correction depth was increased for imaging deeper into samples as appropriate.

Forward propagating signal was collected by a 0.9 NA dry top lens condenser (Olympus) and filtered with a 770 nm edge-pass infrared filter (Semrock) to remove excitation light. A filter cube containing a dichroic beam splitter with a splitting wavelength of 425 nm (Olympus) was used to separate the two- and three-photon signals. The high- and low-pass directions contained band pass filters with band windows of 600/60 nm (2PF, SHG) and 400/40 nm (THG), respectively. Each signal was focused on the active area of separate photomultiplier tubes (PMT). Imaging was conducted using Fluoview software (Olympus) to control scanning hardware, PMT gain and data pre-processing via thresholding and pixel-based Kalman filtering. Settings were chosen based on individual samples to optimize image SNR and contrast and are reported in Chapter 4.

3.2 *Mytilus Edulis* sample preparation

Mussels (*Mytilus edulis*) were purchased from Prince Edward Island, Canada (Prince Edward Aqua Farms, PEI) and kept live in artificial seawater (ASW). Once mussels had grown threads in the new tank environment the plaque (distal end) was removed from the tank wall by scraping with a scalpel. The thread was then cut at the proximal end as close

as possible to the stem. Threads were kept stored in ASW at 5° C. Threads were kept for imaging up to six months after collection.

Thread slices were prepared by freezing individual threads in a cryotome chamber at -20° C, then cutting 4 µm sections and mounting them directly on microscope slides. The slides were immersed in Boin's solution overnight, then placed in a 0.1% solution of Sirius red dye in saturated picric acid (PsR) for 1 hour. After this they were washed in 0.5% acetic acid and dehydrated through a series of ascending ethanol concentrations. They were then transferred to a bath of Neo-Clear xylene substitute (Sigma Aldrich). Finally, they were mounted on standard microscope slides using Neo-Mount (VWR) and covered with #1.5 coverslips. They were stored at 5° C and imaged for up to six months after preparation. Whole threads were imaged by mounting them on cover slips in their storage medium (ASW) and sealing the cover slips with nail polish to prevent them from drying out. Samples were imaged immediately and stored at 5° C for future reference or replicate imaging. Figure 3.2 shows sample slides prepared of whole and sectioned threads.

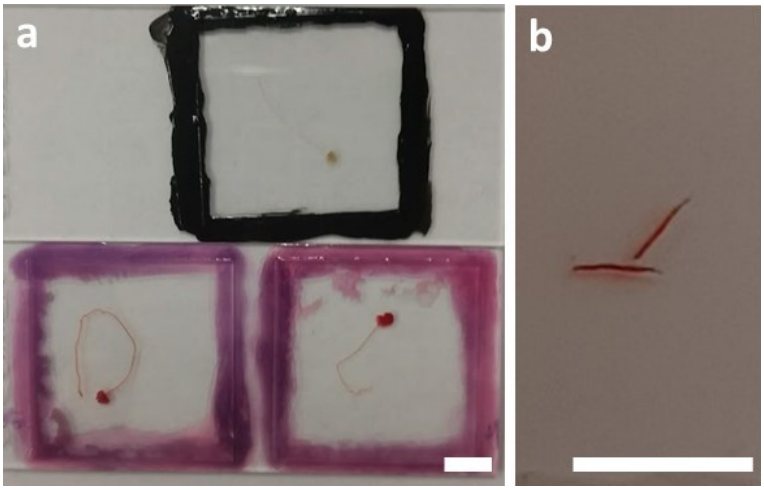

Figure 3.2: Whole mussel byssal threads prepared on slides: (a) unstained (upper) and stained with picrosirius red (lower); (b) sectioned and mounted threads stained with picrosirius red. Scale bars 0.5 cm.

Optical clearing of whole threads was performed using the 3DiSCO protocol, a method of clearing tissues with solvents to match refractive indices and reduce light scattering

for volumetric 3D imaging [191]. The refractive index of the cleared specimen is ideal for imaging with oil-immersion objectives, but collagenous tissues cleared with a similar method to the same refractive were previously imaged successfully with this microscope system [73]. Threads were taken from ASW and immersed in a series of increasing concentrations of tetrahydrofuran (THF) in distilled water: 50%, 70%, 80%, and 100%, for 20 minutes each. They were then transferred to a bath of pure dichloromethane for 15 minutes before being rinsed in a bath of dibenzyl ether (DBE) and transferred to a fresh vial of DBE for storage. For harmonic hamonic generation imaging, threads were mounted on glass slides with #1.5 coverslips in DBE as a mounting medium and imaged immediately. All imaging was performed within 7 days of clearing but samples are expected to be viable for months after preparation [191].

3.3 *Xenopus Laevis* sample preparation

Specimens were raised and fixed according to the process described in Chorghay et al. [192]. In brief, *Xenopus* eggs were raised from birth in normal light conditions to promote normal development of the optical portions of the nervous system. Specimens were anaesthetized at stages 51, 52, and 53 of their development and the hindbrain and optic tectum were extracted from the brain; these stages had previously been identified as the period at which myelination occurs in these areas in a healthy tadpole. These were chemically fixed in 4% paraformaldehyde, washed, and cryoprotected in a solution of 20% fish gelatin (Norland HP-03) with 15% sucrose. 20 µm slices were acquired using a crysostat and mounted on Superfrost-plus slides (Fisher) using Aqua-Polymount (Polysciences).

Antibody staining for myelin basic protein was performed using rat anti-MBP antibody (1:200; Abcam [clone 12] ab7349; RRID:AB_305869) and goat anti-rat IgG Cy3 (1:200; Jackson Immunoresearch 112-165-175; RRID:AB_2338252). Neurons and axons were also labelled using mouse 3A10 (1:400; DSHB Hybridoma Product 3A10; RRID:AB_531874), which was counterstained with goat anti-mouse IgG Alexa-647 (1:200; Invitrogen A21236;

RRID:AB_2535805). Cell nuclei were counterstained with DAPI (1:1000; Invitrogen D-1306; RRID:AB_2629482). One set of samples was also prepared using only the MBP staining. Slides were stored at -20° C between imaging sessions.

3.4 Image Processing and Analysis

Image processing and analysis was performed using existing packages in Matlab and ImageJ and additional custom scripts in Matlab. The Bioformats Reader plugin in ImageJ [193] was used to read the output images from Fluoview and save them as multi-channel TIFF images. All images were converted from 32-bit to 8-bit formats before being analyzed. Control images were created by breaking each image up into evenly sized blocks of 5 to 40 pixels, which were then given a random number of quarter turns and rearranged randomly to spatially scramble the image as done previously by Aaron et al. [194]. The size of the blocks was chosen empirically based on the size of the features in the image to minimize the size of the threads in the shufled blocks.

3.4.1 Image processing for mussel samples

Mussel images were manually segmented to isolate sub-regions containing only the core, to avoid the strong signal from the thread-water interface and bright spots scattered within the sectioned threads. Subregions selected were at least 130 pixels in any direction to minimize random outlying data points during analysis. This specific constraint was also required by the Matlab package used to perform fiber analysis, CT-FiRE.

CT-FiRE was developed to perform fiber identification and quantification by Bredfeldt et al. [72]. It was developed for, and has been overwhelmingly applied to, collagen systems, but has also been implemented with actin fibers [195,196]. It uses a curvelet transform filter to remove noise without affecting fiber shapes, with improved ability to highlight lines and edges. It then traces fibers by choosing bright spots in the image as likely nucleation points and tracing out from them in all directions, selecting two directions in which the

fiber appears to proceed, and repeating the process until the feature ends (or becomes indistinguishable from the surrounding region). Thresholds can be set for the maximum average width and minimum length of recorded fibers, rejecting any full features outside of these limits. For each image, a list is produced of the length and average width (measured in pixels) of each fiber within the image. CT-FiRE also measures the straightness (the ratio of the distance between the start and end points to the total length of the fiber, so that a value less than 1 indicates increasing curvature) and relative angle (between the vertical axis and the line formed by connecting the start and ends points) for each fiber.

Correlation analysis was performed using a custom Matlab script which calculated the 2D spatial autocorrelation function for all channels in each image, and the spatial cross-correlation function between them for two channel images. A rotationally free bivariate 2D Gaussian function, based on code written by Dave Kolin and incorporating the rotational component from a script by Diaz [197] was used to fit the correlation surfaces and the seven parameters (amplitude, standard deviation in x and y, peak location in x and y, offset at infinity, and angle from the x-axis) were stored with the CT-FiRE output values for analysis.

3.4.2 Image processing for tadpole samples

Tadpole images were first processed by removing unwanted signal via image subtraction (see Section 4.5.3). They were then denoised using CANDLE, an ImageJ plugin developed specifically for volumetric imaging deep in biological specimens where SNR is often low [198], scattering is high, and photobleaching and phototoxicity are undesirable side effects of long exposure times [199]. It uses patch-based denoising which has proven useful in low-count fluorescence applications [175]. Figure 3.3 shows the workflow of the filter.

It first prefilters the image using a median filter, then applies a variance-stabilized transform to correct the Poisson-distributed noise in photon counts across the image into Gaussian noise. A map of weighted voxels, produced from the pre-filtered image, is then used to locally adjust the relative amount of smoothing. The degree of smoothing is also

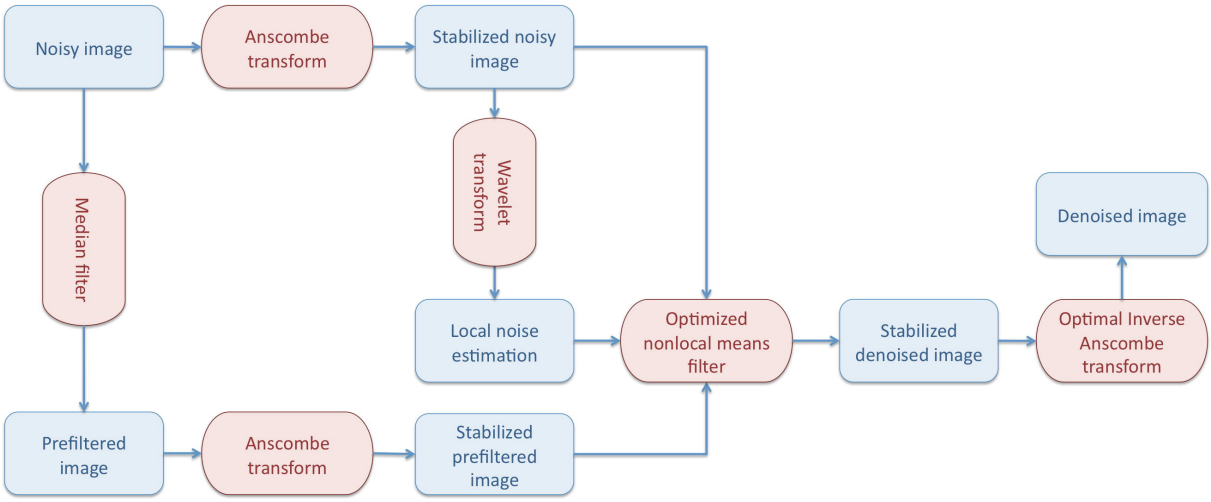

Figure 3.3: Workflow diagram of the CANDLE denoising filter (reproduced from [198], with permission from Elsevier)

adjusted globally by stabilizing the raw image with the same VST and applying a wavelet transform to extract the highest spatial frequency details. This gives an estimate of the overall random noise. The map of weightings and overall noise estimate are then applied to the stabilized, noisy image, and the inverse VST transform is performed to arrive at the fully denoised image.

Images produced through CANDLE contained periodically spaced NaN artifact pixels in both channels, which were replaced prior to analysis by the average of the four immediately adjacent pixels. Filtered images were then analyzed using CT-FiRE and the same Matlab script used to perform spatial correlation analysis on the mussel samples. Monochromatic images for CT-FiRE analysis were produced by pixelwise multiplication of the two single-channel 8 bit images to produce 32 bit images, which were then converted back to 8 bit images.

Chapter 4

Nonlinear microscopy imaging and image analysis of tissue samples

The objective of this chapter is to combine the principles of multiphoton contrast generation and image analysis outlined in Chapter 2 with the biological models and questions discussed in Chapter 1. It aims to demonstrate that the former can elicit statistically significant variations between datasets in the biological systems of the latter, namely the proximal, transition and distal zones of *Mytilus edulis* byssal threads, and the developmental stages of *Xenopus laevis* tadpoles.

Section 4.2 covers the alignment process and determination of the PSF for nonlinear imaging modalities by imaging diffraction-limited microspheres. Sections 4.3 and 4.4 apply SHG and THG microscopy to the byssal thread system, analyzing simultaneously acquired two-channel images of the core and cuticle. In the core ICS and fiber fitting are used to quantify the spatial gradient of structure in the collagen-like core; in the cuticle ICS is used to demonstrate that NLSM is a viable way to investigate compacted proteinaceous domains. In Section 4.5 multimodal NLSM is employed to image progressive compaction of myelin of the axons of optic nerves, and ICS and fiber fitting are examined for their potential to quantify this change in this and future work.

4.1 Universal imaging parameters

All work except the acquisition of TEM images was done using the nonlinear microscope instrumentation and sample preparation methods detailed in Chapter 3. Due to the varying quality of alignment, as well as sample heterogeneity, brightness varied widely between images. This informed the decision later to focus on quantitative metrics that did not depend on the relative intensity between samples. For consistency, pixel dwell time was set to 12.5 µs with a three-pass Kalman filter, which gave qualitatively good SNR with reasonable image capture times. Zoom varied depending on the size of the sample but pixel size was kept roughly constant by changing resolution. PMT signal gain was adjusted during preliminary scanning of samples (either setting upper and lower limits in the Z direction, registering tracks for multi-tile captures, or both) so that the brightest features were at the edge of saturation. SNR values, pixel size ranges, and gain settings are all reported in their respective sections.

4.2 Verification of microscope alignment and imaging PSF

For a custom built microscope with multiple lasing stages driven by one seed laser, the system can be highly dependent on the alignment of that initial beam. The Verdi-V18 system uses a temperature-controlled birefringent crystal to double its frequency via SHG, and required an extended period to thermally stabilize after startup. The inconsistent stabilization point and highly directional nature of nonlinear processes in the Mira 900-F meant that the mirrors in its cavity often had to be adjusted on startup to maximize the output power sent to the Mira OPO. The optics in the OPO were then aligned if necessary to maximize conversion to the imaging wavelength. Lasing could be achieved across a window from roughly 1050 nm to 1200 nm by adjusting the length of the OPO laser cavity, but the alignment had to be repeated iteratively to maintain high output power if changing the output wavelength by more than 40 nm. Lastly, the adjustable mirrors between the

OPO and the scanning hardware were used to straighten and centre the beam by centering it on crosshairs placed at alternating locations along the beam path.

The complete process was verified by acquiring z-stack images of diffraction-limited fluorescent beads (maximum absorption at 580 nm, maximum emission at 650 nm) and adjusting the beam angle until the THG signal from the beads was maximized and the circular THG signal from the glass-mounting medium interface was centered. An example two-channel calibration image is shown in Figure 4.1.

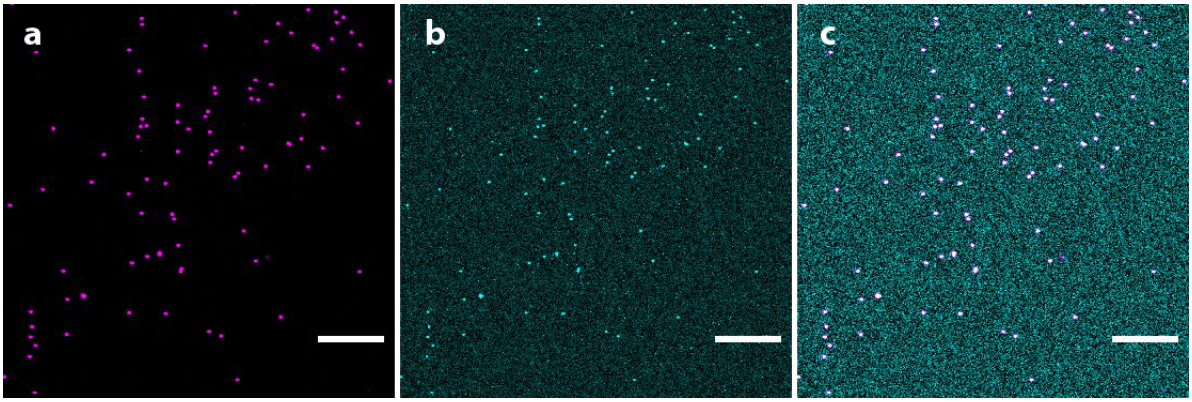

Figure 4.1: Calibration images of 100 nm diameter carboxylate-modified polystyrene spheres imaged with SHG (a), THG (b) at 1140 nm excitation. The overlay of the two images is shown in (c) . Scale bars 50 µm.

These images were used to determine the experimental PSF of the microscope by performing ICS on each channel and taking the average of the width of the Gaussian surface along each axis. Table 4.1 compares the theoretical lateral PSFs reported in Table 2.1 to the experimental lateral PSFs for 2PF and 3PF. Axial resolution was not measured since no analysis was performed in the axial direction, but beads were in general visible across several 1 µm slices, much greater than the theoretical limit. SNR values were measured by comparing the standard deviation of the pixels in a background region to the average value of the bead. SNR values for the SHG channel were extremely high, with almost all images having the maximum possible value for an 8-bit image of 255. SNR in the SHG channel ranged from 3 to 36, with an average value of 14.

Modality	Theoretical XY resolution (nm)	Experimental XY resolution (nm)	Median SNR
2PF	510	740 ± 190	255
3PF/THG	340/200	290 ± 80 (THG)	14

Table 4.1: Theoretical and experimental lateral resolution of the nonlinear scanning microscope for 2PF and 3PF/THG imaging using 50 mW, 1140 nm excitation of 100 nm fluorescent beads, with maximum absorption at 580 nm and maximum fluorescent emission at 605 nm.

The PSF measured by 2PF is consistent with expectations for the high-NA water immersion objectives used here [200, 201]. The fact that the PSF measured by THG is so much smaller and appears to be below the diffraction limit altogether is consistent with both theory [154] and direct measurements of the Gaussian FWHM in other work [202]. In theory, the 2D projection of the volume within which 2PF is produced in is distorted strictly by aberration in the optical path causing absorption and emission to occur in a region larger than a single scanning voxel. On the other hand, coherent nonlinear scattering is also strongly dependent on alignment, so the response to aberration is not the same. Out-of focus 2PF caused by aberration will increase the size of the image of diffraction-limited beads, while interface-dependent THG is only possible at the focal point where the Gouy phase shift occurs. Consistent with this, during alignment beads would generally grow from very tiny points to fuller, brighter spots as the alignment was corrected, and beads towards the edge of the field of view would remain smaller than those at the center.

The large uncertainties are possibly explained by the fact that the images were not heavily oversampled relative to the diffraction limits. The amount of background noise also varied between images, which may not always be completely compensated for by background removal. This is intended as a general measure of how close the system comes to diffraction-limited imaging rather than a definitive measurement of the PSF.

4.3 Identifying the transition region in the byssal threads of *Mytilus edulis* using harmonic generation

The primary goal of using multimodal scattering microscopy to image the threads was to demonstrate its utility as an additional method of exploring the structure of the preCol fibers in the collagen-like core. This can be done with either whole or sectioned threads, with the former being more representative of the *in vivo* condition, while the latter offers better resolution and SNR. Additionally, two analytical methods are applied (image correlation spectroscopy and automated fiber fitting) to see whether the three regions of the fiber (proximal, transition, and distal) can be distinguished quantitatively. The two methods are compared both together and independently using PCA, and also by applying them to TEM images, to see if either one alone is sufficient to do so.

4.3.1 Image acquisition and preparation

Exploratory wide field imaging of whole threads, stained with picrosirius red for visibility, confirmed that the preCols appeared to form long, fibrillar structures very similar to mammalian collagens. Figure 4.2 contains sample images showing the rippled surface of the proximal region, with lateral wrinkles clearly visible, becoming more structured in the transition region and being well organized in the distal region. This supported the idea that correlation analysis and fiber fitting using CT-FiRE were both potentially useful tools to quantify the structure of the thread using HGM.

The first images acquired with the scanning microscope were of whole threads mounted in ASW to confirm the presence of nonlinear scattering within mussel fibres. Figure 4.3 shows a 3 µm stack of a twisted hairpin in the proximal region of an intact thread. THG is clearly visible along the wrinkled surface (Figure 4.3a), while SHG is visible from the bulk (Figure 4.3b), but no internal structure was apparent.

Sectioned threads were then prepared to see if it was possible to acquire clearer images of the interior structure. Both stained and unstained threads were prepared as described

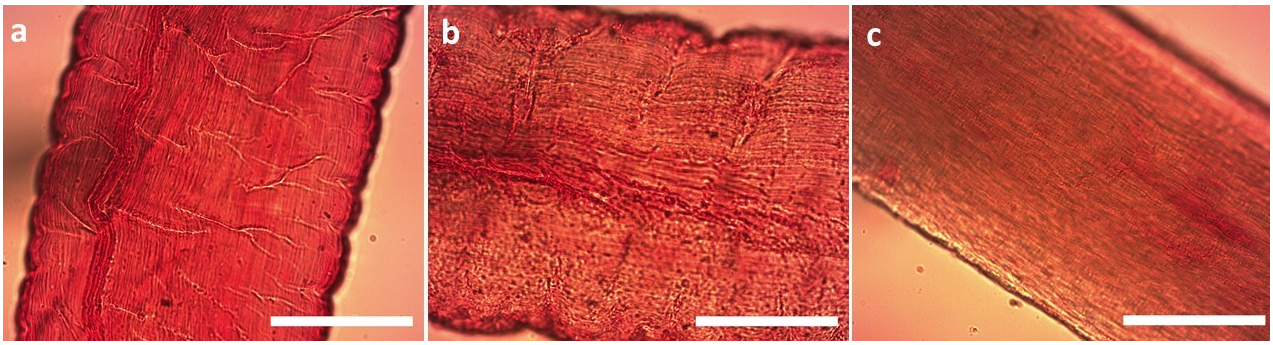

Figure 4.2: Wide field images of intact picrosirius red stained whole threads: proximal region (a), transition region (b), distal region (c). Scale bars 50 µm.

in Section 3.2. Images were captured as tiled sets to cover individual thread slices up to 5 mm long and stitched together for display using the grid stitching plug-in for ImageJ developed by Preibisch et al. [203]. Figure 4.4 compares the THG (a,b) and SHG (c,d) channels of one stained (a,c) and one unstained (b,d) thread. Dim areas are clearly visible at the edges of the stitched components; overlap was minimized to reduce scan times at the expense of imperfect reconstruction.

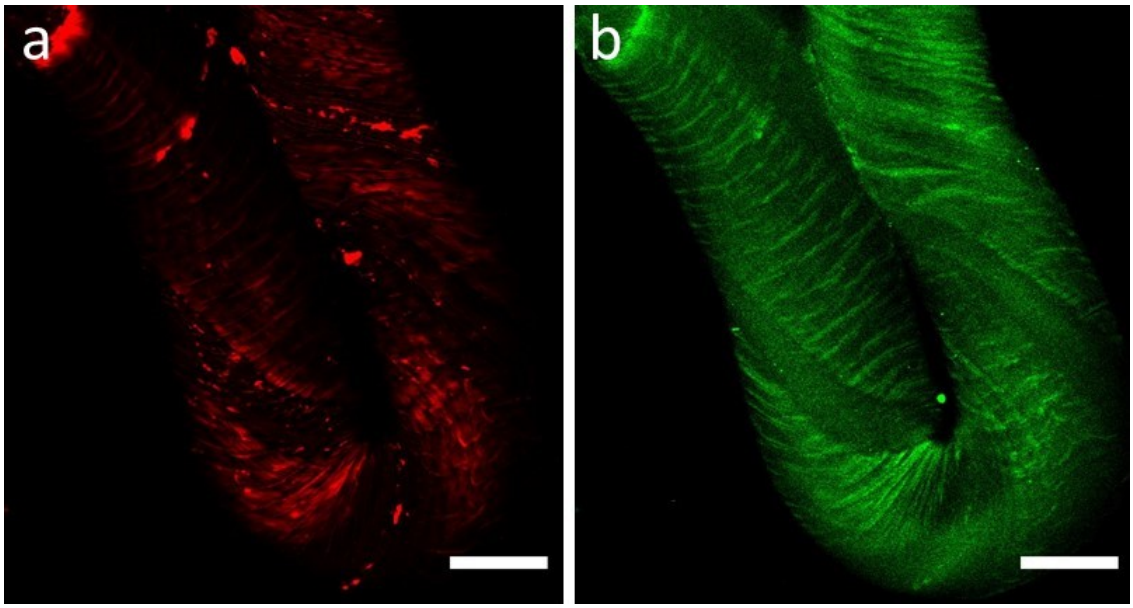

Figure 4.3: Sample images of harmonic generation in an intact proximal thread excited at 1140 nm; THG produced at 380 nm (a) and SHG produced at 570 nm (b). Scale bars 50 µm.

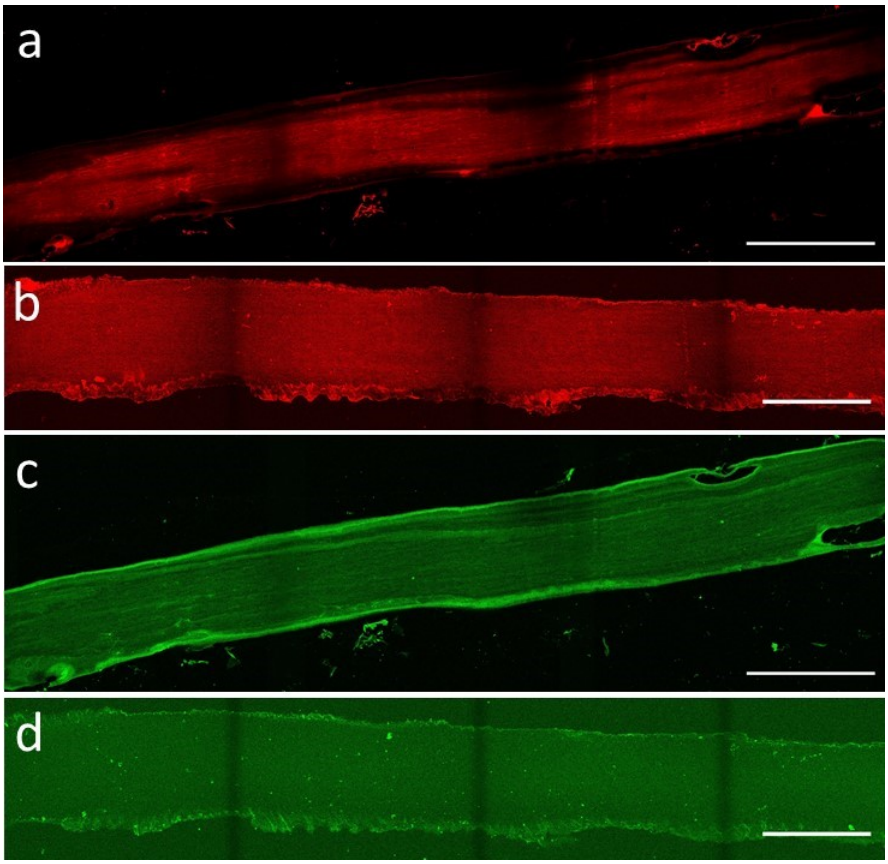

Figure 4.4: Stitched outputs of overlapping images taken of sectioned proximal region threads, showing THG (a,b) and SHG (c,d) produced at 1140 nm of one picrosirius red stained (a,c) and one unstained thread (b,d). Scale bars 200 µm.

The staining process clearly improved both the SHG and THG signals qualitatively, and also made the structure within the threads visibly apparent. Imaging was performed using the stained, sectioned threads since the high contrast fiber structures showed the most promise for both ICS and CT-FiRE analysis.

Images were acquired under settings that varied slightly between sessions but used a consistent excitation power of 100 mW. The voltage gain of the PMT detecting the three-photon bandwidth was set to between 325 V and 450 V, with a median value of 430 V. The PMT detecting the two-photon bandwidth was set ranging from 665 V to 750 V with a median value of 750 V. All images were acquired with a 12.5 µs pixel integration time and 3x line scan Kalman filtering. Pixel sizes varied between 0.254 µm and 0.318 µm depending

on the magnification and resolution used, which varied from 1.5 to 2 and 1024 by 1024 to 1600 by 1600, respectively. These variations are accounted for in the outputs of both analysis pipelines. Individual frames were all roughly 350 µm long on each side.

The signal to noise ratio in the was measured by tracing individual threads in each channel and dividing the average value by the standard deviation along the trace. Forty threads were measured per region in each channel. SNR varied significantly between images but was approximately 5 in the THG channel and increased from 2 in the proximal end to 5 in the distal end in the SHG channel. However, it is important to note the arbitrary nature of this definition, as staining and biological variability play a significant role here. SNR comparing the samples to the background generally measured no lower than 15 and as high as 100.

4.3.2 Analysis using ICS and CT-FiRE

Prior to analysis, strong harmonic signals were observed qualitatively at the edges of the sectioned threads, in addition to speckling that varied between samples and scattered dark spots in the threads; it was unclear if these were possibly shear damage from the microtome or foreign contaminants captured during slide preparation. ICS in theory would be affected by the bright artifacts, and thread fitting was prone to tracing both the edges and the perimeters of spots. To avoid having these impact the analysis, rectangular ROIs covering as much artifact-free signal as possible were manually segmented from each unstitched frame. These 2-channel sub-images were at least 128 pixels per side due to size limits of the CT-FiRE algorithm.

These ROIs were run through CT-FiRE to get fiber fitting statistics, which were then read by a Matlab script that also calculated and fit the ACF for each sub-image. All ROIs from each individual frame were averaged together and registered as individual data points (frames with only one ROI were not averaged). Figures 4.5 and 4.6 show each step of this process in the proximal and distal regions, respectively. Both figures show the THG image of the subregion (a), the autocorrelation surface of this image to which the

correlation function is fit (b), the curvelet-filtered image produced by CT-FiRE (c), and the overlay of the fitted fibers identified by the algorithm (d). The same sequence of images is given for the SHG image in (e)-(f).

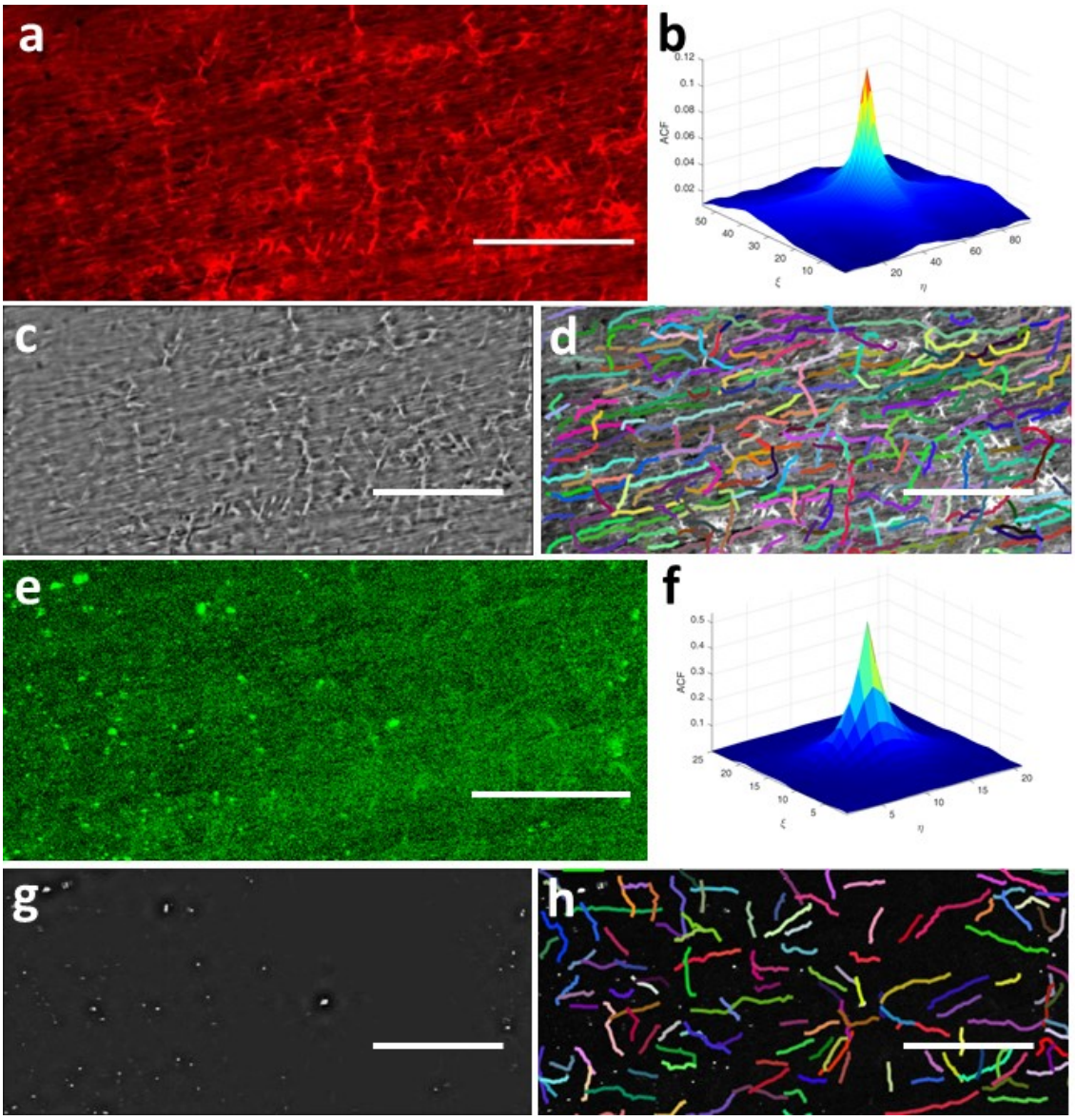

Figure 4.5: Sample images of sectioned proximal threads with respective analytical outputs. Left to right, from top: (a) THG image of proximal region thread; (b) 2D spatial ACF of (a); (c) curvelet-filtered CT-FiRE output image; (d) overlay of fitted fibers on (a); (e) SHG image of the same region as (a), acquired simultaneously; (f) 2D spatial ACF of (e); (g) curvelet-filtered CT-FiRE output image; (h) overlay of fitted fibers on (e). Contrast in (d) and (h) has been reduced by CT-FiRE but pixel values are unchanged. Scale bars 50 μm.

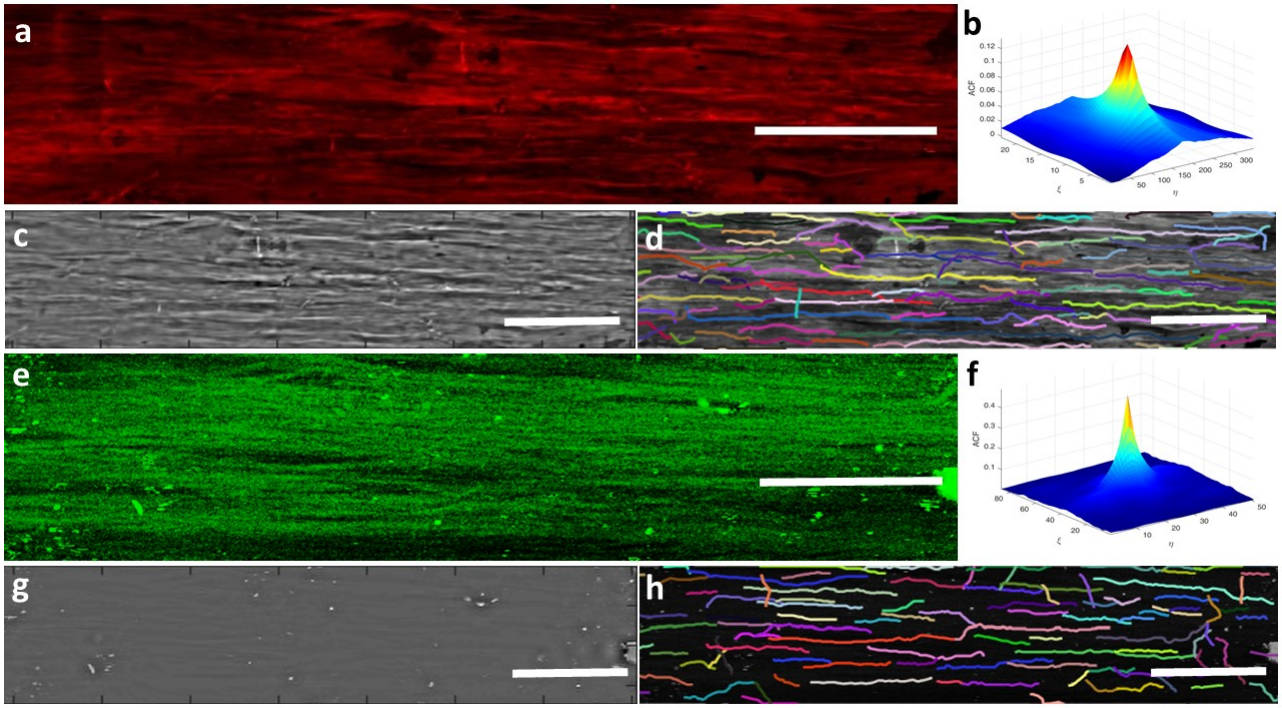

Figure 4.6: Sample images of sectioned distal threads with respective analytical outputs. Left to right, from top: (a) THG image of distal region thread; (b) 2D spatial ACF of (a); (c) curvelet-filtered CT-FiRE output image; (d) overlay of fitted fibers on (a); (e) SHG image of the same region as (a), acquired simultaneously; (f) 2D spatial ACF of (e); (g) curvelet-filtered CT-FiRE output image; (h) overlay of fitted fibers on (e). Contrast in (d) and (h) has been reduced by CT-FiRE but the pixel values are unchanged. Scale bars 50 µm.

The combined analysis produces four outputs of interest from fitting the ACF: amplitude (which is converted to cluster density), FWHM width in the x- and y-direction, and the offset from zero at infinity. Since the assignment of the x and y axis depends entirely on the orientation of the sample on the slide, the x and y widths of were reassigned as the major and minor axes based on their relative values. Three more outputs come from the CT-FiRE data: average fiber straightness, average fiber width, and average fiber length. The quality of the Gaussian fit was included as an additional parameter, measured as the sum of the residuals divided by the total number of pixels, as well as two permutations of other metrics: the cluster density ratios for each channel representing the colocalization

across channels (as described in Section 2.3.1) and the ellipticity (the ratio of the major axis to the minor axis in the ACF). This gave a total of nine outputs.

All outputs were considered for their ability to distinguish between the proximal, transition and distal regions using a one-way parametric Anova test between the three groups, with post-hoc comparison between each pair of groups. Data was log-transformed for all metrics involving ICS outputs before performing statistical analysis, which is standard practice because they are often very small and restricted to non-negative values.

In theory, both analyses should respond to the same features in both channels, and they should show similar behaviour, but this was not the case in practice. This is understandable given that the targets of the two techniques are expected to be co-localized but are not exactly the same. Table 4.2 summarizes the conclusions of this analysis for all of the variables that showed a discernible trend, in order of lowest to highest average p-value. Specifically, metrics were singled out which showed both significant p-values and monotonic behaviour across the three regions.

The major axis width, ellipticity, fiber straightness, and fitted fiber length showed consistent, statistically significant behaviour in both channels. The minor axis width and fitted fiber width were neither consistent nor significant in the THG channel, but both consistent and significant in the SHG channel. The offset showed a general decrease from the proximal to the distal end. The goodness of the Gaussian fit as measured by the sum of the residuals showed significant decrease in the SHG channel only, but this metric is susceptible to outliers because of the extremely small values ($\sim 10^{-4}$).

The cluster density showed monotonic behaviour in both channels; however, the THG value increased going from the proximal to the distal end, while the SHG value decreased in the same direction. Only the latter was statistically significant. This may be a result of stain being more evenly distributed in the ordered distal end, whereas SHG from more organized fibrils is less likely to interfere destructively and therefore appears brighter. The cluster density of the cross correlation showed no trend or statistical significance, nor did the cluster density ratios for either channel, indicating that the signals co-localize to the

Parameter	THG	SHG	Cross-correlation
Fiber straightness	Increase from proximal to transition/ distal, $p = 1*10^{-11}$	Increase from proximal to transition to distal, $p = 4*10^{-6}$	N/A
Fiber length	Increase from proximal/transition to distal, $p = 2*10^{-7}$	Increase from proximal/transition to distal, $p = 2*10^{-12}$	N/A
Ellipticity (ACF)	Increase from proximal to transition/ distal, $p = 5*10^{-5}$	Increase from proximal to distal, $p = 4*10^{-5}$	Increase from proximal to transition/ distal, $p = 0.0002$
Major axis FHWM	Increase from proximal to distal, $p = 0.003$	Increase from proximal to transition/ distal, $p = 6*10^{-6}$	Increase from proximal to distal, $p = 0.0002$
Minor axis FWHM	Positive linear trend in mean, no change in median, $p = 0.24$	Increase from proximal to transition/distal, $p = 3*10^{-6}$	Increase from proximal to transition/distal $p = 0.01$
Fiber Width	Transition significantly less than proximal/ distal, $p = 0.002$	Increase from proximal/transition to distal, $p = 0.0002$	N/A
Offset	Insignificant decrease from proximal to transition/ distal, $p = 0.05$	Decrease from proximal to transition/distal, $p = 0.008$	Decrease from proximal/ transition to distal, $p = 0.006$
Sum of residuals	Insignificant decrease from proximal/transition to distal, $p = 0.62$	Decrease from proximal to transition/distal, $p = 0.02$	No trend $p = 0.46$
Cluster Density	Insignificant decrease from proximal to distal, $p = 0.61$	Increase from proximal to transition/distal, $p = 0.0009$	No trend $p = 0.90$
% Colocalization	Parabolic trend, no post-hoc significance between regions, $p = 0.03$	No trend $p = 0.52$	No trend $p = 0.25$

Table 4.2: Summary of trends and one-way Anova comparison results observed in SHG and THG imaging of sectioned mussel threads for all output parameters produced using CT-FiRE and ICS/ICCS.

same degree in all regions. THG signal was however significantly more likely to overlap with SHG signal than vice versa, consistent with it being generated from non-specifically bound stain rather than omnipresent collagen fibrils.

PCA was then applied to the THG and SHG data using the entire data set with all nine variables. The biplots for these are shown below in Figures 4.7a and 4.7c. Only the first four

principal components (PCs) are necessary to capture at least 85% of the variance in both channels, and the first two alone captured at least 60% (Figures 4.7b and 4.7d) Parallel lines in the biplot indicate that metrics correlate closely and have similar weightings in the PCs; comparing the vectors for the CT-FiRE outputs to those from ICS, it is clear that there is some correlation between the fitted fiber straightness and ACF ellipticity in both channels, and that the ACF offset and residual values are unique in terms of their contribution. The SHG data in particular can be compressed down to one dimension while retaining much of its variance.

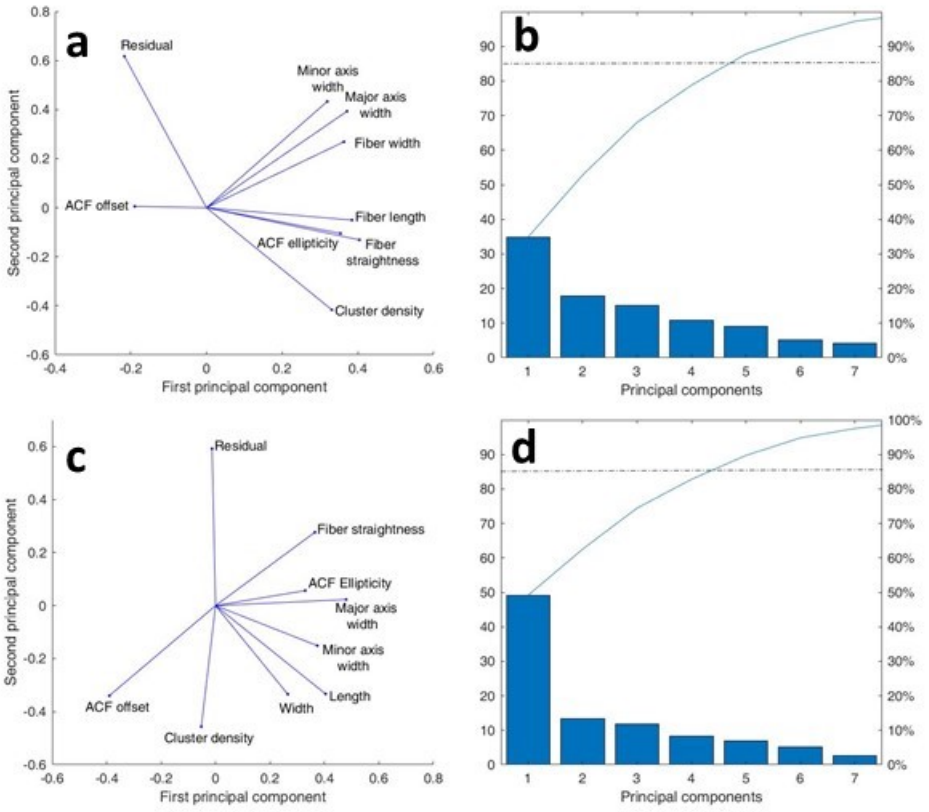

Figure 4.7: 2-axis biplots showing the first two PCs of the entire data set in both channels, with scree plots showing the variance captured by each PC. THG data shown in (a) and (b), SHG data shown in (c) and (d). Solid lines in (c) and (d) indicate the cumulative variance of the PCs; dashed lines indicate the 85% variance threshold.

Plotting the individual data points grouped by region reveals the distribution of the three datasets in principal component space. Figure 4.8 shows this distribution for the

first two . Each plot shows the first two PCs, with successive components describing less variance in the dataset. The thread regions are grouped by colour, and ovals are drawn to indicate the spread of data points with a radius of two standard deviations in each component axis centered on the mean value for that region. The data points from frames belonging to each individual thread are connected to show their movement within their respective regions.

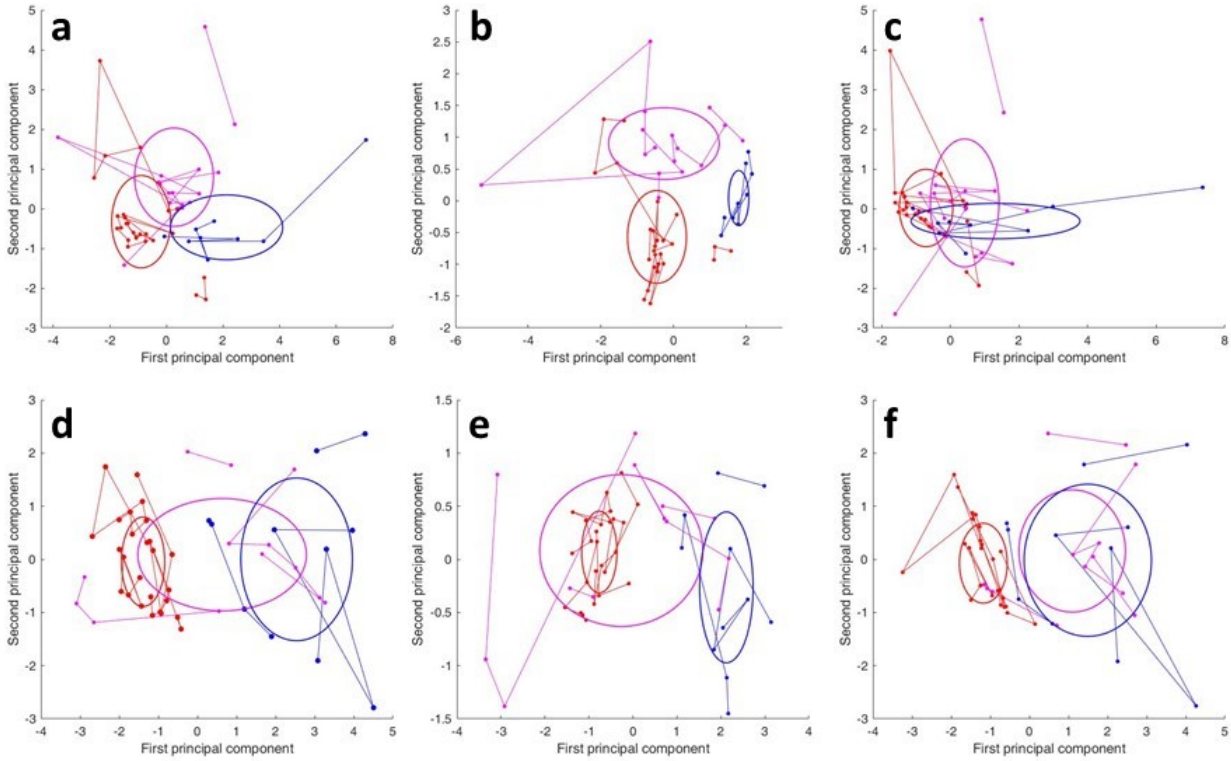

Figure 4.8: Scatter plots of the first two PCs determined with PCA using (a) all measured parameters from CT-FiRE and ICS analysis; (b) CT-FiRE parameters only; (c) ICS parameters only. Each row shows analysis for one channel: THG (a,b,c) and SHG (d,e,f). Data points are grouped by colour according to region: proximal (red), transition (magenta), or distal (blue) regions. Straight lines connect individual points from each fiber. Ovals indicate the 2σ radius from the mean along each principal axis.

In the two most significant components, the proximal points are often clustered together, will the distal points form a less concentrated cluster in a distinctly different region of the plot. The transition region points cross from one terminal region to the other, although

many threads have too few points to show long-distance trends. In subsequent PCs a similar pattern of spreading is observed, although the circles are all centered more closely on the origin (not shown). THG appears to have tighter point distributions, but also more distant outliers. Additionally, the use of only CT-FiRE outputs identifies the transition region as being more proximal, while the ICS outputs group those points more closely with the distal data. The most transitory behaviour is observed for the combination of both, with the most distinct progression from proximal to transition to distal occurring for SHG images of PCA using both ICS and CT-FiRE data.

Figure 4.9 shows the first PC values of all data points in box-and-whisker plots, split by region in box plot. THG (a-c) and SHG (d-f) are compared for the same combinations of input variables used to produce Figure 4.8. Red lines indicate median values, boxes indicate the interquartile range, and whiskers indicate the highest and lowest non-outlier data points. Outliers more than three standard deviations from the median are marked by red crosses. This more clearly shows that the choice of input parameters has a strong influence on the conclusion of the nature of the transition region, although it stretches between the points describing the proximal and distal regions no matter what inputs are used.

4.3.3 CT-FiRE control validation

To verify that the CT-FiRE outputs were fitting actual image features (or structural metrics) rather than random variations, control datasets were produced of the distal and proximal data using the scrambling algorithm and analyzed for statistical significance between the proximal and distal regions. Scrambling regions of 40, 30, 20, 10 and 5 pixels^2 were tested to observe the impact of scrambling scale on the preservation of statistical significance between regions for different features. Figure 4.10 shows, for each channel, the ratio of the experimental p-value for each of the CT-FiRE metrics to the p-value of the metric in unscrambled images. Error bars show the standard deviation of the mean of five randomized datasets.

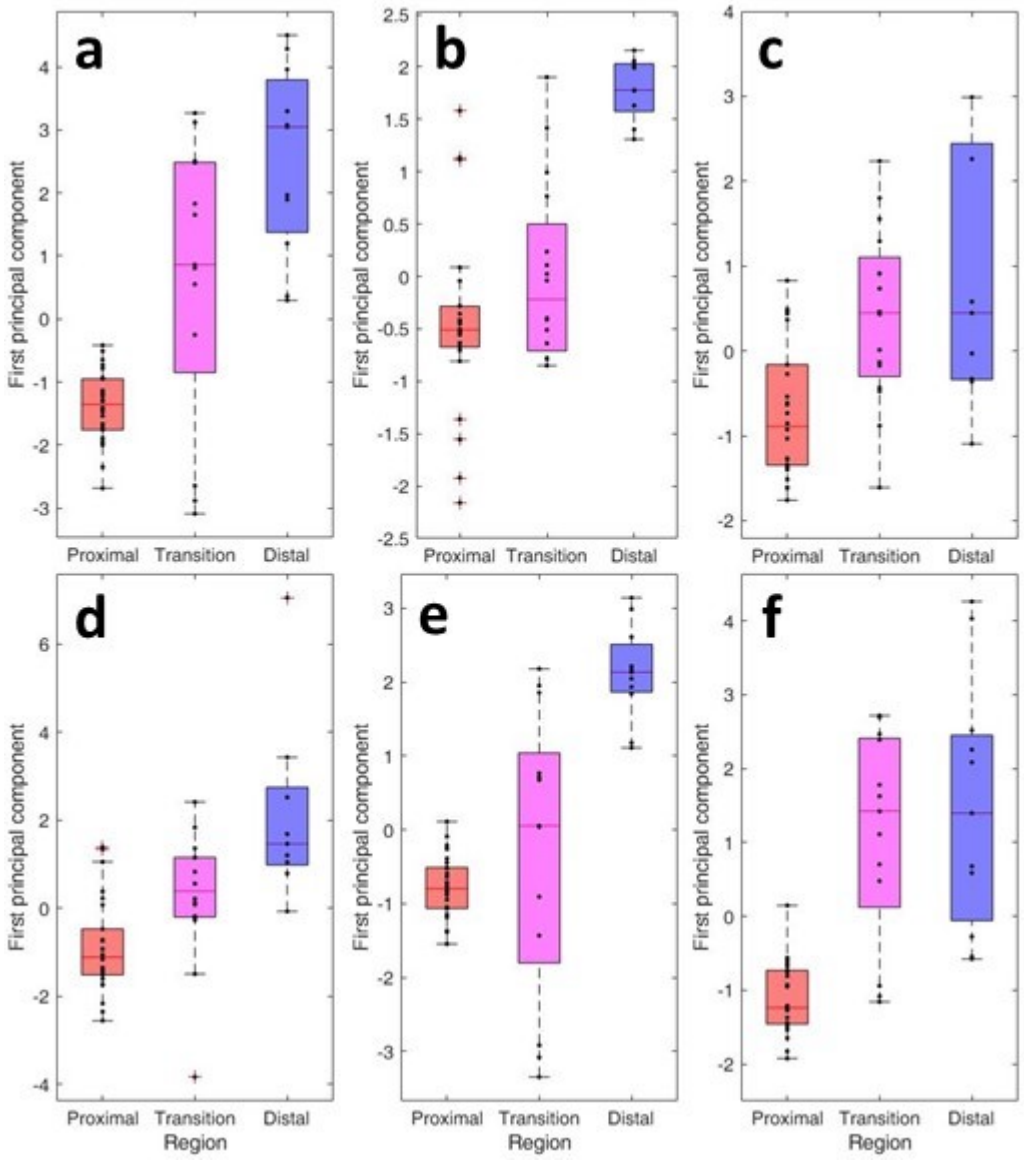

Figure 4.9: Distributions of the first principal component values in the proximal (red), transition (magenta), and distal (blue) regions, for THG images (a,b,c) and SHG images (d,e,f). PCA performed using (a) all measured parameters from CT-FiRE and ICS analysis; (b) CT-FiRE parameters only; (c) ICS parameters only. Boxes indicate the median and 25th/75th percentile windows.

Although the significance does not disappear completely, particularly for straightness, it is reduced drastically at all length scales, confirming that the characteristics of the images are more structural than random.

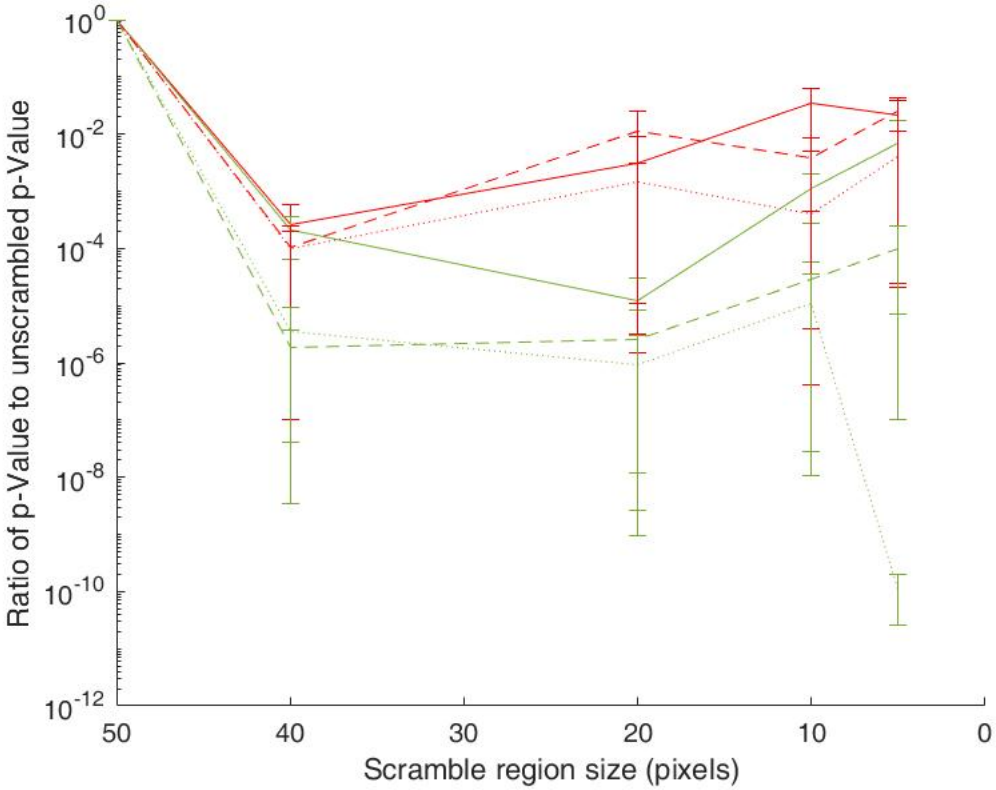

Figure 4.10: Ratio of the p-values for CT-FiRE outputs of scrambled to unscrambled mussel byssus datasets using length scales of 40, 30, 20, 10 and 5 pixels. Red lines show THG data, green lines show SHG data. Solid, dashed and dotted lines correspond to straightness, width and length data, respectively.

4.3.4 Application to TEM images

The processing pipeline was also tested on previously-acquired transmission electron microscopy images of the byssus core. Two images from the proximal and one each from the transition and distal regions were separated into approximately twenty 1 µm squares and analyzed individually. Figure 4.11 shows a cropped section from the full images of these regions, where the fine structure of each is clearly visible. The transition region appears particularly to be a distinct combination of the proximal and distal motifs.

PCA was conducted using all of the ICS output parameters that were incorporated for the NLSM analysis: cluster density, major axis width, minor axis width, and ellipticity

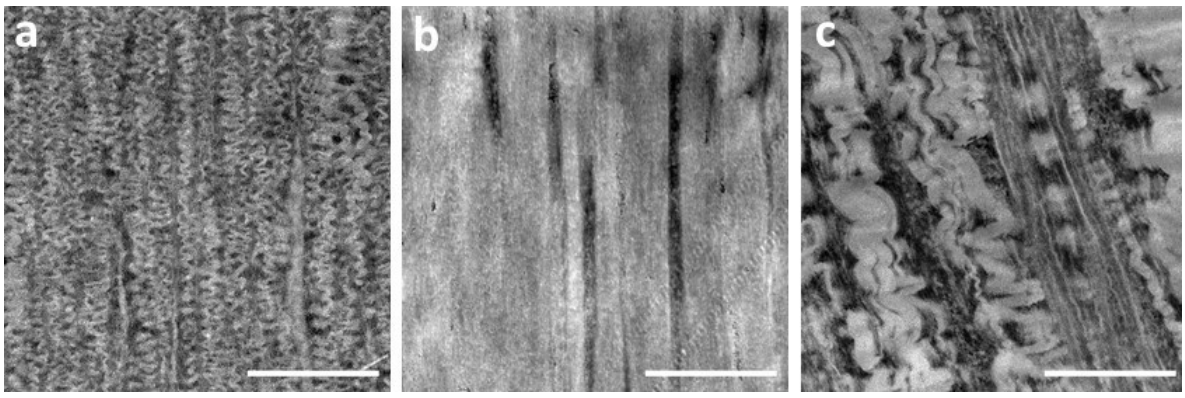

Figure 4.11: Sample regions from TEM images of *M. edulis* byssal threads used for ICS analysis showing the fine structure of the proximal (a), transition (b), and distal (c) regions. Scale bars 1 µm.

(rotation angle, offset and peak location were ignored). The same statistically significant behaviour as in the NLSM images was observed for major axis width ($p << 0.05$) and ellipticity ($p < 0.05$). Cluster density appeared to be much larger in the transition region, with no significant difference between the proximal and distal regions. Minor axis width appeared to increase from the proximal to distal region, but was much higher in the transition region. These p-values are reported approximately, because different images may show very different behaviour, and creating large datasets from single images may bias the Anova results towards significance.

The PCA of all metrics combined consequently shows a similar behaviour to that of the NLSM data in the second PC (23% of total variance) (Figure 4.12(b)). However, in the first PC (55% of total variance), the transition region is distinctly removed from the proximal and distal regions, rather than bridging them (Figure 4.12(b)). The third and fourth principal components are again similar to the NLSM data in that the proximal points more concentrated around the origin and the transition and distal regions are spread over a wider area.

CT-FiRE analysis was performed, but because of the significantly different scales of the two imaging modalities, it was only used to manually measure the width of individual

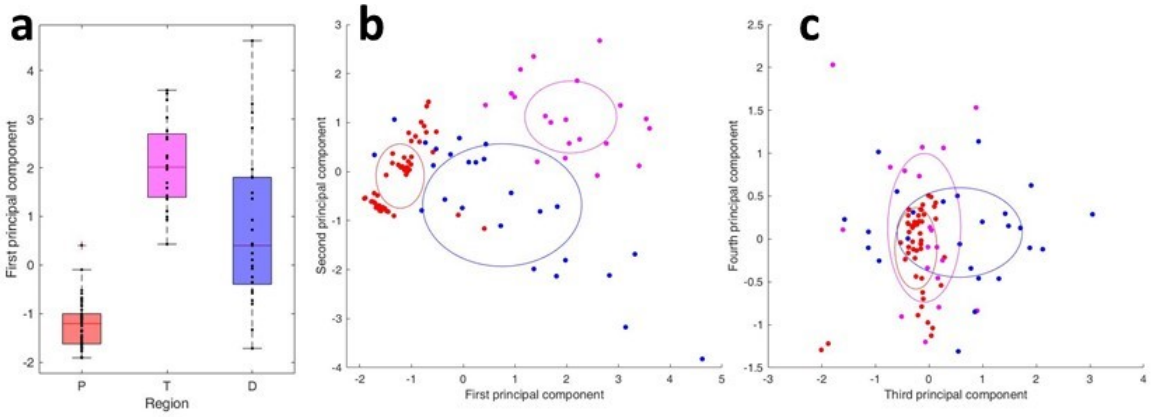

Figure 4.12: Distributions of principal component values in the proximal, transition and distal regions for TEM images, using ICS parameters only. Box-and-whisker plot (a) indicates the median and 25th/75th percentile window for each region; scatter plots show the overall distribution of the first/second and third/fourth PCs. Ovals indicate the 2σ radius from the mean value along each principal axis.

fibers for reference to the widths as determined from NLSM images. These numbers are reported and discussed in Section 5.1.2.

4.4 Observing compacted protein domains in the cuticle of *Mytilus edulis* byssal threads

When imaging whole threads that had been cleared with 3Disco, bright spots larger than the diffraction limit and localized on the outer surface of the threads were clearly visible in the THG channel (see Figure 4.13). However, some spots were very dim in the SHG channel and some had no visible feature at all. To analyze them quantitatively to determine whether they could the densely cross-linked proteinaceous granules observed with CRS [101], smaller ROIs containing between five and twenty of these features were sectioned and processed with the ICS pipeline. This sectioning was done mainly to allow for localized background subtraction, as there was nonuniform structural noise arising

from the thread itself (indicated by the white arrow in Figure 4.13b). This was done by taking the average value of the brightest uniform background present in a given ROI.

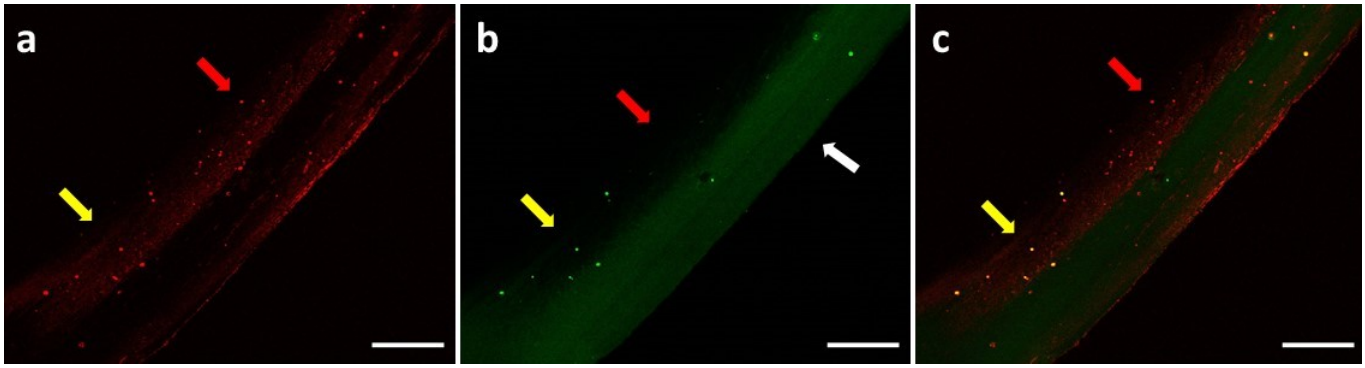

Figure 4.13: Distal region of an optically cleared thread showing sub-micron domains in the cuticle producing (a) THG and (b) SHG. The superposition of the two channels is given in (c). The contrast in has been enhanced in (b) only to 0.05% saturation for visibility. Red arrows indicate granules only visible in the THG channel; yellow arrows indicate granules visible in both channels. White arrow indicates structural background noise in the SHG channel. Scale bars 50 µm.

Figure 4.14 shows the size and ellipticity data for the granules imaged using autocorrelation of THG and SHG. It shows that the majority of the measured domains are within the established range of the granule sizes for *M. edulis* (500 - 1000 nm) regardless of imaging modality. However, the uncertainty is much larger on the SHG measurements, likely due to the higher structural background arising from the byssus core.

Since there was both uniform white noise and localized structural noise, SNR was measured by taking the ratio of the mean intensity of domains traced in the THG channel to the standard deviation of a similar sized spot adjacent to the domain. Measurements were taken in the SHG channel using the same size region, even when the feature in that channel was smaller or not visible at all. There was significance variation between domains, with the mean SNR being slightly higher in the THG channel compared to the SHG channel (17 ± 8 vs 13 ± 11, n = 31).

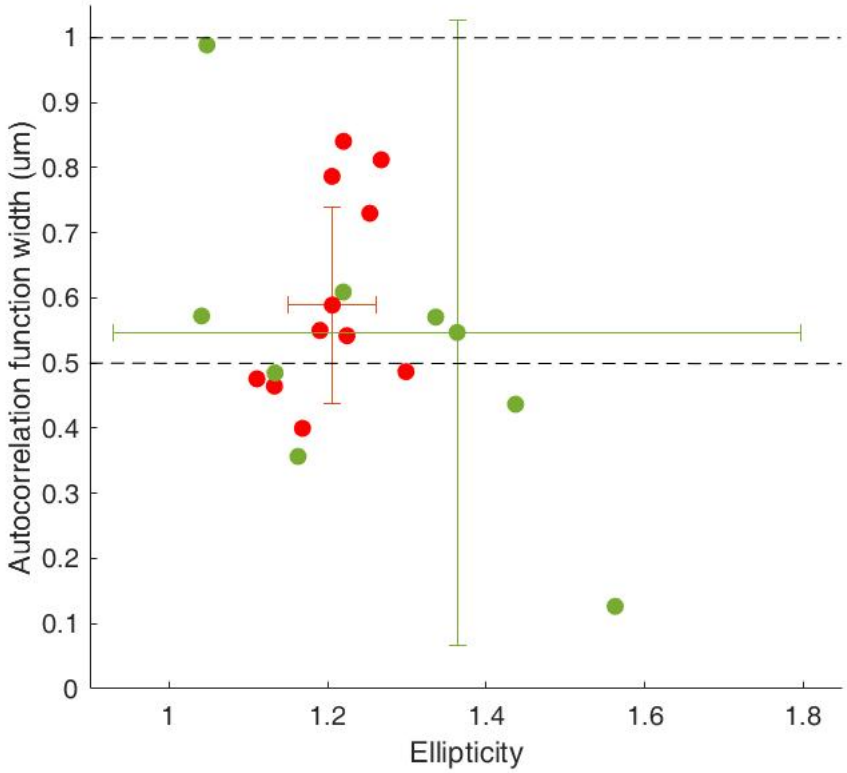

Figure 4.14: Scatter plot of size vs. ellipticity of domains imaged in the cuticle of *M. edulis* measured using THG (red) and SHG (green). Points with error bars indicate the respective means and standard deviations. Dashed lines indicate the typical size range of these granules as determined by electron microscopy. Some far outlying SHG points influencing the large error bars are omitted.

4.5 Measuring progression of myelination in *Xenopus laevis* optic tectum and hindbrain

Myelination progression was evaluated by capturing images of two retinotectal regions of *X. laevis* tadpoles, the hindbrain and the optic chiasm, at stages 51, 52, and 53 of their development. These had been previously identified empirically as capturing the onset of myelin compaction, which was observed again in images captured here. CT-FiRE and spatial ICS and ICCS were applied to assess quantitative changes between the stages in

both channels. An additional pre-processing method to remove image artifacts based on nonlinear scattering theory was also quantified and found to be ineffective.

4.5.1 Imaging the compacted myelin using THG myelin

The presence of THG signal from myelinated axons at stage 53, and its absence at stage 51, was confirmed by imaging samples stained for axons, MBP, and nuclei. Myelinated axons in stage 53 were clearly visible in the three-photon detection channel. However, DAPI (a nuclear stain) also showed strong 3PF signal (highlighting cell bodies) and IgG Alexa-647 produced a non-zero amount of 2PF. Therefore images were captured using samples only stained for MBP for quantitative analysis. Since there was no staining to increase the SNR of the THG signal, it was expected that there would be other sources of contrast in the image. Features resembling cell nuclei were observed, as well some bright features too thick or amorphous to be axons. To minimize these signals, all images were captured twice, once using linear polarization oriented at a 45 degree angle to the principal axes of the fiber morphologies, and a second time using circular polarization. Since THG driven by the step-change in refractive index between the myelin sheath and the ECM should be suppressed in the latter case, this should provide a control image dominated by birefringence-based THG and 3PF. This showed qualitative improvements, appropriate for non-quantitative assessment. It was later assessed post hoc by examining its impact on key quantitative outputs from CT-FiRE and ICCS and found to be ineffective, and possibly detrimental (see Section 4.5.3).

All 2-channel images were split into two single channel images and pre-processed with the CANDLE filter plugin in ImageJ [198]. The THg channel was processed further by subtracting the image captured using circular polarization from the identical image captured using linear polarization; this was then recombined with the SHG image. Figures 4.15 and 4.16 show sets of three images depicting the progression of myelination in the optic chiasm and hindbrain, respectively. All images have had contrast increased with ImageJ to 0.3% saturation in each channel for visual clarity. Beginning at stage 51, fibers

can be seen clearly to be present above a background signal in the two-photon channel. This background signal is possibly from unbound fluorescent antibodies or uncompacted myelin protrusions, and fades as the 2PF signal becomes more concentrated and brighter in stages 52 and 53. On the other hand, no fibers are visible at all in the THG channel in stage 51, beginning to form in stage 52 and becoming clearly defined in stage 53. Three-photon artifacts and background also fade as stages progress due to the relatively brighter axonal THG signal.

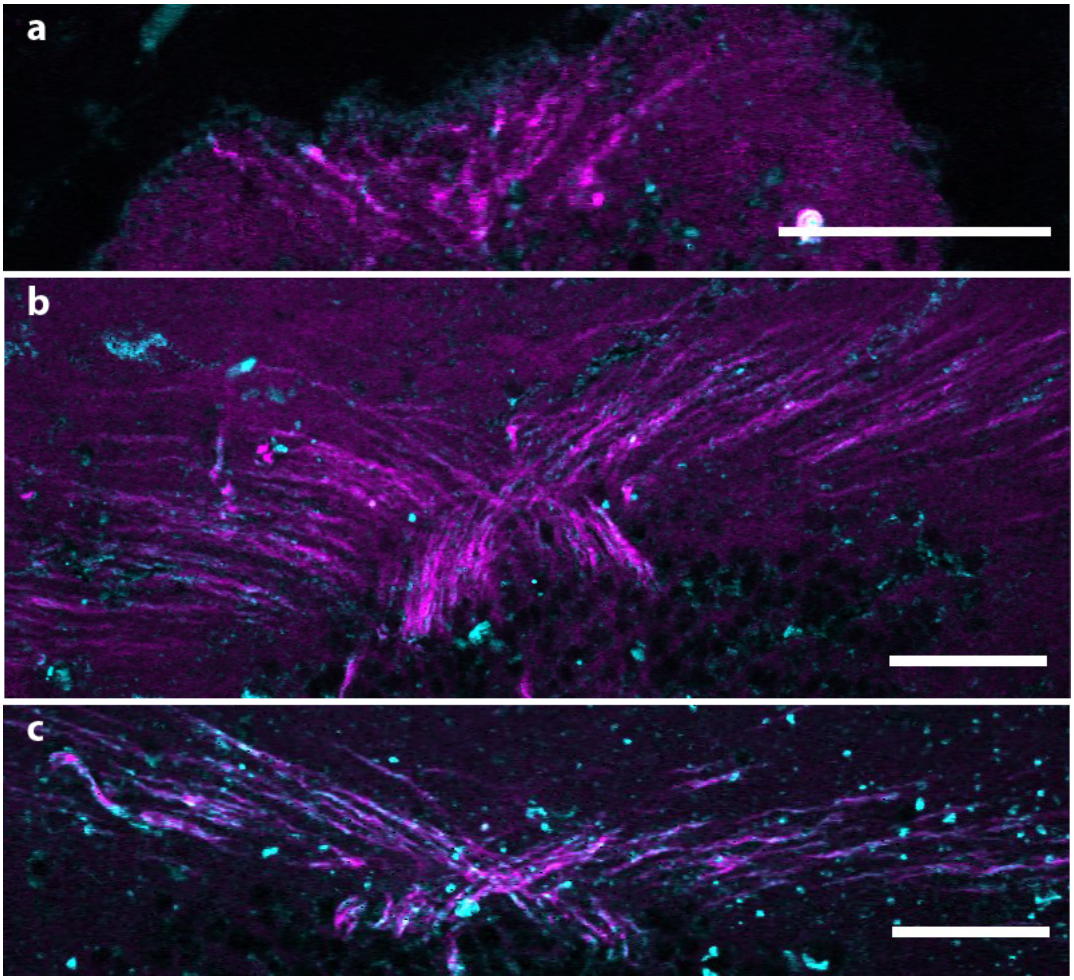

Figure 4.15: Sample images of *X. laevis* optic chiasm sections at stage 51 (a), stage 52 (b), and stage 53 (c) of its development. Images have been processed with CANDLE filtering (both channels) and circular polarization subtraction (THG channel). Three-photon signal appears in blue, two-photon signal appears in magenta. Scale bars 50 μm.

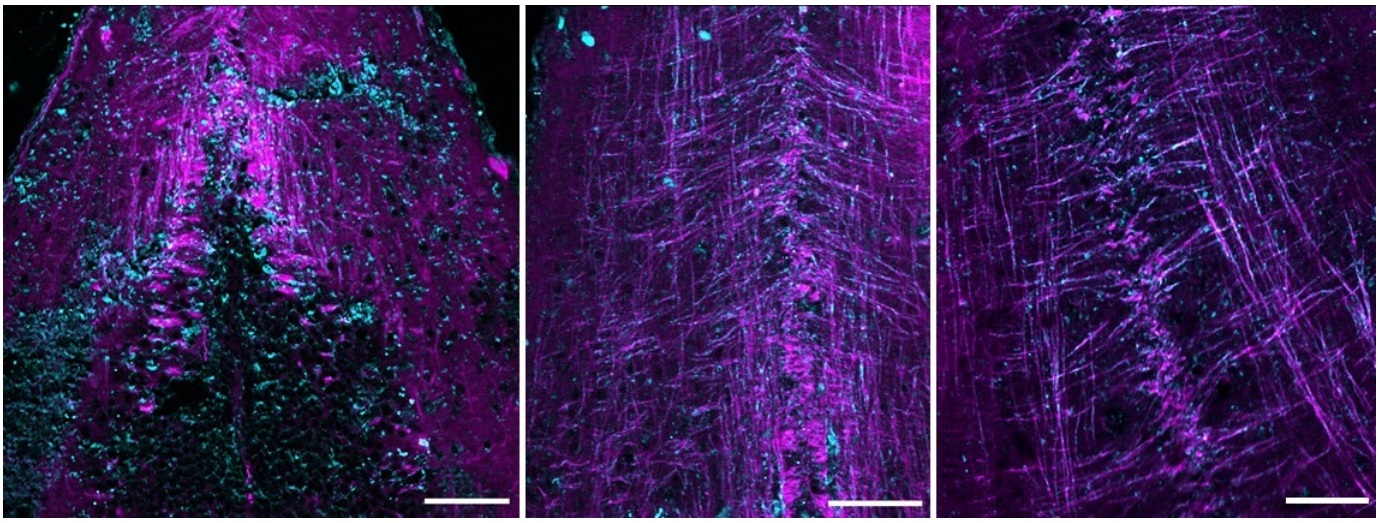

Figure 4.16: Sample images of *X. laevis* hindbrain sections at stage 51 (a), stage 52 (b), and stage 53 (c) of its development. Images have been processed with CANDLE filtering (both channels) and circular polarization subtraction (THG channel). Three-photon signal appears in blue, two-photon signal appears in magenta. Scale bars 50 µm.

SNR values of the final images were measured by tracing matching threads in each image (30 total threads per region) and taking the ratio of the average pixel value over the standard deviation along the trace. SNR values fell between 3 and 7, with some high outliers, and were consistent across all three regions, although the highest values were all measured in the stage 53 images.

4.5.2 Quantification of the progression of myelination

One advantage of cross-correlative methods in multimodal microscopy is that they minimize contribution from background signal, non-target features, and other sources that are only present in one or the other channel. With this in mind, cross-correlation was chosen as the primary mode of analysis, with fiber fitting applied to a set of equivalent monochromatic images (see Section 3.4.2). The environment around the hindbrain is known to be more complex than the optic chiasm, and to vary more between samples (clearly visible in Figure 4.16), so the quantitative analysis presented here is focused on the latter. Significance was calculated simultaneously across all three stages.

All three fiber fitting metrics showed an increase across the stages, although straightness was not statistically significant. Correlation analysis was less consistent, but did show significance indicative of progression in three metrics: ellipticity, offset and the goodness of the Gaussian fit as measured by the sum of the residuals. The major and minor axis widths both showed slight increasing trends, but were heavily influenced by outliers, particularly at stage 51. ICS outputs relating to the amplitude of the ACF (cluster and colocalization densities) showed highly significant, negative parabolic behaviour, which is not consistent with biological intuition regarding the myelination system, and is not included here.

The erratic nature of the results may indicate that some of the variation is a result of differences between samples rather than progression of myelination. Since there in no published research, to the best of our knowledge, on the application of ICCS to non-periodic, non-diffraction limited features, autocorrelation of the SHG and THG signals was performed to verify whether the same significant variation was present in autocorrelated data. This revealed that certain metrics were consistently significant under both analyses, while others become more or less significant in one or the other. Figure 4.17 shows the trends from stage 51 to stage 53 of each of the parameters that maintained consistently small p-values and similar trending behaviour for both.

Despite the large uncertainty, the convergence is significant for the fiber width, offset and goodness of fit. However, fiber length is significant in diverging instead.

4.3 summarizes the observations of each trend for all of the observables that showed significance in either analysis, indicating between which stages the most change occurred. Measured thread widths and lengths for comparison, as well as the p-values for both cross-correlation and differential comparison.

In general the observations are logically consistent with the expectation that fibers imaged with THG would thicken and segments would connect as the axons are progressively covered in compact myelin. The fiber dimensions as measured by ICCS are significantly different than CT-FiRE, which is to be expected given the sensitivity of image correlation to structural characteristics of the image, and the long-range curvature of the optic nerves.

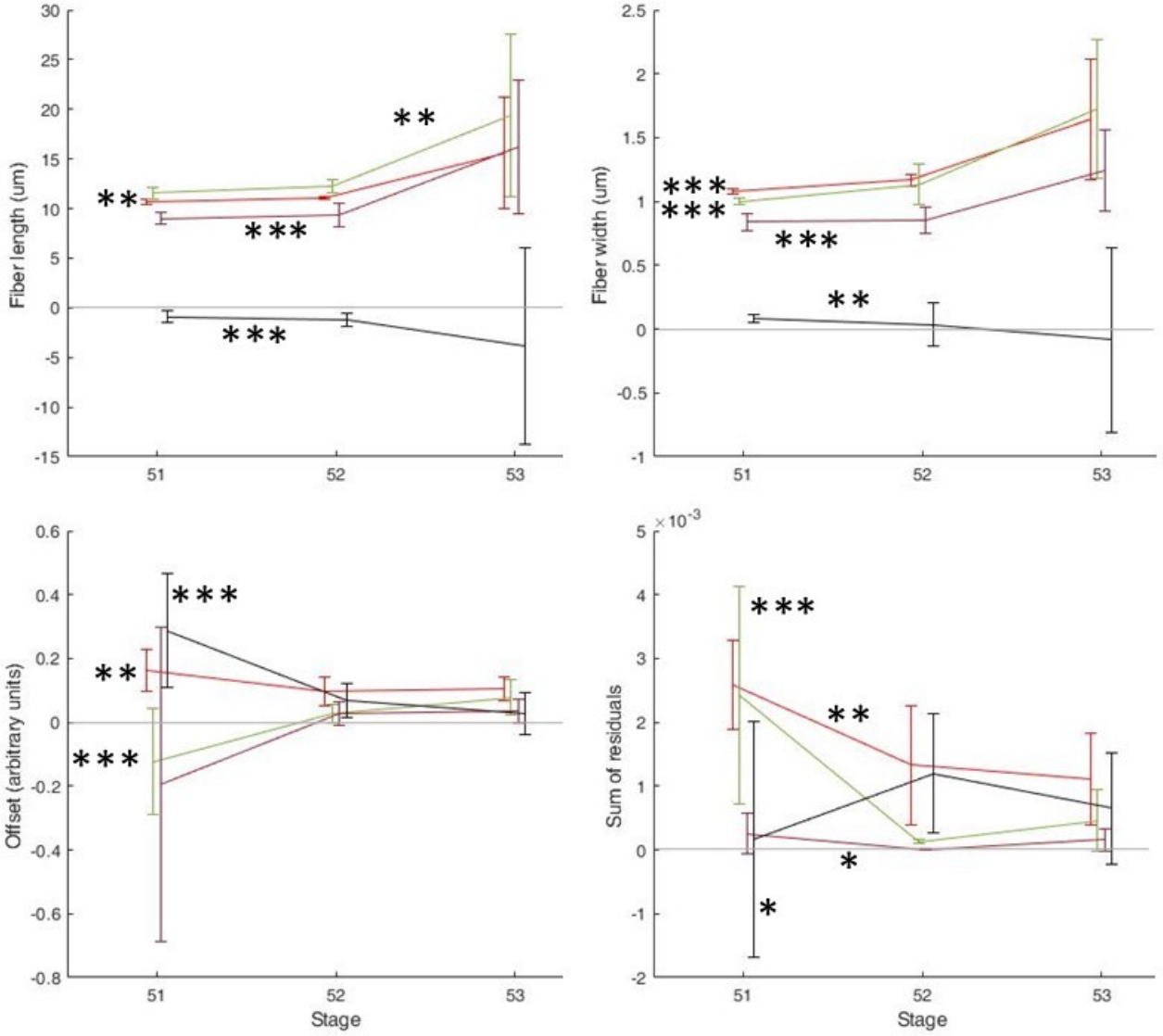

Figure 4.17: Line plots of selected CT-FiRE and ICCS output metrics showing the change (or lack thereof) from stage 51 to stage 53 in the THG (red) and SHG (green) images of the *X. laevis* optic chiasm. The difference between the two is plotted in black. The ICCS/monochromatic image analyses are plotted in dark red. Error bars indicate the standard deviation of the mean at at each time point; differential error bars are the sum of the THG and SHG error in quadrature. Asterisks next to the lines indicate the significance of the respective p-values; * ≤ 0.05; ** ≤ 0.005; *** ≤ 0.0005.

Simple quantitative assessment of the hindbrain indicated, as expected, that the analysis was heavily impacted by sample variation. No metrics showed more significance in ICCS

Parameter	Observations	p-Value (cross-correlation)	p-Value (convergence)
Fiber width	Increase from stage 52 to stage 53 (0.8 ± 0.2 µm to 1.2 ± 0.3 µm)	$5*10^{-5}$	0.002
Fiber length	Increase from stage 52 to stage 53 (9 ± 3 µm to 16 ± 2 µm)	$4*10^{-4}$	$0\ 2*10^{-3}$
Fiber straightness	Increase from stage 51 to stage 53	0.5	0.007
Ellipticity	Increase from stage 51 to stage 52	$9*10^{-3}$	0.0005*
Minor axis width	Increase from stage 52 to stage 53 (2 ± 2 µm to 3 ± 2 µm)	0.30	$3*10^{-4}$
Major axis width	Increase from stage 52 to stage 53 (4 ± 4 µm to 6 ± 4 µm)	0.61	$4*10^{-4}$
Offset	Increase from stage 51 to stage 52	0.08	$4*10^{-5}$
Sum of residuals	Decrease from stage 51 to stage 52	0.014	0.0392

*The difference between THG and SHG showed a parabolic rather than a linear trend

Table 4.3: Summary of trends and one-way Anova comparison results in selected ICCS and CT-FiRE outputs from optic chiasm images of *X. laevis* tadpoles.

than they did in the respective autocorrelation functions. Rather, ICCS for many outputs showed little to no statistical significance. However, there was an indication that the ACF widths, ellipticities, and goodness of fit might converge. Figure 4.18 shows the progression of these four metrics for autocorrelation of the SHG and THG data compared to the ICCS and convergence analyses in the hindbrain, where the convergence clearly shows statistical significance while even loses the significance arising from sample variations.

4.5.3 Validation of THG polarization filtering

Figure 4.19 shows a set of images contrasting the linear (4.19a) and circular (4.19b) polarization versions of an image, along with the differential image they produce (4.19c). These images are taken from the stage 52 hindbrain samples. The polarization filtering was primarily performed to improve image quality for publication when quantification was not required.

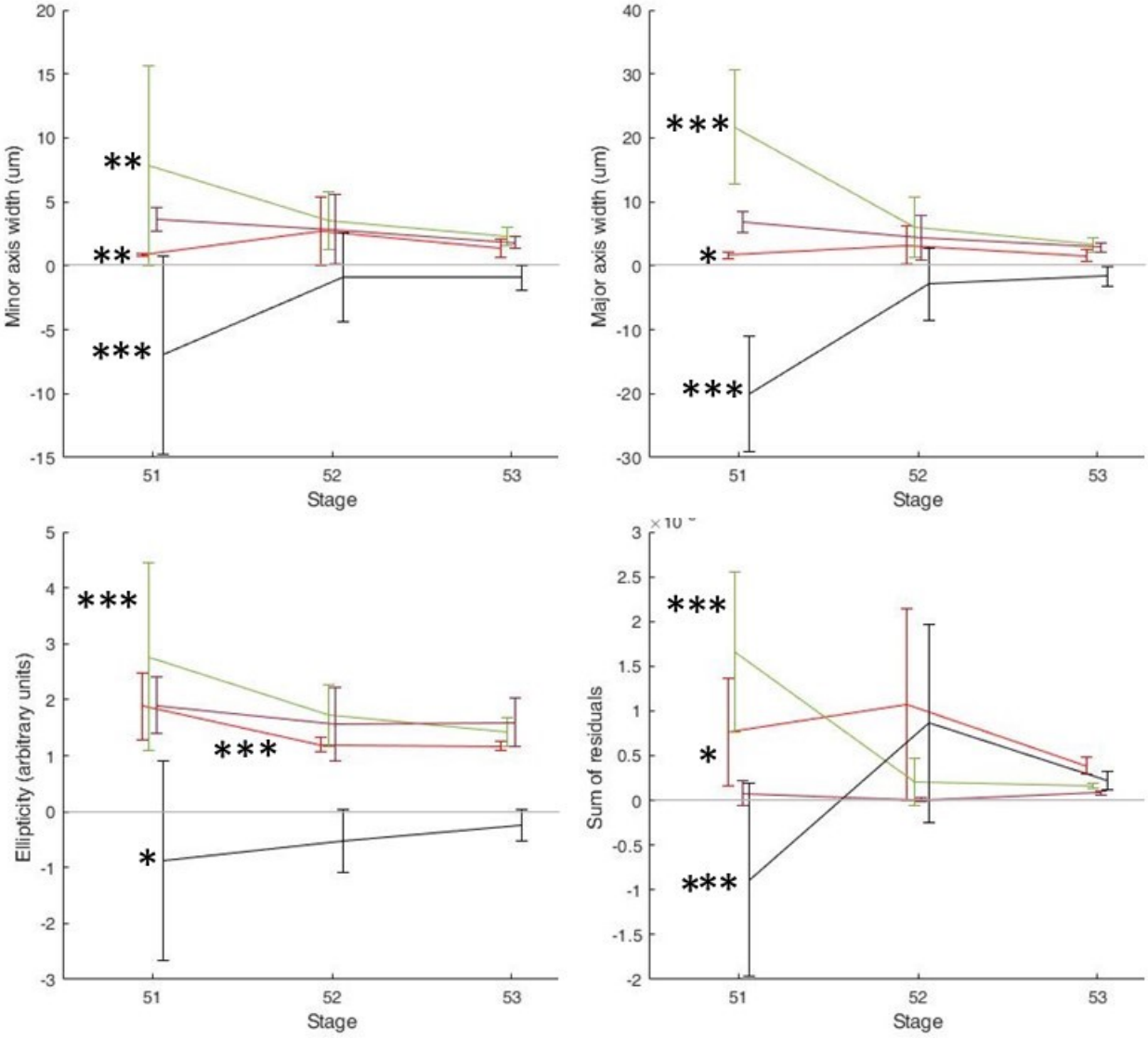

Figure 4.18: Line plots of selected CT-FiRE and ICCS output metrics showing the change (or lack thereof) from stage 51 to stage 53 in the THG (red) and SHG (green) images of the *X. laevis* hindbrain. The difference between the two is plotted in black. The ICCS/monochromatic image analyses are plotted in dark red. Error bars indicate the standard deviation of the mean at at each time point; differential error bars are the sum of the THG and SHG error in quadrature. Asterisks next to the lines indicate the significance of the respective p-values; * ≤ 0.05; ** ≤ 0.005; *** ≤ 0.0005.

There is a clear distinction in the contrast between the images collected using linear and circular excitation polarization, and the differential image of the two. The higher back-

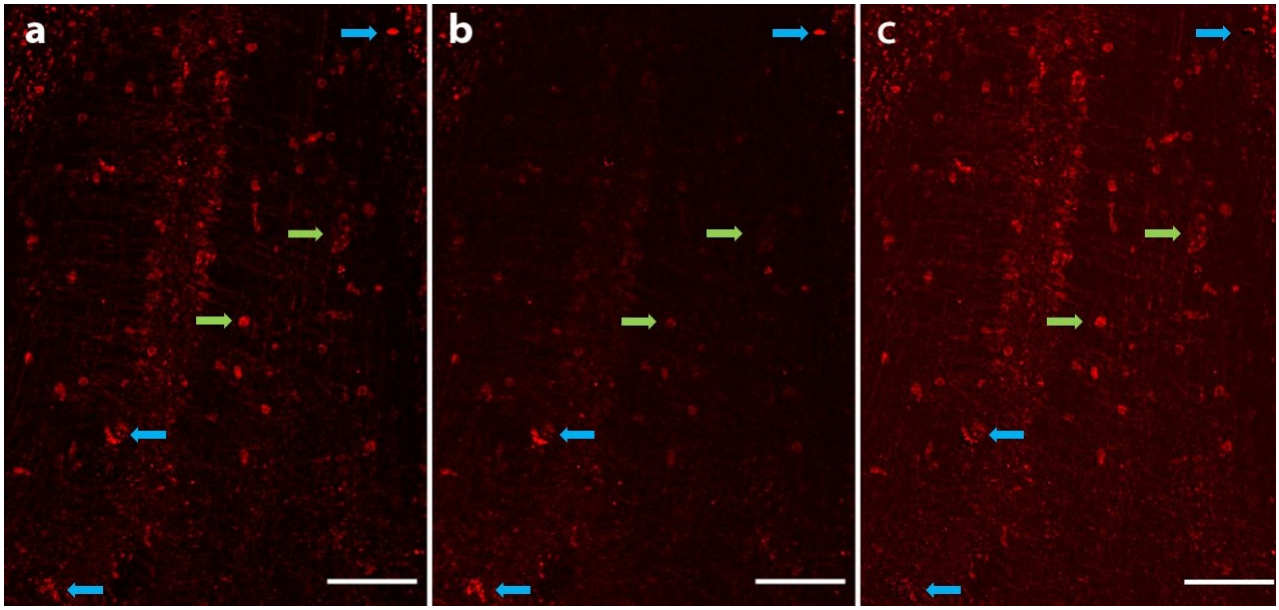

Figure 4.19: Three-photon images of a sectioned stage 52 *X. laevis* hindbrain sample, collected with linear (a) and circular (b) polarization, and the differential image a - b (c). All images have had contrast enhanced to 0.3% pixel saturation. Blue arrows indicate non-fiber features filtered out in the differential image. Green arrows indicate non-fiber features observed to become more prominent. Scale bars 50 µm.

ground in the differential image is a result of the lack of overly bright features dominating the contrast enhancement. Certain bright non-fiber features in the linear image stand out strongly in the circular image, and are dimmer in the differential image (blue arrows). However, some other non-fiber features appear to become more prominent (green arrows).

To assess quantitatively whether it was appropriate for this purpose, the linear polarization and circular polarization-filtered images of the stage 53 chiasm samples were compared for changes in their SNR, and the effective SNR of the most predictive ICS/ICCS outputs (measured as the mean value divided by the standard deviation). CT-FiRE outputs were also assessed since they were able to qualitatively trace threads, despite not providing statistical significance. These results are reported in Table 4.4.

In most cases, the output SNR fell after filtering. In nearly all cases, subtracting the circularly polarized signal did not change the reported value significantly, but the fact that the effective SNR of the measurements that appear to be the most useful in quantifying

Parameter	THG		Cross-correlation	
	linear	isolated	linear	isolated
Fiber straightness	466	686*	140	173*
Fiber width	48	41*	62	77
Fiber length	207	90*	22	25*
ACF width	1.4	1.5*	2.5	2.2
ACF ellipticity	7	6*	30	15
SNR	4.4 ± 1.6	N/A	3.5 ± 1.5	N/A

* $<$ 5% change from linear mean

Table 4.4: Effective SNR values of cross-correlation and fiber fitting output metrics and mean image SNR, before and after pre-processing by subtracting THG image produced using circularly polarized excitation light from THG image produced using linearly polarized excitation light.

myelination was reduced suggests that this is not a viable approach to improve optic tectum images for quantitative analysis. Similar comparison in the hindbrain yielded more consistent improvement, but not enough to make quantitative analysis of those images possible.

Chapter 5

Discussion of results, conclusions, and future work

The aims of this work are twofold: first to apply nonlinear harmonic generation imaging to biological and biomaterals systems were it has not been used before, and second to investigate these systems using two different analysis paradigms: image correlation spectroscopy and algorithmic feature registration. This chapter will review the results of the analyses from Chapter 4, put them in context with comparable imaging modalities and analytical techniques, and provide direction for the next steps in the implementation of these conclusions. The conclusions reached here are limited to the data collected prior to analysis; at the time of writing, the NLSM system used to acquire these images was awaiting repair, so no further experiments were possible.

For *Mytilus edulis*, and sea mussels in general, there have been no previous reports in the literature of harmonic generation imaging of their byssal threads, and no quantitative microscopy of their structure has been performed, much less a mesoscale comparison between the proximal and distal zones. There is more literature exploring the cuticle, but none offering the multipurpose flexibility of HGM; cuticle imaging in this work is primarily a proof of concept. Application of CT-FiRE and ICS are entirely novel approaches to both of these systems.

For myelination and the compaction of myelin, both THG as a method [94,137] and myelination in *Xenopus laevis* [125,135] as a subject have been explored, but the two nonlinear methods have not been combined. Additionally, quantitative analysis has been limited to manual and semi-automatic feature measurement, limiting its applicability to either very small scale or very large scale measurements. CT-FiRE and ICS/ICCS, with the large number of outputs they provide, present novel tools to explore new questions of the process of myelination in a network of axons.

5.1 Quantification of mussel byssal thread core with ICS and fiber fitting

The transition region of the mussel byssus is ambiguously defined, only in that at some point the proximal region of the thread becomes the distal region of the thread. The relevant question, from a bio-inspired materials standpoint, is how the two regions interact in a way that optimizes the mechanical properties of the thread. The first step to doing so is to establish consistent metrics that distinguish one from the other.

5.1.1 Evaluation of the applicability of CT-FiRE and ICS

Previous work on the application of image correlation spectroscopy to collagen fibers has concluded that all of the parameters of the ACF (excluding the peak location and the rotation angle) correlate in some way with the properties of either the fibers or their spatial and angular distribution. The ACF width has been further extended to the macroscopic mechanical properties of the fibers [119,120,204]. However, practical implementation of ICS is almost always performed on relatively straight collagen fibers with either uniformly ordered or uniformly disordered morphologies (both simulated and *ex vivo*). Byssal threads are somewhere in the middle, having a general direction of orientation but also being wavy in the proximal region and displaying a significant amount of crosslinking. Notably,

Mir et al. did explore the impact of the randomness of the orientation of the fibers, and found that the ACF was more elliptical in more ordered samples [120]; Hall et al. also demonstrated that increasingly disordered fiber morphologies introduced distortions into the autocorrelation surface, making it harder to fit with a 2D Gaussian [119].

The implications of these are important, because the waviness and crosslinking of collagen are the two principal differences between the proximal and distal regions. Translating the analysis to collagen-like byssal cores is additionally complicated by the fact that autocorrelation of collagen is generally applied to distinguish diseased or damaged collagen from a baseline. That can be accomplished by establishing a minimum number of parameters that are consistent in healthy tissue, and classifying a certain deviation as 'other'. In the case of byssal fibers, to understand the transition region the parameters need to show a consistent, but statistically distinct behaviour in two separate regions. This motivated the use of CT-FiRE as a highly developed source of additional variance between regions.

Casting the net for variance as wide as possible, thread sections were stained with a harmonophore collagen stain, PsR, so that the byssus core could be imaged using both SHG and THG. An increase in SNR from the high scattering cross section of PsR should increase the SNR of the images, improving the quantitative measurements; indeed this was observed in the proximal end, where less organized collagen fibers result in a shorter coherence length for SHG. THG is also less dependent on the polarization of the laser, improving the contrast from more randomly oriented domains, and is less prone to backscattering than SHG [77, 170]. Finally, it frees up the two photon channel for other modalities in future explorations. Previous studies have only applied to SHG signal; autocorrelation has only been applied to THG previously in time domain FCS [205].

With this in mind, imaging was performed simultaneously in both channels, and all outputs from both analytical techniques were examined for significance (summarized in Table 4.2). Interestingly, the most statistical significance was achieved when imaging with SHG, despite the lower signal to noise ratio and generally lower contrast. In the THG im-

ages, neither fiber width fitted by CT-FiRE nor the minor axis width of the autocorrelation function were effective at distinguishing the proximal and distal regions; in SHG both did, although they gave conflicting conclusions about the structure of the transition zone. The offset and sum of residuals also showed slight trends as expected, moreso in the SHG channel, but with minimal statistical significance compared to the other metrics.

This behaviour may simply be consistent with the coherent nature of harmonic generation. SHG depends on the organization of collagen, whereas THG from PsR simply detects its presence. Adjacent bundles of fibers would then be detected as single large fibers by THG, whereas SHG emanating from them may interfere destructively. This would degrade the distinction of fiber widths if the proximal region is comprised mostly of smaller bundles, which aggregate in an ordered fashion in the distal region. This also affects the forward/backward scattering ratio, reducing the SNR in smaller fibers [206]. This would also be reflected in the goodness of fit of the correlation function, which is worse for highly disordered regions; THG would see a more uniform signal from closely packed threads that were in fact disordered relative to each other [120].

From the analysis of individual variables, there is no clear consensus as to whether the transition region is structurally more similar to the proximal or distal region, or a distinct combination of the two. This motivated the use of PCA to try to establish distinct low-dimensional morphospaces for each region, using the many available input metrics. As a general result (see Figure 4.8), images from the disordered proximal region are very similar to each other, while the distal points occupy a distinctly different region and are spread over a much larger area. Tracing the threads and looking only at the first PC does give a strong argument that the transition region is in fact a gradual mixing of the two regions, but without multiple images of full, unsectioned threads this remains a speculative interpretation.

To streamline future research, one important question is whether autocorrelation can be considered to be as effective as CT-FiRE at mapping structural differences in collagen-like fiber systems, as opposed to applying both together, and whether SHG or THG is

the preferable imaging modality. Regarding the first, the distinct modes of analysis do not correlate with each other (Figures 4.7a and 4.7c); comparing PCA with the CT-FiRE outputs classifies the transition region with the proximal one, while PCA based on ICS groups it more closely with the distal region. Fiber fitting also produced more consistent results across images in the distal region; in the proximal region ICS was marginally better. Complete separation between proximal and distal data was only achieved for SHG imaging using both analyses. Given the complexity of performing both analyses in parallel, it may be appropriate to choose one or the other, knowing in advance the bias of the conclusions. The analysis could also be chosen based on the desire to see more or less variance in a particular region, if for example an experiment was being performed on the distal section of threads grown under different conditions.

The variation between channels is more likely due to SHG being more sensitive to the organization of collagen. This would then imply that the decision of which modality to use depends again on the experimental conditions. Comparing the p-values as presented in Table 4.2, SHG is a better choice when looking for changes in the effective width and length of fiber bundles, while THG is better for measuring straightness through with CT-FiRE, and equivalent if measuring it with ICS. Given that under extension threads both straighten [107] and unfold their flanking domains [105], this may still be a matter of preference and/or convenience.

5.1.2 Comparison of NLSM images to TEM images

Applying the two modes of analysis to images taken in a different modality at a very different length scale presents another way to assess whether they are appropriate for the byssal thread system. There is no history of CT-FiRE being applied to nanometer-resolution images, and it was unclear what it would identify as a thread. In total, six independent measurements of thread width were made in this work: both spatial autocorrelation and CT-FiRE fiber fitting for each of the two µm-scale HGM imaging channels and nm-scale

Method	Proximal (μm)	Transition (μm)	Distal (μm)
THG autocorrelation	1.8 ± 1.1	2.1 ± 1.0	2.3 ± 1.9
THG fiber fitting	1.6 ± 0.2	1.5 ± 0.2	1.74 ± 0.08
SHG autocorrelation	0.21 ± 0.14	1 ± 1.5	1.2 ± 0.9
SHG fiber fitting	1.2 ± 0.1	1.3 ± 0.3	1.6 ± 0.2
TEM autocorrelation	0.0041 ± 0.0039	0.051 ± 0.016	0.02 ± 0.01
TEM fiber fitting	0.010 ± 0.002	0.016 ± 0.004	0.015 ± 0.004
Manual fiber measurement	0.04 ± 0.01	0.12 ± 0.07	0.28 ± 0.12

Table 5.1: Comparison of thread widths as measured by autocorrelation, CT-FiRE fiber fitting, and manual tracing of NLSM and TEM images.

TEM images. These measurements are given in Table 5.1, along with average thread widths as measured manually from TEM images using ImageJ.

The most obvious difference is in the thousandfold gap between widths as measured by NLSM and TEM. Referring to the images in Figure 4.11, in particular Figure 4.11b, the reason for this is quite obvious. The width of fibers, which are in fact bundles composed of many fibrils, will vary depending on whether resolution is at the scale of individual fibrils or of bundled fibers. This is true both for feature registration and autocorrelation. Measuring manually, the question of what constituted a fiber was often arbitrary decision, as there were distinct features across a range of widths that could rightly be labeled as individual fibers. It is particularly evident here that SHG is measuring a changing fiber size, while the THG fiber size is consistent across all regions.

There is no literature measuring fibril sizes specific to the mussel byssus, but the TEM results are consistent with previous measurements of fibrils of mammalian collagens [207]. Autocorrelation is not expected to return the exact fiber widths, but the widths as measured by both TEM and SHG autocorrelation follow approximately the same linear increase as the manual fiber measurements. The small datasets (particularly for the TEM images) and

large uncertainties suggest that autocorrelation of TEM and SHG images may further be a useful, high throughput indicator of the width of the aggregated collagen fibers. The most obvious analysis to corroborate this would be to measure the forward/backward scattering ratio and compare it to these results to those of Williams et al. [75] and Légaré et al. [208].

5.2 Exploratory imaging of granules in the mussel byssus cuticle

The role of the granules in the mechanical behaviour of the cuticle has been a focus of considerable research because of the significance of polymeric thin films in materials and bio-inspired materials science. This is complicated by several factors, such as lack of appropriate fluorescent labels and the fact that the mechanical behaviour of the thread is strongly affected by whether it is wet or dry (problematic for microscopy requiring intensive sample preparation). An ideal imaging modality would therefore be label-free and involve minimal technical intervention. So far only resonance-based CRS has been used to image intact samples, a time-intensive method relying on metal-protein complexes specifically localized within the granules [121]. Although this elucidates the functional difference between the granules and the surrounding matrix and makes it possible to map their distribution, it is limited in its ability to probe mechanical changes unless they are accompanied (or driven) by molecular ones. Andersen et al. have demonstrated through electron microscopy and atomic force microscopy that these domains deform under strain, and have postulated the ways in which this affects the stress/strain behaviour of the cuticle (and therefore the thread) [109], but these methods are unable to image in real time or across large areas. Harmonic generation is both relatively straightforward to implement and is able to image intact 3D samples mounted in water, their natural *in situ* environment.

Based on the domain widths measured with autocorrelation in the THG channel, it is likely that the features are cuticle granules. Further, the autocorrelation metrics of these

features have the same relationships in both the SHG and THG signals, and the THG signal forms a solid feature rather than a ring at the granule-matrix interface. This establishes that the features generate harmonic signal because they display ordered birefringence, as expected from a granule with a high degree of cross-linking. The SNR in images acquired with THG was effectively the same as for SHG, but the uncertainty measurements is much larger due to the dependence of SHG on the polarization of the laser relative to the scattering feature.

One important observation in some whole threads, specifically ones that had been stained with picrosirius red, was of domains that were visible only in the SHG channel. These had a size similar to the other features measured by autocorrelation, but displayed a very different correlation function amplitude and no THG signal. Principal component analysis of datasets containing these features behaved erratically depending on background subtraction, suggesting that they were quantitatively very different than the THG domains. The source of these features is unclear, but their observation reinforces the case for proceeding specifically with THG imaging.

Two immediate applications are well-served by HGM combined with ICS. First, the fact that birefringence is dependent on the presence of cross-links suggests that it may be used to measure the extent of that crosslinking, without the steady background in Raman spectroscopy images observed by Harrington et al. [121]. This gives a better approach with which to quantify the influence of external conditions on the formation of the cuticle between the molecular and the macroscopic level, and consequently the mechanical properties of the byssus. The gap may possibly be bridged completely by using ICS to measure the eccentricity of granules across an image series which, with HGM, can be captured in real time during a stress-strain test. Andersen et al. have proposed mechanical models based on certain deformation behaviour of the granules under stress, but they have not been tested to the necessary degree [109]. Beyond that, the question of whether this behaviour is uniform along the whole thread is a question that appears to not have been asked in the literature thus far; here the simple sample preparation and

large field of view of harmonic generation give it a further advantage over other forms of microscopy.

5.3 Quantitative imaging of myelination during *Xenopus laevis* development

Label-free imaging methods for studying myelination are particularly valuable for their ability to distinguish compacted from uncompacted myelin, an important quality when researching the dynamic nature of myelination in the nervous system. The demonstration of quantitative THG imaging applied to *Xenopus laevis* tadpoles is motivated by the advantages that technical simplicity, µm-scale model neural systems, and potential new analytical pathways have for the future of research into the process of myelination,

5.3.1 Demonstration of quantifiable, simultaneous THG and 2PF imaging of unmyelinated vs fully myelinated axons

Of the label-free techniques that have been demonstrated, third harmonic generation is easily the least technically complex, requiring no more than a single high-power NIR laser and a scanning confocal microscope equipped with a high-NA multiphoton objective. However, it has been applied primarily to fully-grown mouse models, where nervous tissues are already immensely complex, and huge relative to the size of individual neurons. Even large scale imaging like that accomplished by Redlich et al. [209] only captures a tiny µm-scale region of a mm-scale organ. An ideal system for exploring this fundamental aspect of nervous system during its development would be small and well understood; to this end only stimulated Raman spectroscopy has been demonstrated on the µm-scale *X. laevis* model system [135].

The first step to establishing THG as a viable method for imaging in *X. laevis* is simply to demonstrate that its small-diameter axons are large enough (after the compaction of myelin)

to generate THG images at a practical resolution. As expected from previous electron microscopy measurements, properly myelinated fibers in the optic nerve and hindbrain are clearly visible using THG microscopy. Qualitatively, these signals are colocalized with fluorescent signal from myelin basic protein, and emerge across the tadpole development periods during which most compaction of myelin is expected to occur.

Regarding quantitative measurements, there was a strong desire to demonstrate a novel alternative to the established techniques using colocalization matrices and coefficients [194] or signal density [209]. These approaches to measuring density and colocalization in nervous systems look at an aggregate scale and obscure any more subtle pattern information, while approaches for measuring the characteristics of individual nerve fibers focus on individual features and miss the forest for the trees. More fully automated methods with more nuanced output parameters are an opportunity to improve both throughput and the richness of information that can be extracted from images.

In practice, however, both CT-FiRE and ICCS struggled to demonstrate differences between unmyelinated and fully myelinated axons. The only parameters that showed significant change between the time points that could reasonably be attributed to structural change, rather than variation between the samples, were the correlation function offset, the goodness of fit, and the fitted fiber width. Other parameters that showed significance under ICCS behaved erratically when verifying whether the correlative characteristics of the THG and SHG images appeared to converge as well. ICCS was expected to have difficulty in measuring structural features through the ACF and CCF widths, because the curved morphology of fibers in the optic chiasm does not change with time. It performed better than expected, although it is unclear whether that was a result of sample variation and merits further investigation.

That the offset decreases as myelination progresses speculatively indicates that it is measuring an increase in the feature density of the image consistent with increasing THG signal. In the hindbrain, the convergence of the THG and SHG ACF widths suggests that autocorrelation alone may be sufficient to quantify the thickening of fibers in regions

dominated by straight morphologies even if they are oriented perpendicular to each other. This thickening is more clearly observed in the optic chiasm by CT-FiRE, and the widths measured by fiber fitting agreed with those measured previously in developing and mature *X. laevis*, considering that the nerve structures in the tadpoles are likely to be slightly smaller than in adults [125]. The observed increase in fitted fiber length was expected in the THG and cross-correlation images, although the parallel observation in the SHG autocorrelation data casts doubt on what exactly was being measured. It is also worth noting that despite the lack of significance of CCF width in the chiasm, the mean values did trend in the right direction with a similar magnitude.

It is also possible that both CT-FiRE and ICCS are appropriate methods, and they simply quantify not only the refractive index boundary of compacted myelin but also the general coalescence of the myelin signal as compaction brings it closer together. This approach would require validation with either simulation of explicit morphologies different than those of collagen, or simple and well-established biological models of myelination, or both. If it turns out to work for both modalities and can be replicated *in vivo* with transparent tadpoles, it clears the way for research into the intricate process of nervous system development in relation to external stimuli.

The largest factor that may be distorting these quantitative results is the application of the CANDLE non-local means filter. As a carefully engineered method of noise removal, it may have removed some of the localized fluctuations that would have distinguished the behaviour of the emergent THG signal from that of the already-present fluorescent myelin. It could also have connected and padded under-myelinated fibers, affecting the CT-FiRE measurements.

Since real-time imaging of a single sample in which myelination occurs on an appropriate timescale (as opposed to the days/weeks between *X. laevis* is of great interest, testing the analyses on this sort of data may be another useful test for validity. This would eliminate the varying background signal and test strictly for structural change over time; it may

also be possible to extract more information, such as the rate at myelination/compaction expands from an initial point, by analyzing temporal behaviour.

5.3.2 Polarization-dependent signal filtering nonlinear scattering images of heterogeneous highly scattering tissues

The immediate observation that section *X. laevis* neural tissue contained many features that showed THG contrast makes it clear that coherent scattering has less feature specificity than SRS. Based on nonlinear optical theory, a straightforward method of removing these features was tested using circular polarization. This was done on spec, since THG imaging is generally performed with circular polarization to even out the THG produced by all fiber orientations. However, the increased signal from non-fiber features may be more problematic in very heterogeneous samples; addressing this by exploiting the physics of nonlinear scattering has not been explored previously in the literature.

Assessing the manipulation in terms of the most useful CT-FiRE and autocorrelation outputs, it provided no benefit and potentially reduces signal to noise ratio when used in the optic chiasm. When applied to the hindbrain, it performed better, improving signal to noise ratios particularly in the underdeveloped structures at stage 51 and 52. These results should be taken with a grain of salt, since the manipulated images were still not useful for quantitative analysis.

It is possible that for images containing many scattering features other than those of interest, there is some benefit to be gained from filtering based on polarization. The method would benefit from better refinement based on a more rigorous understanding of the nonlinear theory, and would likely require a detailed understanding of the sample being imaged beyond the features of interest. However, it is ultimately better to select regions for analysis that show minimal nonlinear scattering without additional manipulation.

5.4 Summary of Key Conclusions

In sum, the unorthodox pairing of multimodal NLSM and correlation analysis generally shows promise for quantitative imaging of highly scattering biological tissues. It is able to distinguish features larger than the diffraction limit when the behaviour of its outputs are understood correctly. When applied alongside established feature fitting algorithms, it provides a large set of outputs that can be used to reach quantitative conclusions about collagen-like structures in natural biomaterials, and provide quantitative measurements of high-contrast granular features. CT-FiRE can also be applied with consistent results, extending it beyond its typical context of mammalian collagens. ICS and CT-FiRE may have some applicability to other fibrillar structures as well, such as systems of neurons, but in a much more limited way that prompts additional research into their use in exotic fibrillar structures.

The usage of both NSLM and these analytical techniques depends heavily on the exact question being asked, so clear experimental design is particularly important. Future work in each area will be specific to the system in question, but can be undertaken with some expectation of useful results.

Bibliography

[1] W. L. Peticolas, "Applications of raman spectroscopy to biological macromolecules," *Biochimie*, vol. 57, no. 4, pp. 417–428, 1975.

[2] J. C. Elliott and S. D. Dover, "X-ray microtomography," *Journal of Microscopy*, vol. 126, no. 2, pp. 211–213, 1982.

[3] J. C. Kendrew, G. Bodo, H. M. Dintzis, R. G. Parrish, and H. Wyckoff, "A three-dimensional model of the myoglobin molecule obtained by x-ray analysis," *Nature*, vol. 181, p. 662, 1958.

[4] A. M. Baró, R. Miranda, J. Alamán, N. García, G. Binnig, H. Rohrer, C. Gerber, and J. L. Carrascosa, "Determination of surface topography of biological specimens at high resolution by scanning tunnelling microscopy," *Nature*, vol. 315, no. 6016, pp. 253–254, 1985.

[5] A. Bogner, P. H. Jouneau, G. Thollet, D. Basset, and C. Gauthier, "A history of scanning electron microscopy developments: towards "wet-stem" imaging," *Micron*, vol. 38, no. 4, pp. 390–401, 2007.

[6] S. A. Goss and W. D. O. Jr., "Direct ultrasonic velocity measurements of mammalian collagen threads," *The Journal of the Acoustical Society of America*, vol. 65, no. 2, pp. 507–511, 1979.

[7] R. Sharma, M. Singh, and R. Sharma, "Recent advances in sted and resolft super-resolution imaging techniques," *Spectrochimica Acta Part A: Molecular and Biomolecular Spectroscopy*, vol. 231, p. 117715, 2020.

[8] P. Davidovits and M. D. Egger, "Scanning laser microscope," *Nature*, vol. 223, no. 5208, pp. 831–831, 1969.

[9] F. A. Merchant and K. R. Castleman, *Chapter 27 - Computer-Assisted Microscopy*, pp. 777–831. Boston: Academic Press, 2009.

[10] G. Huszka and M. A. M. Gijs, "Super-resolution optical imaging: A comparison," *Micro and Nano Engineering*, vol. 2, pp. 7–28, 2019.

[11] U. Endesfelder and M. Heilemann, "Direct stochastic optical reconstruction microscopy (dstorm)," *Nature Protocols*, no. 1940-6029 (Electronic), 2011.

[12] T. Nakane, A. Kotecha, A. Sente, G. McMullan, S. Masiulis, P. M. G. E. Brown, I. T. Grigoras, L. Malinauskaite, T. Malinauskas, J. Miehling, T. Uchański, L. Yu, D. Karia, E. V. Pechnikova, E. de Jong, J. Keizer, M. Bischoff, J. McCormack, P. Tiemeijer, S. W. Hardwick, D. Y. Chirgadze, G. Murshudov, A. R. Aricescu, and S. H. W. Scheres, "Single-particle cryo-em at atomic resolution," *Nature*, vol. 587, no. 7832, pp. 152–156, 2020.

[13] C. Reyes-Aldasoro, *Bright Field Microscopy*, pp. 215–289. John Wiley & Sons, 2015.

[14] H. A. Alturkistani, F. M. Tashkandi, and Z. M. Mohammedsaleh, "Histological stains: A literature review and case study," *Global journal of health science*, vol. 8, no. 3, pp. 72–79, 2015.

[15] J. A. Ramos-Vara, "Technical aspects of immunohistochemistry," *Veterinary Pathology*, vol. 42, no. 4, pp. 405–426, 2005.

[16] R. Lattouf, R. Younes, D. Lutomski, N. Naaman, G. Godeau, K. Senni, and S. Changotade, "Picrosirius red staining: a useful tool to appraise collagen networks in normal and pathological tissues," *J Histochem Cytochem*, vol. 62, no. 10, pp. 751–8, 2014.

[17] P. J. Tadrous, "A method of psf generation for 3d brightfield deconvolution," *Journal of Microscopy*, vol. 237, no. 2, pp. 192–199, 2010.

[18] C. N. Hernández Candia and B. Gutiérrez-Medina, "Direct imaging of phase objects enables conventional deconvolution in bright field light microscopy," *PLOS ONE*, vol. 9, no. 2, p. e89106, 2014.

[19] J.-Y. Liu, W.-H. Fan, K.-L. Han, W.-Q. Deng, D.-L. Xu, and N.-Q. Lou, "Ultrafast vibrational and thermal relaxation of dye molecules in solutions," *The Journal of Physical Chemistry A*, vol. 107, no. 50, pp. 10857–10861, 2003.

[20] G. Weber, *Rotational Brownian Motion and Polarization of the Fluorescence of Solutions*, vol. 8, pp. 415–459. Academic Press, 1953.

[21] G. Hamilton and H. Sanabria, *Chapter 6 - Multiparameter fluorescence spectroscopy of single molecules*, pp. 269–333. Elsevier, 2019.

[22] B. K. Nunnally, H. He, L.-C. Li, S. A. Tucker, and L. B. McGown, "Characterization of visible dyes for four-decay fluorescence detection in dna sequencing," *Analytical Chemistry*, vol. 69, no. 13, pp. 2392–2397, 1997.

[23] M. W. Conklin, P. P. Provenzano, K. W. Eliceiri, R. Sullivan, and P. J. Keely, "Fluorescence lifetime imaging of endogenous fluorophores in histopathology sections reveals differences between normal and tumor epithelium in carcinoma in situ of the breast," *Cell Biochemistry and Biophysics*, vol. 53, no. 3, pp. 145–157, 2009.

[24] M. Y. Berezin and S. Achilefu, "Fluorescence lifetime measurements and biological imaging," *Chemical reviews*, vol. 110, no. 5, pp. 2641–2684, 2010.

[25] E. N. Harvey and A. M. Chase, "The phosphorescence microscope," *Review of Scientific Instruments*, vol. 13, no. 8, pp. 365–368, 1942.

[26] A. H. Coons, H. J. Creech, R. N. Jones, and E. Berliner, "The demonstration of pneumococcal antigen in tissues by the use of fluorescent antibody," *The Journal of Immunology*, vol. 45, no. 3, pp. 159–170, 1942.

[27] M. Chalfie, Y. Tu, G. Euskirchen, W. W. Ward, and D. C. Prasher, "Green fluorescent protein as a marker for gene expression," *Science*, vol. 263, no. 5148, pp. 802–5, 1994.

[28] T. Dertinger, R. Colyer, G. Iyer, S. Weiss, and J. Enderlein, "Fast, background-free, 3d super-resolution optical fluctuation imaging (sofi)," *Proceedings of the National Academy of Sciences*, vol. 106, no. 52, pp. 22287–22292, 2009.

[29] S. van de Linde, A. Löschberger, T. Klein, M. Heidbreder, S. Wolter, M. Heilemann, and M. Sauer, "Direct stochastic optical reconstruction microscopy with standard fluorescent probes," *Nature Protocols*, vol. 6, no. 7, pp. 991–1009, 2011.

[30] D. Axelrod, "Cell-substrate contacts illuminated by total internal reflection fluorescence," *The Journal of cell biology*, vol. 89, no. 1, pp. 141–145, 1981.

[31] A. H. VOIE, D. H. BURNS, and F. A. SPELMAN, "Orthogonal-plane fluorescence optical sectioning: Three-dimensional imaging of macroscopic biological specimens," *Journal of Microscopy*, vol. 170, no. 3, pp. 229–236, 1993.

[32] E. G. Reynaud, J. Peychl, J. Huisken, and P. Tomancak, "Guide to light-sheet microscopy for adventurous biologists," *Nature Methods*, vol. 12, no. 1, pp. 30–34, 2015.

[33] M. Born and E. Wolf, *Principles of Optics: Electromagnetic Theory of Propagation, Interference and Diffraction of Light*. Cambridge: Cambridge University Press, 7 ed., 1999.

[34] G. J. Brakenhoff, P. Blom, and P. Barends, "Confocal scanning light microscopy with high aperture immersion lenses," *Journal of Microscopy*, vol. 117, no. 2, pp. 219–232, 1979.

[35] T. Bernas, M. Zarebski, R. R. Cook, and J. W. Dobrucki, "Minimizing photobleaching during confocal microscopy of fluorescent probes bound to chromatin: role of anoxia and photon flux," *Journal of Microscopy*, vol. 215, no. 3, pp. 281–296, 2004.

[36] A. P. Demchenko, "Photobleaching of organic fluorophores: quantitative characterization, mechanisms, protection," *Methods Appl Fluoresc*, vol. 8, no. 2, p. 022001, 2020.

[37] B. C. Wilson, M. S. Patterson, S. T. Flock, and J. D. Moulton, *The Optical Absorption and Scattering Properties of Tissues in the Visible and Near-Infrared Wavelength Range*, pp. 45–52. Boston, MA: Springer US, 1988.

[38] W. F. Cheong, S. A. Prahl, and A. J. Welch, "A review of the optical properties of biological tissues," *IEEE Journal of Quantum Electronics*, vol. 26, no. 12, pp. 2166–2185, 1990.

[39] E. A. Genina, A. N. Bashkatov, and V. V. Tuchin, "Tissue optical immersion clearing," *Expert Review of Medical Devices*, vol. 7, no. 6, pp. 825–842, 2010.

[40] W. Denk, J. Strickler, and W. Webb, "Two-photon laser scanning fluorescence microscopy," *Science*, vol. 248 4951, pp. 73–6, 1990.

[41] D. W. Piston, "Imaging living cells and tissues by two-photon excitation microscopy," *Trends in Cell Biology*, vol. 9, no. 2, pp. 66–69, 1999.

[42] G. Katona, G. Szalay, P. Maák, A. Kaszás, M. Veress, D. Hillier, B. Chiovini, E. S. Vizi, B. Roska, and B. Rózsa, "Fast two-photon in vivo imaging with three-dimensional random-access scanning in large tissue volumes," *Nature Methods*, vol. 9, no. 2, pp. 201–208, 2012.

[43] C. Tischbirek, A. Birkner, H. Jia, B. Sakmann, and A. Konnerth, "Deep two-photon brain imaging with a red-shifted fluorometric ca¡sup¿2+¡/sup¿ indicator," *Proceedings of the National Academy of Sciences*, vol. 112, no. 36, pp. 11377–11382, 2015.

[44] A. Diaspro and M. Robello, "Two-photon excitation of fluorescence for three-dimensional optical imaging of biological structures," *Journal of Photochemistry and Photobiology B: Biology*, vol. 55, no. 1, pp. 1–8, 2000.

[45] I. Gryczynski, H. Malak, and J. R. Lakowicz, "Multiphoton excitation of the dna stains dapi and hoechst," *Bioimaging*, vol. 4, no. 3, pp. 138–148, 1996.

[46] S. Huang, A. A. Heikal, and W. W. Webb, "Two-photon fluorescence spectroscopy and microscopy of nad(p)h and flavoprotein," *Biophysical Journal*, vol. 82, no. 5, pp. 2811–2825, 2002.

[47] S. Hell, K. Bahlmann, M. Schrader, A. Soini, H. Malak, I. Gryczynski, and J. Lakowicz, "Three-photon excitation in fluorescence microscopy," *Journal of Biomedical Optics*, vol. 1, no. 1, 1996.

[48] S. Maiti, J. B. Shear, R. M. Williams, W. R. Zipfel, and W. W. Webb, "Measuring serotonin distribution in live cells with three-photon excitation," *Science*, vol. 275, no. 5299, pp. 530–532, 1997.

[49] T. Wang, D. G. Ouzounov, C. Wu, N. G. Horton, B. Zhang, C.-H. Wu, Y. Zhang, M. J. Schnitzer, and C. Xu, "Three-photon imaging of mouse brain structure and function through the intact skull," *Nature methods*, vol. 15, no. 10, pp. 789–792, 2018.

[50] I. Gryczynski, H. Malak, J. R. Lakowicz, H. C. Cheung, J. Robinson, and P. K. Umeda, "Fluorescence spectral properties of troponin c mutant f22w with one-, two-, and three-photon excitation," *Biophysical Journal*, vol. 71, no. 6, pp. 3448–3453, 1996.

[51] M. Albota, D. Beljonne, J.-L. Brédas, J. E. Ehrlich, J.-Y. Fu, A. A. Heikal, S. E. Hess, T. Kogej, M. D. Levin, S. R. Marder, D. McCord-Maughon, J. W. Perry, H. Röckel,

M. Rumi, G. Subramaniam, W. W. Webb, X.-L. Wu, and C. Xu, "Design of organic molecules with large two-photon absorption cross sections," *Science*, vol. 281, no. 5383, pp. 1653–1656, 1998.

[52] H. Zhang, J. Liu, L. Wang, M. Sun, X. Yan, J. Wang, J.-P. Guo, and W. Guo, "Amino-si-rhodamines: A new class of two-photon fluorescent dyes with intrinsic targeting ability for lysosomes," *Biomaterials*, vol. 158, pp. 10–22, 2018.

[53] A. G. Condie, S. L. Gerson, R. H. Miller, and Y. Wang, "Two-photon fluorescent imaging of myelination in the spinal cord," *ChemMedChem*, vol. 7, no. 12, pp. 2194–203, 2012.

[54] N. J. Durr, T. Larson, D. K. Smith, B. A. Korgel, K. Sokolov, and A. Ben-Yakar, "Two-photon luminescence imaging of cancer cells using molecularly targeted gold nanorods," *Nano Letters*, vol. 7, no. 4, pp. 941–945, 2007.

[55] Y. Dong, H. Xiao, L. Xing, C. Wu, J. Zhou, Z. Zhou, Y. Liu, S. Zhuo, and P. Li, "Two-photon fluorescence visualization of lysosomal ph changes during mitophagy and cell apoptosis," *Talanta*, vol. 209, p. 120549, 2020.

[56] A. Gasecka, T.-J. Han, C. Favard, B. R. Cho, and S. Brasselet, "Quantitative imaging of molecular order in lipid membranes using two-photon fluorescence polarimetry," *Biophysical Journal*, vol. 97, no. 10, pp. 2854–2862, 2009.

[57] I. Gryczynski, G. Piszczek, Z. Gryczynski, and J. R. Lakowicz, "Four-photon excitation of 2,2'-dimethyl-p-terphenyl," *The journal of physical chemistry. A*, vol. 106, no. 5, pp. 754–759, 2002.

[58] L.-C. Cheng, N. G. Horton, K. Wang, S.-J. Chen, and C. Xu, "Measurements of multiphoton action cross sections for multiphoton microscopy," *Biomedical optics express*, vol. 5, no. 10, pp. 3427–3433, 2014.

[59] B. Wang, Q. Zhan, Y. Zhao, R. Wu, J. Liu, and S. He, "Visible-to-visible four-photon ultrahigh resolution microscopic imaging with 730-nm diode laser excited nanocrystals," *Optics Express*, vol. 24, no. 2, pp. A302–A311, 2016.

[60] M. Ingaramo, A. G. York, E. J. Andrade, K. Rainey, and G. H. Patterson, "Two-photon-like microscopy with orders-of-magnitude lower illumination intensity via two-step fluorescence," *Nature Communications*, vol. 6, no. 1, p. 8184, 2015.

[61] W. Chen, S. Bhaumik, S. A. Veldhuis, G. Xing, Q. Xu, M. Grätzel, S. Mhaisalkar, N. Mathews, and T. C. Sum, "Giant five-photon absorption from multidimensional core-shell halide perovskite colloidal nanocrystals," *Nature Communications*, vol. 8, no. 1, p. 15198, 2017.

[62] I. Freund and M. Deutsch, "Second-harmonic microscopy of biological tissue," *Optics Letters*, vol. 11, no. 2, pp. 94–96, 1986.

[63] R. W. Boyd, *Nonlinear Optics, Third Edition*. Academic Press, Inc., 2008.

[64] M. Müller, J. Squier, K. R. Wilson, and G. J. Brakenhoff, "3d microscopy of transparent objects using third-harmonic generation," *J Microsc*, vol. 191, no. 3, pp. 266–274, 1998.

[65] M. A. Kriech and J. C. Conboy, "Imaging chirality with surface second harmonic generation microscopy," *Journal of the American Chemical Society*, vol. 127, no. 9, pp. 2834–2835, 2005.

[66] J. Butet, P.-F. Brevet, and O. J. F. Martin, "Optical second harmonic generation in plasmonic nanostructures: From fundamental principles to advanced applications," *ACS Nano*, vol. 9, no. 11, pp. 10545–10562, 2015.

[67] J. Sun, X. Wang, S. Chang, M. Zeng, S. Shen, and N. Zhang, "Far-field radiation patterns of second harmonic generation from gold nanoparticles under tightly focused illumination," *Optics Express*, vol. 24, no. 7, pp. 7477–7487, 2016.

[68] E. Slenders, H. Bové, M. Urbain, Y. Mugnier, A. Y. Sonay, P. Pantazis, L. Bonacina, P. Vanden Berghe, M. Vandeven, and M. Ameloot, "Image correlation spectroscopy with second harmonic generating nanoparticles in suspension and in cells," *The Journal of Physical Chemistry Letters*, pp. 6112–6118, 2018.

[69] E. Georgiou, T. Theodossiou, V. Hovhannisyan, K. Politopoulos, G. S. Rapti, and D. Yova, "Second and third optical harmonic generation in type i collagen, by nanosecond laser irradiation, over a broad spectral region," *Optics Communications*, vol. 176, no. 1, pp. 253–260, 2000.

[70] X. Chen, O. Nadiarynkh, S. Plotnikov, and P. J. Campagnola, "Second harmonic generation microscopy for quantitative analysis of collagen fibrillar structure," *Nature protocols*, vol. 7, no. 4, pp. 654–669, 2012.

[71] D. James, A. Jambor, H.-Y. Chang, Z. Alden, K. Tilbury, N. Sandbo, and P. Campagnola, "Probing ecm remodeling in idiopathic pulmonary fibrosis via second harmonic generation microscopy analysis of macro/supramolecular collagen structure," *Journal of Biomedical Optics*, vol. 25, no. 1, p. 014505, 2019.

[72] J. S. Bredfeldt, Y. Liu, C. A. Pehlke, M. W. Conklin, J. M. Szulczewski, D. R. Inman, P. J. Keely, R. D. Nowak, T. R. Mackie, and K. W. Eliceiri, "Computational segmentation of collagen fibers from second-harmonic generation images of breast cancer," *Journal of Biomedical Optics*, vol. 19, no. 1, p. 016007, 2014.

[73] A. Kazarine, K. Kolosova, A. A. Gopal, H. Wang, R. Tahara, A. Rammal, K. Kost, L. Mongeau, N. Y. K. Li-Jessen, and P. W. Wiseman, "Multimodal virtual histology of rabbit vocal folds by nonlinear microscopy and nano computed tomography," *Biomedical Optics Express*, vol. 10, no. 3, pp. 1151–1164, 2019.

[74] S. Hirano, S. Minamiguchi, M. Yamashita, T. Ohno, S.-i. Kanemaru, and M. Kitamura, "Histologic characterization of human scarred vocal folds," *Journal of Voice*, vol. 23, no. 4, pp. 399–407, 2009.

[75] R. M. Williams, W. R. Zipfel, and W. W. Webb, "Interpreting second-harmonic generation images of collagen i fibrils," *Biophysical Journal*, vol. 88, no. 2, pp. 1377–1386, 2005.

[76] A. E. Tuer, S. Krouglov, N. Prent, R. Cisek, D. Sandkuijl, K. Yasufuku, B. C. Wilson, and V. Barzda, "Nonlinear optical properties of type i collagen fibers studied by polarization dependent second harmonic generation microscopy," *The Journal of Physical Chemistry B*, vol. 115, no. 44, pp. 12759–12769, 2011.

[77] D. Débarre, W. Supatto, A.-M. Pena, A. Fabre, T. Tordjmann, L. Combettes, M.-C. Schanne-Klein, and E. Beaurepaire, "Imaging lipid bodies in cells and tissues using third-harmonic generation microscopy," *Nature Methods*, vol. 3, p. 47, 2005.

[78] G. Bautista, S. Pfisterer, M. Huttunen, S. Ranjan, K. Kanerva, E. Ikonen, and M. Kauranen, "Polarized thg microscopy identifies compositionally different lipid droplets in mammalian cells," *Biophysical Journal*, vol. 107, no. 10, pp. 2230–2236, 2014.

[79] M. Zimmerley, P. Mahou, D. Débarre, M.-C. Schanne-Klein, and E. Beaurepaire, "Probing ordered lipid assemblies with polarized third-harmonic-generation microscopy," *Physical Review X*, vol. 3, no. 1, p. 011002, 2013.

[80] G. O. Clay, A. C. Millard, C. B. Schaffer, J. Aus-der Au, P. S. Tsai, J. A. Squier, and D. Kleinfeld, "Spectroscopy of third-harmonic generation: evidence for resonances in model compounds and ligated hemoglobin," *Journal of the Optical Society of America B*, vol. 23, no. 5, pp. 932–950, 2006.

[81] A. Kazarine, F. Baakdah, A. A. Gopal, W. Oyibo, E. Georges, and P. W. Wiseman, "Malaria detection by third-harmonic generation image scanning cytometry," *Anal Chem*, vol. 91, no. 3, pp. 2216–2223, 2019.

[82] J. M. Bélisle, S. Costantino, M. L. Leimanis, M.-J. Bellemare, D. S. Bohle, E. Georges, and P. W. Wiseman, "Sensitive detection of malaria infection by third harmonic generation imaging," *Biophysical journal*, vol. 94, no. 4, pp. L26–L28, 2008.

[83] N. V. Kuzmin, P. Wesseling, P. C. d. W. Hamer, D. P. Noske, G. D. Galgano, H. D. Mansvelder, J. C. Baayen, and M. L. Groot, "Third harmonic generation imaging for fast, label-free pathology of human brain tumors," *Biomedical Optics Express*, vol. 7, no. 5, pp. 1889–1904, 2016.

[84] J.-X. Cheng and X. S. Xie, "Green's function formulation for third-harmonic generation microscopy," *Journal of the Optical Society of America B*, vol. 19, no. 7, pp. 1604–1610, 2002.

[85] C.-A. Couture, S. Bancelin, J. Van der Kolk, K. Popov, M. Rivard, K. Légaré, G. Martel, H. Richard, C. Brown, S. Laverty, L. Ramunno, and F. Légaré, "The impact of collagen fibril polarity on second harmonic generation microscopy," *Biophysical journal*, vol. 109, no. 12, pp. 2501–2510, 2015.

[86] L. Moreaux, O. Sandre, S. Charpak, M. Blanchard-Desce, and J. Mertz, "Coherent scattering in multi-harmonic light microscopy," *Biophysical Journal*, vol. 80, no. 3, pp. 1568–1574, 2001.

[87] S. Psilodimitrakopoulos, S. I. C. O. Santos, I. Amat-Roldan, A. K. N. Thayil, D. Artigas, and P. Loza-Alvarez, "In vivo, pixel-resolution mapping of thick filaments' orientation in nonfibrilar muscle using polarization-sensitive second harmonic generation microscopy," *Journal of Biomedical Optics*, vol. 14, no. 1, p. 014001, 2009.

[88] D. A. Dombeck, K. A. Kasischke, H. D. Vishwasrao, M. Ingelsson, B. T. Hyman, and W. W. Webb, "Uniform polarity microtubule assemblies imaged in native brain tissue by second-harmonic generation microscopy," *Proceedings of the National Academy of Sciences*, vol. 100, no. 12, p. 7081, 2003.

[89] P. C. Stoller, B.-M. Kim, A. M. Rubenchik, K. M. Reiser, and L. B. D. Silva, "Polarization-dependent optical second-harmonic imaging of rat-tail tendon," *Journal of Biomedical Optics*, vol. 7, no. 2, pp. 205–214, 10, 2002.

[90] W. R. Zipfel, R. M. Williams, R. Christie, A. Y. Nikitin, B. T. Hyman, and W. W. Webb, "Live tissue intrinsic emission microscopy using multiphoton-excited native fluorescence and second harmonic generation," *Proceedings of the National Academy of Sciences*, vol. 100, no. 12, p. 7075, 2003.

[91] M. Rehberg, F. Krombach, U. Pohl, and S. Dietzel, "Label-free 3d visualization of cellular and tissue structures in intact muscle with second and third harmonic generation microscopy," *PLoS ONE*, vol. 6, no. 11, p. e28237, 2011.

[92] T.-M. Liu, Y.-W. Lee, C.-F. Chang, S.-C. Yeh, C.-H. Wang, S.-W. Chu, and C.-K. Sun, "Imaging polyhedral inclusion bodies of nuclear polyhedrosis viruses with second harmonic generation microscopy," *Optics Express*, vol. 16, no. 8, pp. 5602–5608, 2008.

[93] A. Kazarine, A. A. Gopal, and P. W. Wiseman, "Nonlinear microscopy of common histological stains reveals third harmonic generation harmonophores," *Analyst*, vol. 144, no. 10, pp. 3239–3249, 2019.

[94] M. J. Farrar, F. W. Wise, J. R. Fetcho, and C. B. Schaffer, "In vivo imaging of myelin in the vertebrate central nervous system using third harmonic generation microscopy," *Biophysical journal*, vol. 100, no. 5, pp. 1362–1371, 2011.

[95] E. Munch, M. E. Launey, D. H. Alsem, E. Saiz, A. P. Tomsia, and R. O. Ritchie, "Tough, bio-inspired hybrid materials," *Science*, vol. 322, no. 5907, pp. 1516–1520, 2008.

[96] U. G. K. Wegst, H. Bai, E. Saiz, A. P. Tomsia, and R. O. Ritchie, "Bioinspired structural materials," *Nature Materials*, vol. 14, no. 1, pp. 23–36, 2015.

[97] K. L. Goh, *20 - Current understanding of interfacial stress transfer mechanisms in connective tissue*, pp. 529–549. Woodhead Publishing, 2020.

[98] J. M. Lucas, E. Vaccaro, and J. H. Waite, "A molecular, morphometric and mechanical comparison of the structural elements of byssus from ¡em¿mytilus edulis¡/em¿ and

¡em¿mytilus galloprovincialis¡/em¿," *Journal of Experimental Biology*, vol. 205, no. 12, pp. 1807–1817, 2002.

[99] F. Rodríguez, L. Morán, G. González, E. Troncoso, and R. N. Zúñiga, "Collagen extraction from mussel byssus: a new marine collagen source with physicochemical properties of industrial interest," *Journal of Food Science and Technology*, vol. 54, no. 5, pp. 1228–1238, 2017.

[100] M. J. Harrington, F. Jehle, and T. Priemel, "Mussel byssus structure-function and fabrication as inspiration for biotechnological production of advanced materials," *Biotechnology Journal*, vol. 13, no. 12, p. 1800133, 2018.

[101] T. Priemel, E. Degtyar, M. N. Dean, and M. J. Harrington, "Rapid self-assembly of complex biomolecular architectures during mussel byssus biofabrication," *Nature Communications*, vol. 8, no. 1, p. 14539, 2017.

[102] X. Qin and J. H. Waite, "Exotic collagen gradients in the byssus of the mussel mytilus edulis," *The Journal of Experimental Biology*, vol. 198, no. 3, p. 633, 1995.

[103] Bell and Gosline, "Mechanical design of mussel byssus: material yield enhances attachment strength," *The Journal of experimental biology*, vol. 199 Pt 4, pp. 1005–17, 1996.

[104] Z. Qin and M. J. Buehler, "Impact tolerance in mussel thread networks by heterogeneous material distribution," *Nature Communications*, vol. 4, 2013.

[105] A. Hagenau, P. Papadopoulos, F. Kremer, and T. Scheibel, "Mussel collagen molecules with silk-like domains as load-bearing elements in distal byssal threads," *Journal of Structural Biology*, vol. 175, no. 3, pp. 339–347, 2011.

[106] A. Trapaidze, M. D'Antuono, P. Fratzl, and M. J. Harrington, "Exploring mussel byssus fabrication with peptide-polymer hybrids: Role of ph and metal coordination

in self-assembly and mechanics of histidine-rich domains," *European Polymer Journal*, vol. 109, pp. 229–236, 2018.

[107] E. Filippidi, T. R. Cristiani, C. D. Eisenbach, J. H. Waite, J. N. Israelachvili, B. K. Ahn, and M. T. Valentine, "Toughening elastomers using mussel-inspired iron-catechol complexes," *Science*, vol. 358, no. 6362, pp. 502–505, 2017.

[108] C. A. Monnier, D. G. DeMartini, and J. H. Waite, "Intertidal exposure favors the soft-studded armor of adaptive mussel coatings," *Nature Communications*, vol. 9, no. 1, p. 3424, 2018.

[109] N. Holten-Andersen, G. E. Fantner, S. Hohlbauch, J. H. Waite, and F. W. Zok, "Protective coatings on extensible biofibres," *Nature Materials*, vol. 6, no. 9, pp. 669–672, 2007.

[110] M. J. Harrington, A. Masic, N. Holten-Andersen, J. H. Waite, and P. Fratzl, "Iron-clad fibers: A metal-based biological strategy for hard flexible coatings," *Science*, vol. 328, no. 5975, p. 216, 2010.

[111] M. Mousa and Y. Dong, *5 - A critical role of interphase properties and features on mechanical properties of poly(vinyl alcohol) (PVA) bionanocomposites: nanoscaled characterisation and modelling*, pp. 115–136. Woodhead Publishing, 2020.

[112] A. P. Kiseleva, P. V. Krivoshapkin, and E. F. Krivoshapkina, "Recent advances in development of functional spider silk-based hybrid materials," *Frontiers in Chemistry*, vol. 8, no. 554, 2020.

[113] S. V. Patwardhan, J. R. H. Manning, and M. Chiacchia, "Bioinspired synthesis as a potential green method for the preparation of nanomaterials: Opportunities and challenges," *Current Opinion in Green and Sustainable Chemistry*, vol. 12, pp. 110–116, 2018.

[114] W. L. Rice, S. Firdous, S. Gupta, M. Hunter, C. W. P. Foo, Y. Wang, H. J. Kim, D. L. Kaplan, and I. Georgakoudi, "Non-invasive characterization of structure and morphology of silk fibroin biomaterials using non-linear microscopy," *Biomaterials*, vol. 29, no. 13, pp. 2015–2024, 2008.

[115] K. Kiraly, M. M. Hyttinen, T. Lapvetelainen, M. Elo, I. Kiviranta, J. Dobai, L. Modis, H. J. Helminen, and J. P. A. Arokoski, "Specimen preparation and quantification of collagen birefringence in unstained sections of articular cartilage using image analysis and polarizing light microscopy," *The Histochemical Journal*, vol. 29, no. 4, pp. 317–327, 1997.

[116] P. Kiviranta, J. Rieppo, R. K. Korhonen, P. Julkunen, J. Töyräs, and J. S. Jurvelin, "Collagen network primarily controls poisson's ratio of bovine articular cartilage in compression," *Journal of Orthopaedic Research*, vol. 24, no. 4, pp. 690–699, 2006.

[117] P. Whittaker, R. A. Kloner, D. R. Boughner, and J. G. Pickering, "Quantitative assessment of myocardial collagen with picrosirius red staining and circularly polarized light," *Basic Res Cardiol*, vol. 89, no. 5, pp. 397–410, 1994.

[118] A. Deniset-Besseau, P. D. S. Peixoto, J. Duboisset, C. Loison, F. Hache, E. Benichou, P. F. Brevet, G. Mosser, and M. C. Schanne-Klein, "Nonlinear optical response of the collagen triple helix and second harmonic microscopy of collagen liquid crystals," in *Proc.SPIE*, vol. 7569, 2010.

[119] C. B. Raub, J. Unruh, V. Suresh, T. Krasieva, T. Lindmo, E. Gratton, B. J. Tromberg, and S. C. George, "Image correlation spectroscopy of multiphoton images correlates with collagen mechanical properties," *Biophysical Journal*, vol. 94, no. 6, pp. 2361–2373, 2008.

[120] S. M. Mir, B. Baggett, and U. Utzinger, "The efficacy of image correlation spectroscopy for characterization of the extracellular matrix," *Biomedical Optics Express*, vol. 3, no. 2, pp. 215–224, 2012.

[121] A. Mašić, M. Harrington, J. H. Waite, and P. Fratzl, "In-situ raman spectroscopic imaging of a mussel coating and adhesive," *AIP Conference Proceedings*, vol. 1267, no. 1, pp. 358–359, 2010.

[122] E. Valois, C. Hoffman, D. G. Demartini, and J. H. Waite, "The thiol-rich interlayer in the shell/core architecture of mussel byssal threads," *Langmuir*, vol. 35, no. 48, pp. 15985–15991, 2019.

[123] C. W. Mount and M. Monje, "Wrapped to adapt: Experience-dependent myelination," *Neuron*, vol. 95, no. 4, pp. 743–756, 2017.

[124] B. I. Roots, *The Evolution of Myelinating Cells*, pp. 223–248. Totowa, NJ: Humana Press, 1995.

[125] R. S. Smith, H. Chan, and C. J. Schaap, "Intermittent myelination of small-diameter sciatic axons in xenopus laevis," *Journal of Neurocytology*, vol. 14, no. 2, pp. 269–278, 1985.

[126] I. L. Arancibia-Cárcamo, M. C. Ford, L. Cossell, K. Ishida, K. Tohyama, and D. Attwell, "Node of ranvier length as a potential regulator of myelinated axon conduction speed," *eLife*, vol. 6, p. e23329, 2017.

[127] A. Alizadeh, S. M. Dyck, and S. Karimi-Abdolrezaee, "Myelin damage and repair in pathologic cns: challenges and prospects," *Frontiers in Molecular Neuroscience*, vol. 8, no. 35, 2015.

[128] E. Barbarese, C. Barry, C. H. Chou, D. J. Goldstein, G. A. Nakos, R. Hyde-DeRuyscher, K. Scheld, and J. H. Carson, "Expression and localization of myelin basic protein in oligodendrocytes and transfected fibroblasts," *J Neurochem*, vol. 51, no. 6, pp. 1737–45, 1988.

[129] F. K. Sanders and A. C. Hardy, "The thickness of the myelin sheaths of normal and regenerating peripheral nerve fibres," *Proceedings of the Royal Society of London. Series B - Biological Sciences*, vol. 135, no. 880, pp. 323–357, 1948.

[130] Z. Chorghay, R. T. Káradóttir, and E. S. Ruthazer, "White matter plasticity keeps the brain in tune: Axons conduct while glia wrap," *Frontiers in Cellular Neuroscience*, vol. 12, no. 428, 2018.

[131] E. M. Gibson, D. Purger, C. W. Mount, A. K. Goldstein, G. L. Lin, L. S. Wood, I. Inema, S. E. Miller, G. Bieri, J. B. Zuchero, B. A. Barres, P. J. Woo, H. Vogel, and M. Monje, "Neuronal activity promotes oligodendrogenesis and adaptive myelination in the mammalian brain," *Science*, vol. 344, no. 6183, p. 1252304, 2014.

[132] J. Liu, K. Dietz, J. M. DeLoyht, X. Pedre, D. Kelkar, J. Kaur, V. Vialou, M. K. Lobo, D. M. Dietz, E. J. Nestler, J. Dupree, and P. Casaccia, "Impaired adult myelination in the prefrontal cortex of socially isolated mice," *Nature Neuroscience*, vol. 15, no. 12, pp. 1621–1623, 2012.

[133] P. C. Christensen, C. Brideau, K. W. C. Poon, A. Döring, V. W. Yong, and P. K. Stys, "High-resolution fluorescence microscopy of myelin without exogenous probes," *NeuroImage*, vol. 87, pp. 42–54, 2014.

[134] Y. Fu, H. Wang, T. B. Huff, R. Shi, and J.-X. Cheng, "Coherent anti-stokes raman scattering imaging of myelin degradation reveals a calcium-dependent pathway in lyso-ptdcho-induced demyelination," *Journal of neuroscience research*, vol. 85, no. 13, pp. 2870–2881, 2007.

[135] C.-R. Hu, D. Zhang, M. Slipchenko, J.-X. Cheng, and B. Hu, "Label-free real-time imaging of myelination in the xenopus laevis tadpole by in vivo stimulated raman scattering microscopy," *Journal of Biomedical Optics*, vol. 19, no. 8, p. 086005, 2014.

[136] D. G. Gonsalvez, S. Yoo, J. L. Fletcher, R. J. Wood, G. A. Craig, S. S. Murray, and J. Xiao, "Imaging and quantification of myelin integrity after injury with spectral confocal reflectance microscopy," *Frontiers in molecular neuroscience*, vol. 12, pp. 275–275, 2019.

[137] H. Lim, D. Sharoukhov, I. Kassim, Y. Zhang, J. L. Salzer, and C. V. Melendez-Vasquez, "Label-free imaging of schwann cell myelination by third harmonic generation microscopy," *Proceedings of the National Academy of Sciences*, vol. 111, no. 50, p. 18025, 2014.

[138] X.-R. Huang and R. W. Knighton, "Microtubules contribute to the birefringence of the retinal nerve fiber layer," *Investigative Ophthalmology & Visual Science*, vol. 46, no. 12, pp. 4588–4593, 2005.

[139] J. Lin, W. Zheng, Z. Wang, and Z. Huang, "Label-free three-dimensional imaging of cell nucleus using third-harmonic generation microscopy," *Applied Physics Letters*, vol. 105, no. 10, p. 103705, 2014.

[140] B. Maity and S. Maiti, "Label-free imaging of neurotransmitters in live brain tissue by multi-photon ultraviolet microscopy," *Neuronal Signaling*, vol. 2, no. 4, 2018.

[141] C. Hildebrand and R. Hahn, "Relation between myelin sheath thickness and axon size in spinal cord white matter of some vertebrate species," *Journal of the Neurological Sciences*, vol. 38, no. 3, pp. 421–434, 1978.

[142] R. M. Grainger, "Xenopus tropicalis as a model organism for genetics and genomics: past, present, and future," *Methods in molecular biology (Clifton, N.J.)*, vol. 917, pp. 3–15, 2012.

[143] W. Xin and J. R. Chan, "Myelin plasticity: sculpting circuits in learning and memory," *Nature Reviews Neuroscience*, vol. 21, no. 12, pp. 682–694, 2020.

[144] M. J. Sanderson, I. Smith, I. Parker, and M. D. Bootman, "Fluorescence microscopy," *Cold Spring Harbor protocols*, vol. 2014, no. 10, pp. pdb.top071795–pdb.top071795, 2014.

[145] M. W. Wessendorf and T. C. Brelje, "Multicolor fluorescence microscopy using the laser-scanning confocal microscope," *Neuroprotocols*, vol. 2, no. 2, pp. 121–140, 1993.

[146] M. Lukumbuzya, M. Schmid, P. Pjevac, and H. Daims, "A multicolor fluorescence in situ hybridization approach using an extended set of fluorophores to visualize microorganisms," *Frontiers in Microbiology*, vol. 10, no. 1383, 2019.

[147] F. Poulon, M. Zanello, A. Ibrahim, A. J. Zaylaa, P. Varlet, B. Devaux, and D. A. Haidar, "Comparison between fresh and fixed human biopsies using spectral and lifetime measurements: Fluorescence analysis using one and two photon excitations," in *2015 International Conference on Advances in Biomedical Engineering (ICABME)*, pp. 25–28, 2015.

[148] A. Zoumi, A. Yeh, and B. J. Tromberg, "Imaging cells and extracellular matrix in vivo by using second-harmonic generation and two-photon excited fluorescence," *Proceedings of the National Academy of Sciences*, vol. 99, no. 17, pp. 11014–11019, 2002.

[149] C. Stock, K. Zlatanov, and T. Halfmann, "Dispersion-enhanced third-harmonic microscopy," *Optics Communications*, vol. 393, pp. 289–293, 2017.

[150] A. Hayat, A. Nevet, P. Ginzburg, and M. Orenstein, "Applications of two-photon processes in semiconductor photonic devices: invited review," *Semiconductor Science and Technology*, vol. 26, no. 8, p. 083001, 2011.

[151] T. Latychevskaia, "Lateral and axial resolution criteria in incoherent and coherent optics and holography, near- and far-field regimes," *Applied Optics*, vol. 58, no. 13, pp. 3597–3603, 2019.

[152] G. Cox and C. J. Sheppard, "Practical limits of resolution in confocal and non-linear microscopy," *Microscopy Research and Technique*, vol. 63, no. 1, pp. 18–22, 2004.

[153] M. Gu, "Resolution in three-photon fluorescence scanning microscopy," *Optics Letters*, vol. 21, no. 13, pp. 988–990, 1996.

[154] Z. Tang, D. Xing, and S. Liu, "The nonlinear imaging theory of second harmonic and third harmonic generations in confocal microscopy," *Science in China Series G Physics Mechanics and Astronomy*, vol. 47, pp. 8–16, 2004.

[155] U. Petzold, A. Büchel, and T. Halfmann, "Effects of laser polarization and interface orientation in harmonic generation microscopy," *Optics Express*, vol. 20, no. 4, pp. 3654–3662, 2012.

[156] H. Fröhlich, "Long-range coherence and energy storage in biological systems," *International Journal of Quantum Chemistry*, vol. 2, no. 5, pp. 641–649, 1968.

[157] Y. Barad, H. Eisenberg, M. Horowitz, and Y. Silberberg, "Nonlinear scanning laser microscopy by third harmonic generation," *Applied Physics Letters*, vol. 70, no. 8, pp. 922–924, 1997.

[158] Y. R. Shen, "Optical second harmonic generation at interfaces," *Annual Review of Physical Chemistry*, vol. 40, no. 1, pp. 327–350, 1989.

[159] K. D. Bonin and T. J. McIlrath, "Two-photon electric-dipole selection rules," *Journal of the Optical Society of America B*, vol. 1, no. 1, pp. 52–55, 1984.

[160] A. Nag and D. Goswami, "Polarization induced control of single and two-photon fluorescence," *The Journal of Chemical Physics*, vol. 132, no. 15, p. 154508, 2010.

[161] I. Micu, C. Brideau, L. Lu, and P. Stys, "Effects of laser polarization on responses of the fluorescent ca¡sup¿2+¡/sup¿ indicator x-rhod-1 in neurons and myelin," *Neurophotonics*, vol. 4, no. 2, p. 025002, 2017.

[162] S. Brasselet, "Polarization-resolved nonlinear microscopy: application to structural molecular and biological imaging," *Advances in Optics and Photonics*, vol. 3, no. 3, p. 205, 2011.

[163] I. Gusachenko, G. Latour, and M.-C. Schanne-Klein, "Polarization-resolved second harmonic microscopy in anisotropic thick tissues," *Optics Express*, vol. 18, no. 18, pp. 19339–19352, 2010.

[164] N. Olivier, F. Aptel, K. Plamann, M.-C. Schanne-Klein, and E. Beaurepaire, "Harmonic microscopy of isotropic and anisotropic microstructure of the human cornea," *Optics Express*, vol. 18, no. 5, pp. 5028–5040, 2010.

[165] U. Petzold, C. Wenski, A. Romanenko, and T. Halfmann, "Spatial emission profiles at different interface orientations in third harmonic generation microscopy," *Journal of the Optical Society of America B*, vol. 30, no. 6, pp. 1725–1731, 2013.

[166] V. V. Yakovlev and S. V. Govorkov, "Diagnostics of surface layer disordering using optical third harmonic generation of a circular polarized light," *Applied Physics Letters*, vol. 79, no. 25, pp. 4136–4138, 2001.

[167] D. Oron, E. Tal, and Y. Silberberg, "Depth-resolved multiphoton polarization microscopy by third-harmonic generation," *Optics Letters*, vol. 28, no. 23, pp. 2315–2317, 2003.

[168] D. Oron, D. Yelin, E. Tal, S. Raz, R. Fachima, and Y. Silberberg, "Depth-resolved structural imaging by third-harmonic generation microscopy," *Journal of Structural Biology*, vol. 147, no. 1, pp. 3–11, 2004.

[169] C. Vonesch, F. Aguet, J. Vonesch, and M. Unser, "The colored revolution of bioimaging," *IEEE Signal Processing Magazine*, vol. 23, no. 3, pp. 20–31, 2006.

[170] X. Han and E. Brown, "Measurement of the ratio of forward-propagating to back-propagating second harmonic signal using a single objective," *Optics Express*, vol. 18, no. 10, pp. 10538–10550, 2010.

[171] M. Piovoso and P. A. Laplante, "Kalman filter recipes for real-time image processing," *Real-Time Imaging*, vol. 9, no. 6, pp. 433–439, 2003.

[172] U. Bal, "Dual tree complex wavelet transform based denoising of optical microscopy images," *Biomedical Optics Express*, vol. 3, no. 12, pp. 3231–3239, 2012.

[173] S. Jean-Luc, E. J. Candes, and D. L. Donoho, "The curvelet transform for image denoising," *IEEE Transactions on Image Processing*, vol. 11, no. 6, pp. 670–684, 2002.

[174] P. S. Addison, *The illustrated wavelet transform handbook : introductory theory and applications in science, engineering, medicine, and finance*. Bristol, UK ;: Institute of Physics Pub., 2002.

[175] J. Boulanger, C. Kervrann, P. Bouthemy, P. Elbau, J. Sibarita, and J. Salamero, "Patch-based nonlocal functional for denoising fluorescence microscopy image sequences," *IEEE Transactions on Medical Imaging*, vol. 29, no. 2, pp. 442–454, 2010.

[176] D. Magde, E. Elson, and W. W. Webb, "Thermodynamic fluctuations in a reacting system—measurement by fluorescence correlation spectroscopy," *Physical Review Letters*, vol. 29, no. 11, pp. 705–708, 1972.

[177] N. O. Petersen, *FCS and Spatial Correlations on Biological Surfaces*, book section 8, pp. 162–184. Springer Series in Chemical Physics, Berlin: Springer, 2001.

[178] C. Baugh, *Correlation function and power spectra in cosmology*. Bristol and Philadelphia: Institute of Physics Publishing, 2006.

[179] J. W. D. Comeau, D. L. Kolin, and P. W. Wiseman, "Accurate measurements of protein interactions in cells via improved spatial image cross-correlation spectroscopy," *Molecular BioSystems*, vol. 4, no. 6, pp. 672–685, 2008.

[180] J. Hwang, L. A. Gheber, L. Margolis, and M. Edidin, "Domains in cell plasma membranes investigated by near-field scanning optical microscopy," *Biophysical Journal*, vol. 74, no. 5, pp. 2184–2190, 1998.

[181] D. L. Kolin and P. W. Wiseman, "Advances in image correlation spectroscopy: Measuring number densities, aggregation states, and dynamics of fluorescently labeled macromolecules in cells," *Cell Biochemistry and Biophysics*, vol. 49, no. 3, pp. 141–164, 2007.

[182] N. O. Petersen, P. L. Höddelius, P. W. Wiseman, O. Seger, and K. E. Magnusson, "Quantitation of membrane receptor distributions by image correlation spectroscopy: concept and application," *Biophysical Journal*, vol. 65, no. 3, pp. 1135–1146, 1993.

[183] S. Costantino, J. W. D. Comeau, D. L. Kolin, and P. W. Wiseman, "Accuracy and dynamic range of spatial image correlation and cross-correlation spectroscopy," *Biophysical Journal*, vol. 89, no. 2, pp. 1251–1260, 2005.

[184] Y. Li, F. Xu, F. Zhang, P. Xu, M. Zhang, M. Fan, L. Li, X. Gao, and R. Han, "Dlbi: deep learning guided bayesian inference for structure reconstruction of super-resolution fluorescence microscopy," *Bioinformatics*, vol. 34, no. 13, pp. i284–i294, 2018.

[185] P. A. Yushkevich, J. Piven, H. C. Hazlett, R. G. Smith, S. Ho, J. C. Gee, and G. Gerig, "User-guided 3d active contour segmentation of anatomical structures: Significantly improved efficiency and reliability," *NeuroImage*, vol. 31, no. 3, pp. 1116–1128, 2006.

[186] Z. Burdikova, Z. Svindrych, C. Hickey, M. G. Wilkinson, M. A. E. Auty, O. Samek, S. Bernatova, V. Krzyzanek, A. Periasamy, and J. J. Sheehan, "Application of advanced light microscopic techniques to gain deeper insights into cheese matrix physico-chemistry," *Dairy Science & Technology*, vol. 95, no. 5, pp. 687–700, 2015.

[187] Y. Liu, A. Keikhosravi, C. A. Pehlke, J. S. Bredfeldt, M. Dutson, H. Liu, G. S. Mehta, R. Claus, A. J. Patel, M. W. Conklin, D. R. Inman, P. P. Provenzano, E. Sifakis, J. M.

Patel, and K. W. Eliceiri, "Fibrillar collagen quantification with curvelet transform based computational methods," *Frontiers in bioengineering and biotechnology*, vol. 8, pp. 198–198, 2020.

[188] I. T. Jolliffe and J. Cadima, "Principal component analysis: a review and recent developments," *Philosophical Transactions of the Royal Society A: Mathematical, Physical and Engineering Sciences*, vol. 374, no. 2065, p. 20150202, 2016.

[189] S. Vajda, P. Valko, and T. Turányi, "Principal component analysis of kinetic models," *International Journal of Chemical Kinetics*, vol. 17, no. 1, pp. 55–81, 1985.

[190] Y.-L. Hsu, P.-Y. Huang, and D.-T. Chen, "Sparse principal component analysis in cancer research," *Translational Cancer Research*, vol. 3, no. 3, pp. 182–190, 2014.

[191] A. Ertürk, K. Becker, N. Jährling, C. P. Mauch, C. D. Hojer, J. G. Egen, F. Hellal, F. Bradke, M. Sheng, and H.-U. Dodt, "Three-dimensional imaging of solvent-cleared organs using 3disco," *Nature Protocols*, vol. 7, no. 11, pp. 1983–1995, 2012.

[192] Z. Chorghay, D. MacFarquhar, V. J. Li, S. Aufmkolk, A. Schohl, P. W. Wiseman, R. T. Káradóttir, and E. S. Ruthazer, "Activity-dependent alteration of early myelin ensheathment in a developing sensory circuit," *bioRxiv*, p. 2021.04.18.440312, 2021.

[193] M. Linkert, C. T. Rueden, C. Allan, J.-M. Burel, W. Moore, A. Patterson, B. Loranger, J. Moore, C. Neves, D. MacDonald, A. Tarkowska, C. Sticco, E. Hill, M. Rossner, K. W. Eliceiri, and J. R. Swedlow, "Metadata matters: access to image data in the real world," *Journal of Cell Biology*, vol. 189, no. 5, pp. 777–782, 2010.

[194] J. S. Aaron, A. B. Taylor, and T.-L. Chew, "Image co-localization – co-occurrence versus correlation," *Journal of Cell Science*, vol. 131, no. 3, 2018.

[195] J. A. Jiménez-Torres, M. Virumbrales-Muñoz, K. E. Sung, M. H. Lee, E. J. Abel, and D. J. Beebe, "Patient-specific organotypic blood vessels as an in vitro model for

anti-angiogenic drug response testing in renal cell carcinoma," *EBioMedicine*, vol. 42, pp. 408–419, 2019.

[196] A. H. Lee, D. Ghosh, N. Quach, D. Schroeder, and M. R. Dawson, "Ovarian cancer exosomes trigger differential biophysical response in tumor-derived fibroblasts," *Scientific Reports*, vol. 10, no. 1, p. 8686, 2020.

[197] M. A. Diaz, *Fit 1D and 2D gaussian to noisy data*. MathWorks, MATLAB Central File Exchange, 2016.

[198] P. Coupé, M. Munz, J. V. Manjón, E. S. Ruthazer, and D. Louis Collins, "A candle for a deeper in vivo insight," *Medical Image Analysis*, vol. 16, no. 4, pp. 849–864, 2012.

[199] D. J. Jamieson, "Oxidative stress responses of the yeast saccharomyces cerevisiae," *Yeast*, vol. 14, no. 16, pp. 1511–1527, 1998.

[200] O. Sadakane, Y. Masamizu, A. Watakabe, S.-I. Terada, M. Ohtsuka, M. Takaji, H. Mizukami, K. Ozawa, H. Kawasaki, M. Matsuzaki, and T. Yamamori, "Long-term two-photon calcium imaging of neuronal populations with subcellular resolution in adult non-human primates," *Cell Reports*, vol. 13, no. 9, pp. 1989–1999, 2015.

[201] M. Sivaguru, M. M. Kabir, M. R. Gartia, D. S. Biggs, B. S. Sivaguru, V. A. Sivaguru, G. A. Friend, G. L. LIU, S. Sadayappan, and K. C. TOUSSAINT Jr., "Application of an advanced maximum likelihood estimation restoration method for enhanced-resolution and contrast in second-harmonic generation microscopy," *Journal of Microscopy*, vol. 267, no. 3, pp. 397–408, 2017.

[202] C.-H. Yeh, C.-Z. Tan, C.-H. A. Cheng, J.-T. Hung, and S.-Y. Chen, "Improving resolution of second harmonic generation microscopy via scanning structured illumination," *Biomedical optics express*, vol. 9, no. 12, pp. 6081–6090, 2018.

[203] S. Preibisch, S. Saalfeld, and P. Tomancak, "Globally optimal stitching of tiled 3d microscopic image acquisitions," *Bioinformatics*, vol. 25, no. 11, pp. 1463–1465, 2009.

[204] J. Hao, W. Yao, W. B. R. Harris, J. Y. Vink, K. M. Myers, and E. Donnelly, "Characterization of the collagen microstructural organization of human cervical tissue," *Reproduction*, vol. 156, no. 1, pp. 71–79, 2018.

[205] J. Y. Ye, M. N'Gom, Y.-C. Chang, A. Agarwal, N. Kotov, J. R. Baker, and T. B. Norris, "Correlation spectroscopy of third-harmonic generation by single nanorods," in *Conference on Lasers and Electro-Optics/International Quantum Electronics Conference*, OSA Technical Digest (CD), p. CThK3, Optical Society of America, 2009.

[206] S.-W. Chu, S.-P. Tai, M.-C. Chan, C.-K. Sun, I. C. Hsiao, C.-H. Lin, Y.-C. Chen, and B.-L. Lin, "Thickness dependence of optical second harmonic generation in collagen fibrils," *Optics Express*, vol. 15, no. 19, pp. 12005–12010, 2007.

[207] D. F. Holmes, Y. Lu, T. Starborg, and K. E. Kadler, *Collagen Fibril Assembly and Function*, vol. 130, book section 3, pp. 107–142. Academic Press, 2018.

[208] F. Légaré, C. Pfeffer, and B. R. Olsen, "The role of backscattering in shg tissue imaging," *Biophysical Journal*, vol. 93, no. 4, pp. 1312–1320, 2007.

[209] H. L. Michael J. Redlich, "A method to measure myeloarchitecture of the murine cerebral cortex in vivo and ex vivo by intrinsic third-harmonic generation," *Frontiers in Neuroanatomy*, vol. 13, p. 65, 2019.